Ionic liquid/surfactant mixtures as multi-functional electrolytes for graphene-based supercapacitors

by
Sima Lashkari

A thesis

presented to the University of Waterloo

in fulfillment of the

thesis requirement for the degree of

Doctor of Philosophy

in

Chemical Engineering

Waterloo, Ontario, Canada, 2022

Examining Committee Membership

The following serve on the Examining Committee for this thesis. The decision of the Examining Committee is by majority vote.

External Examiner

Igor Zhitomirsky

Professor | Material Science and Engineering | McMaster University

Supervisors

Rajinder Pal

Professor | Chemical Engineering | University of Waterloo

Michael Pope

Associate Professor | Chemical Engineering | University of Waterloo

Internal Examiner

Boxin Zhao

Professor | Chemical Engineering | University of Waterloo

Internal Examiner

Hamed Shahsavan

Assistant Professor | Chemical Engineering | University of Waterloo

Internal/External Examiner

Kevin Musselman

Associate Professor | Mechanical and Mechatronic Engineering | University of Waterloo

Author's Declaration

I hereby declare that I am the sole author of this thesis. This is a true copy of the thesis, including any required final revisions, as accepted by my examiners.

I understand that my thesis may be made electronically available to the public.

Abstract

Supercapacitors store energy by the restructuring of ions at the electrode/electrolyte interface under an applied potential. Supercapacitors bridge the gap between batteries, which are high energy density devices, and electrolytic capacitors, which are high power devices. This makes them suitable for applications that require frequent, short bursts of energy. To increase their utility in commercial applications, supercapacitors with higher energy densities are desired. Therefore, considerable research efforts have focused on developing new materials systems that exhibit higher capacitance when formulated as an electrode and electrode/electrolyte combinations which enable stable, high voltage operation. To this end, the combination of graphene-based materials such as reduced graphene oxide (rGO) as an electrode material and ionic liquid electrolytes have shown significant promise. Graphene has one of the highest theoretical surface areas for double-layer charging, can pack into dense lamellar structures and can exhibit a high electrical conductivity while ionic liquids (ILs) exhibit the highest electrochemical stability window of all electrolytes.

The main challenge with graphene-based electrodes is that the individual, atomically thin sheets tend to restack into low surface area, graphite-like aggregates. This lowers the ion-accessible surface area and thus capacitance of graphene-based supercapacitors. Thus, the main objective of this thesis, is to overcome the restacking problem by using ILs as both an electrolyte and physical spacer which defines the electrolyte-filled pore space between the restacked sheets to maximize the ion-accessible surface area. To do this, we investigate and build upon a newly discovered approach which utilizes non-ionic surfactants to deliver non-surface active, hydrophobic ILs to the surface of dispersed graphene oxide (GO) and rGO. When these IL decorated sheets are cast as electrodes, the adsorbed layer is expected to define the electrolyte-filled pore space, potentially maximizing the electrode capacitance.

In the first study, we aimed to understand the nature of the dispersed and adsorbed phases and the important factors which impact the adsorbed layer structure for several combinations of IL and common non-ionic surfactants (Tween 20 and Triton X-100). The self-assembled structures for both surfactants, in combination with IL, appeared to be mixed micelles that spontaneously adsorb onto GO, forming a compact film. Using fluorescence labeling of the IL and surfactant phases, the adsorption behavior of these surfactant/IL micelle were quantified and compared at different adsorbent concentration. The adsorption quantity was found to be Langmuirian at lower concentrations of IL and sensitive to the adsorbent concentration, with lower adsorbent concentration leading to higher adsorbed amount. Atomic force microscopy is used to analyze the adsorbed layer thickness. The first plateau of the Langmuirian curve marks monolayer arrangement with ~ 1 nm thickness. Adsorption beyond this plateau leads to thicker (> 30 nm), inhomogeneous adsorbed layers. TX-100 behaves similarly to Tween 20, while it requires a lower ratio of TX-100/IL (i.e., 3 vs. 4 for Tween 20) to solubilize the IL, suggesting that it is a more efficient self-assembly vehicle for EMImTFSI.

In the second project, we wanted to investigate the potentials impacts of leaving the non-ionic surfactant mixed with the IL on double-layer formation and ionic conductivity. Thus, we studied the double layer formed at the interface of IL/TX-100 mixtures with glassy carbon electrodes. In preliminary studies, we found that P123 can surpass the ability of TX-100 to self-assemble with IL. Using this surfactant, a stable dispersion of IL in water could be achieved at a P123/IL ratio of 1. Therefore we compared IL/P123 double layer performance with that of TX-100. A significant increase in the minimum capacitance is observed at 40 wt.% surfactant by up to 88% and 102% for P123 and TX-100, respectively. On the other hand, the higher viscosity of the mixtures, lowers the ionic conductivity from 8.5 mS cm^{-1} (neat IL) to 1 mS cm^{-1} (40 wt.% surfactant). Despite the significantly higher viscosity of P123/IL mixtures compared to TX-100/IL, both electrolyte series show the same

reduction in ionic conductivity with respect to concentration. Pulse field gradient nuclear magnetic resonance was also used to show that for both electrolyte series, the diffusion coefficients follow a similar trend.

In the final project, we used our fundamental understanding of the self-assembly process and the double layer performance of the mixed surfactant/IL systems to fabricate high density electrodes with improved performance. Using P123, as the surfactant with proven ability to lower the ionic correlation and solubilize IL at a lower P123/IL ratio, we formulated electrodes at different concentration of P123 using a low concentration of chemically reduced graphene oxide (i.e., 0.2 mg/ml) as an adsorbent for self-assembly and electrode active material. At each surfactant concentration, the IL/P123 ratio was varied to see the full spectrum of capacitance change with respect to self-assembly. The final dispersions were sprayed into liquid nitrogen and freeze dried (i.e., flash freeze dried) to lock in the adsorbed layer on rGO. This is because we found that these self-assembled structures are very dynamic and sensitive to concentration change which gradually increases during air drying. For 20 wt.% P123 at IL/P123=2 the gravimetric capacitance of 148 F/g and bulk density of 0.54 g/cm3, were obtained giving rise to maximum volumetric capacitance of 75 F/cm^3. In contrast, for the 60 wt.% P123 (IL/P123=3) with highest gravimetric capacitance of 247 F/g, the volumetric capacitance of 45 F/cm^3 was obtained due to lowered bulk density of 0.18 g/cm^3. Overall, the gravimetric capacitance increased with increasing the total spacer mass, while the bulk densities of the electrodes continuously decreased. Nevertheless, comparing the theoretical bulk densities of our electrodes with the measured bulk densities uncover the presence of ~ 66 % porosity in our electrodes which can significantly boost the volumetric capacitance and overall performance of the device.

Acknowledgements

I would like thank both my supervisors Dr. Pal and Dr. Pope for supporting me to pursue this PhD. I am grateful to Dr. Pope for patiently helping me grow as a researcher with his guidance and directions which helped me find my way through many uncertainties and difficult times during these 4 years, and to Dr. Pal for his advices and his patience with me to finally get to where I am.

I would also like to thanks all my committee members, Dr. Boxin Zhao, Hamed Shahsavan, Kevin Musselman from University of Waterloo, and my external committee member Dr. Igor Zhitomirsky, from McMaster University for the time they took and their valuable feedback and suggestions.

In addition, special thanks to Chemical Engineering management team, for the great work and care they provided which helped me move forwards knowing I can always get the support and information I needed.

I want to also send my words of appreciation to my friends here, who helped me find joy, togetherness, love and support during these years. Life without those moments would have been gloomy and colorless, and my team members who supported me and helped me with their feedback and guidance to move forward with more ease.

And last but not least, I want to send my greatest appreciations and love to my parents for patiently supporting me and helping me steer my way through life and follow my callings.

Table of Contents

List of Figures

List of Tables

Chapter 1
Introduction

Today's world is faced with global warming as a result of an increased emissions of greenhouse gases (GHG) due to the excessive use of fossil fuels. Consequently, the urgency for development of more renewable energy resources such as solar and wind has risen. Nevertheless, wind and solar are intermittent sources of energy and require a reliable energy storage system such as a supercapacitor and battery for their practical application. In addition, transportation, which is predominantly overtaken by fossil fuels is currently contributing to around 30 to 40% of the GHG emissions. This has led to the more recent commercialization of electric cars as a more environmentally friendly option. Although batteries of mainly the lithium-ion (Li-ion) technology, are currently at the forefront of research for use in electric vehicle, supercapacitor have recently been given equal attention[1] due to their superior power performance and cycle life, originating from their purely physical energy storage mechanism.[2] This can place them together with Li-ion batteries in hybrid electric vehicles to increase efficiency by capturing energy from breaking (i.e., regenerative breaking) and providing rapid bursts of current for engine starters. In addition, as a power device, supercapacitors are being increasingly used in applications where a sudden burst of energy is required in a short period of time (usually few seconds), for instances in seaport cranes, emergency doors on the Airbus A380, heavy hybrid vehicles, portable electronics and finally to store off-peak electricity from the grid during off-peak times. [3,4]

Supercapacitors can store energy using two different mechanisms: As electric double layer capacitance, or double-layer capacitance supplemented by the so-called pseudocapacitance originating from electrochemical reactions. To induce pseudocapacitance, usually conductive polymers such as polyaniline or metal oxides such as RuO_2 are being used. Although, pseudocapacitance increases the overall capacitance of the device, in some cases it compromises the cycle life performance. Electric double layer capacitors

(EDLCs), on the other hand, use a purely physical mechanism where electrostatic energy is stored in the electrode/electrolyte interfaces. Due to the purely physical nature of charging, EDLCs typically sustain very rapid charge/discharge processes, long cycle life and high-power density which make them superior compared to most Li-ion batteries for applications where power, device longevity, reliability, and safety are of primary concern. However, EDLCs suffer from low energy density which restricts their commercial applications. Figure 1-1 is the Ragone plot [5] which compares batteries, capacitors, and supercapacitors in terms of energy density and power density. It can be seen that supercapacitors bridge the gap between batteries and electrolytic capacitors. Therefore, the main challenge for supercapacitor is to increase their energy density.

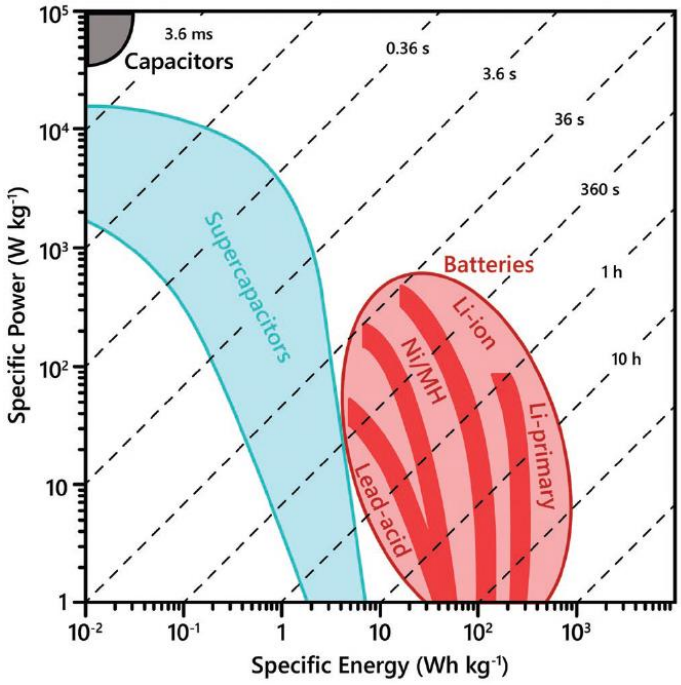

Figure 1-1:Ragone plot, the relationship between power density and energy density[6]

The volumetric energy density (E_V) is the main performance metric for supercapacitors and is proportional to C_V, which is the volumetric capacitance and U^2, which is the cell operating voltage. C_V is a product of bulk density of electrode (ρ_B) and its gravimetric capacitance (C_G). The gravimetric capacitance of an electrode is its areal double layer capacitance (C_{DL}), times the specific surface area (SSA) of the active material. Therefore, to improve E_V of a supercapacitor, we need high ρ_B with large SSA and an electrolyte with high electrochemical voltage window in combination with the electrode used.

Commercial supercapacitors are usually made of activated carbon (AC), mainly due to its high SSA and chemical inertness. However, as will be discussed in more details in the upcoming sections, these materials impose several limitations to the performance of a supercapacitor as their pore structure is such that not the entire specific surface area is accessible to the electrolyte. Therefore, research in this field is focused on mainly engineering the pore structure in a way that it is accessible to certain electrolyte and ionic sizes. [7] This often requires having a blend of both micropores (i.e., < 2 nm) and mesopores (i.e., 5-50 nm) which involves rather intricate treatments. Another avenue in addressing this issue is to use 2D materials such as graphene, MXenes, transition metal dichalcogenide, etc., with intrinsically high surface area due to their nanoscale 2D structures, and use them as a building blocks for electrode fabrication in a so-called bottom-up approach. Single layer graphene is a 2D, one atom thick material which has recently been explored for energy storage applications due to myriads of favorable properties including theoretically large specific surface area (2630 m^2/g) and high electronic conductivity. However, graphene is plagued with low C_{DL} due to its low electronic density of states (DOSs,to be explained in more details later), resulting in low energy density. [8,9] In addition, graphene is not a naturally occurring material. It is often produced by reduction of chemically oxidized graphite in a chemical or thermal reduction methods at high temperature (~1000 °C) which creates reduced graphene oxide (rGO). rGO, with high density of defects and disorder, can offer an increased DOSs and, therefore, larger $C_{DL,}$ leading to gravimetric capacitance of around 400- 500 F/g (when using high surface area materials). [8] Note that this value depends also on the

electrolyte being used. However, due to the strong sheet-sheet van der Waals interactions, rGO quickly restacks upon reduction and, thus, in practice, this high SSA cannot be completely utilized. The first rGO-based supercapacitor introduced by Stroller et al.[10] has only shown capacitance of 135 and 99 F/g in aqueous and organic electrolyte, respectively. This huge loss of capacitance is indicative of agglomeration and restacking of the chemically reduced graphene oxide upon drying. To remedy this problem, a physical spacer has been repeatedly utilized in the literature. [11–14] Although, using these spacers improves the rate performance and capacitance, due to the added weight from the spacer, they impose a constraint on the maximum achievable energy density. In addition, this still requires electrolyte imbibition steps to infuse the electrode pores with electrolyte. Using an electrolyte as spacer can circumvent this issue, while reducing the mass of inactive materials and increasing the electrode's ρ_B. Therefore, the main objectives of this thesis will be around exploring this option for rGO in combination with an electrolyte with high electrochemical potential windows such as ionic liquid (i.e., room temperature molten salts). These electrolytes are of higher electrochemical stability and, as will be discussed in more details in the upcoming section, can improve the energy density. Before laying out the specifics of my thesis objectives, a brief background on main classifications of supercapacitors, their performances metrics and material of constructions such as electrodes and electrolytes will be provided in the following chapter.

Chapter 2
Background

2.1 Principles of supercapacitors

Depending on the mechanism of energy storage, supercapacitors can be classified into two main categories, EDLC or pseudocapacitors. While EDLCs are purely physical and store electric charge within the double layer formed between electrolyte and electrode, pseudocapacitors have an extra mechanism for charge storage, which occurs based on fast and reversible redox reaction between electroactive groups in electrolyte and functional groups on the surface of electrode. Due to this added charge storage mechanism, pseudocapacitors possess high capacitance compared to EDLCs. In some instances, this added pseudocapacitance can induce instability and lower the cycle life. Nevertheless, depending on the electrode/electrolyte combination, this can be resolved.

2.1.1 Electric Double Layer Capacitance (EDLC)

An EDLC, consists of two current collectors and two electrodes which are wetted by an electrolyte solution and separated by an ionically conducting but electronically insulating membrane (Figure 2-1). When a supercapacitor is charged, electrons move from the positive electrode to the negative electrode, while cations and anions in the electrolyte travel to the negative and positive electrode, respectively.

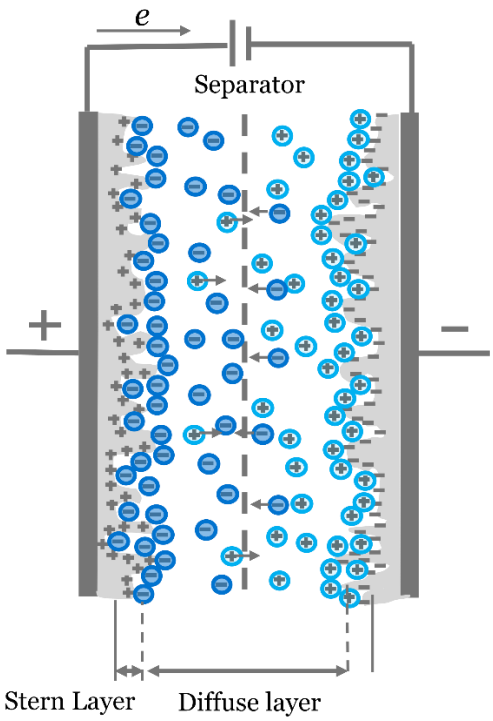

Figure 2-1:Supercapacitor's components

Electric double layer capacitance, as its name implies, works based on double layer theory and was first introduced by Helmholtz in the 19th century. [15] Based on his theory, when a charged surface is placed in an electrolyte, a layer of opposite charge will be created in the liquid medium adjacent to the charged surface. The distance between the two charged layers is only a few solvent molecules and thus only ~Angstroms in thickness. This distance can be approximated by the distance (*d*) of closest approach of an ion to the surface (Figure 2-2, a). This structure resembles the parallel plate capacitor, the capacitance of which can be described using the following relationship:

$$C_d = \frac{\varepsilon\varepsilon_0}{d} \qquad \textit{Equation 2-1}$$

In this equation, ε is the relative permittivity of the medium between the two charged surfaces and ε_0 is the permittivity of free space. Although this theory was the first of its kind, it has some shortcomings: First, the

interdependence of measured capacity and electrolyte concentration or potential is not taken into consideration in this model. Second, the effect of thermal motion of ions is not accounted for.

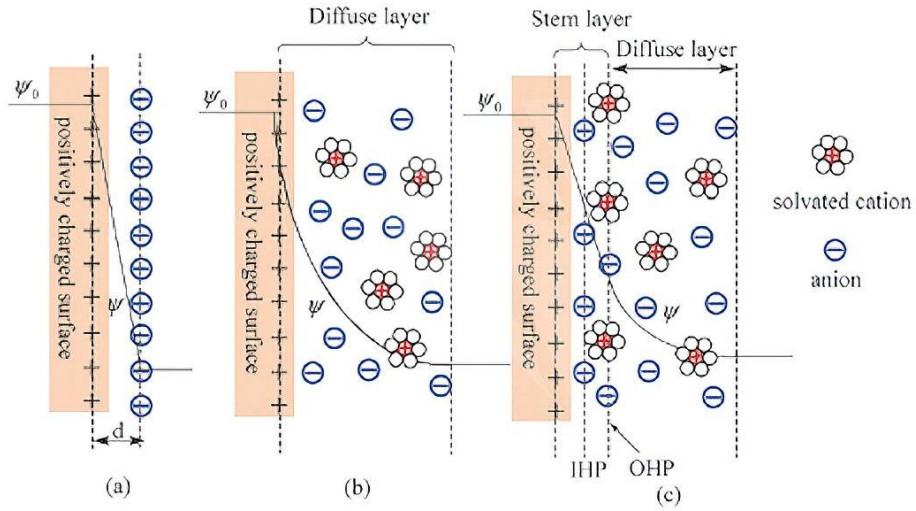

Figure 2-2: Theory of electric double layer capacitor a) Helmholtz model, b) Gouy and Chapman model, c) Stern model

Later, Gouy and Chapman (GC) expanded the Helmholtz model by introducing thermal effects. [16] According to their model, near the surface of electrodes, ions distribute following the Poisson-Boltzmann equation to form a diffuse layer. The potential change over this diffuse layer, for very small electrode surface potential (ϕ_0), is exponential and can be shown as:

$$\phi = \phi_0 e^{-\kappa x} \qquad \textit{Equation 2-2}$$

In this equation, ϕ is the electrostatic potential, x is the distance from the electrode surface, and κ can be defined as:

$$\kappa = \left(\frac{2n^0 z^2 e^2}{\varepsilon\varepsilon_0 BT}\right)^{1/2} \qquad \textit{Equation 2-3}$$

where B is the Boltzmann constant, T is the temperature, e is the charge on each electron, z is the magnitude of charge on each ion, and n^0 is the number concentration of ions in bulk. κ inversed has a unit of length and can define the thickness of diffuse layer, which is most commonly referred to as the Debye length. [16] However, since in this theory ions are considered as point charges, their model overestimates the

capacitance value near the surface of an electrode. This model was further modified by Stern who combined the two models of Helmholtz and GC. In Stern's model, the ion distribution was divided into two regions, the Stern layer (Helmholtz layer) and the diffuse layer. When the ions are solvated, the locus of points corresponding to the counter ion centres is called the outer Helmholtz plane (OHP), while ions which adsorb to the surface without a solvation shell form the inner Helmholtz plane (IHP). [15] Stern demonstrated that the capacitance of these layers (Helmholtz and diffuse layer) add inversely as capacitors in series:

$$\frac{1}{C_{DL}} = \frac{x_2}{\varepsilon\varepsilon_0} + \frac{1}{(2\varepsilon\varepsilon_0 z^2 e^2 n^0/BT)^{1/2}\, cosh(ze\phi_2/2BT)} \qquad \textit{Equation 2-4}$$

x_2 in this relationship is the starting location of the outer Helmholtz plane, e is the charge on the electron, B is the Boltzmann constant, T is the absolute temperature, n^0 is the number concentration of each ion in the bulk, and z is the valency of an ion. The first term and the second terms are related to the Helmholtz layer and diffuse layer, respectively. [16] Therefore, it can be defined as:

$$\frac{1}{C_{DL}} = \frac{1}{C_H} + \frac{1}{C_D} \qquad \textit{Equation 2-5}$$

A graphical description of all three models can be seen in Figure 2-2. This model has expanded to break the potential drop across the interface into various planes to take into account adsorbed vs. solvated ions (inner vs. outer Helmholtz layers) [17] and to include electronic phenomena acting to distribute charge over some distance in materials like semiconductors [18] and semi-metals [19] as will be discussed later for graphene.

2.1.2 Pseudocapacitance Mechanism

In pseudocapacitance, there is a faradaic charge transfer across the electrode/electrolyte interface. These processes can be categorized into three different groups: 1) Adsorption: Adsorption and reduction of an ion (typically a metal cation) onto another metal which happens at potential less negative than the equilibrium potential of the substance (also called underpotential deposition); 2) Redox processes: In these processes current is created as a result of reversible chemical reaction of ions in electrolyte with an electrode

surface; 3) Intercalation: Electrolyte ions such as Li^+ intercalate (insert) into the layered structure of a host electrode materials such as MoS_2, TiS_2 or graphite. This process is reversible and can partially reduce/oxidize the material. [20] The capacitance of pseudocapacitors is between 10 -100 times larger than that of the EDLC. However, due to the slow nature of faradaic reaction, the power density in pseudocapacitors is lower than that of EDLC.[20] In addition, shorter cycle-life is often observed due to the irreversibility of electrochemical reactions and their slow kinetics compared to the spatial rearrangement of charges which has little to no activation barrier. [8] Pseudocapacitors are usually operated with aqueous electrolytes, which as will be discussed have limited voltage stability window. However, recently, redox active ILs have also been developed [21,22] that can improve energy and power density.

2.2 Performance Metrics for Symmetric EDLC

EDLC can be arranged in two common configurations: symmetric and asymmetric. In a symmetric supercapacitor, both negative and positive electrodes are identical, whereas, in an asymmetric one the positive and negative electrodes differ in material, size, and mechanism.

The gravimetric capacitance of an electrode is equivalent to its intrinsic capacitance (double layer capacitance) times its mass specific surface area accessible by the electrolyte: [23]

$$C_G = C_{DL}.SSA \qquad \textit{Equation 2-6}$$

The volumetric capacitance of an electrode is its gravimetric capacitance (C_G) multiplies by its electrode ρ_B:

$$C_V = \rho_B C_G \qquad \textit{Equation 2-7}$$

For a symmetric supercapacitor, the energy density is a function of one electrode's volumetric capacitance (C_V) and the operating voltage (U) of the cell. Therefore, both C_V and U are the determining factors in increasing the energy density and power density of a supercapacitor: [23]

$$E_V = \frac{1}{8} C_V U^2$$ *Equation 2-8*

E_V is the energy density of two EDLC electrodes. The power density can be calculated using the following expression:

$$P_V = \frac{E_V}{\Delta t}$$ *Equation 2-9*

where Δt is the discharge time calculated from GCD plot. The internal resistance of the device (R_{ES}), is calculated by dividing the voltage drop at the beginning of the discharge (U_{drop}) by the applied constant current in galvanostatic charge/discharge plot:

$$R_{ES} = \frac{U_{drop}}{2I}$$ *Equation 2-10*

Thus, to increase the energy density of the device, one would need to maximize the value of ρ_B, SSA, U and C_{DL}. This is challenging in practice as these parameters are often linked. Thus, these values need to be optimized in order to maximize the energy density. [23]

2.3 Electrolyte

Due to the square dependence of the energy density on the operating voltage, this parameter is very important to supercapacitor design. The operating voltage is typically determined by the electrolyte's electrochemical stability window. Aqueous electrolytes are the most common type of electrolyte in supercapacitor research and can be categorized based on their pH value into three main types: acidic, alkaline and neutral electrolyte. However, the operating voltage of aqueous electrolytes is limited thermodynamically to a maximum of 1.23 V for both acid and alkaline electrolyte due to the two water splitting reactions: oxygen evolution and hydrogen evolution, which occur at standard potentials of 0 V vs. SHE (i.e. Standard Hydrogen Electrode) and 1.23 V vs. SHE, respectively. However, in practice for some neutral electrolytes, the voltage window can be enhanced up to 2.3 V. [24] This is due to the existence of lower concentrations of $H^+$and OH^-ion in the neutral electrolyte compared to the acidic and alkaline

electrolyte, which results in a higher overpotential for hydrogen and oxygen evolution reaction. [24] Using aqueous electrolyte also leads to a potentially higher volumetric capacitance due to the smaller ion size of aqueous electrolytes, which could provide them with more accessible surface area as they can reach smaller pore sizes. Furthermore, aqueous electrolyte can initiate faradaic reactions and gives rise to pseudocapacitance.

Organic electrolytes are being used predominantly in commercial supercapacitors due to their high operating voltage of 2.5 to 2.8 V despite being more expensive than aqueous ones. [25] However, organic electrolyte have safety concerns such as flammability, volatility and toxicity. [25] In addition, organic electrolytes have large ion sizes and lower dielectric constant which render them lower capacitance compared to aqueous electrolyte. Organic electrolytes also lack the pseudocapacitance which is available to the aqueous based supercapacitors. The most common organic electrolytes are tetraethylammonium tetrafluoroborate ($TEABF_4$) in acetonitrile or polycarbonate solvents.

Ionic liquids have recently been explored as an electrolyte for supercapacitors due to their larger operating voltage and other outstanding properties which will be discussed in the next section.

2.3.1 Ionic Liquids

Ionic liquids (ILs) are molten salts, with melting point typically below 100 ˚C and are composed of only cations and anions. ILs are also called “designer solvents” due to their tunable physical and chemical properties which can be attained by combining specific types of cations and anions. There are, in general, three kinds of IL, aprotic, protic and zwitterionic. Zwitterionic ILs, as their name implies, contain equal number of positively and negatively charged functional groups making them a neutral compound. These ILs have found application in lithium conducting electrolytes [26] and polymer membranes for Li-ion batteries.[27,28] In contrast, both aprotic and protic ILs are made of cations and anions as two separate molecules. In general, both aprotic and protic ILs are formed when H^+ or R^+ are added to a neutral substance

holding a lone pair of electrons, resulting in the formation of a cation which is paired with a specific anion. The cations that accept H^+ forms protic ILs while the one that hold R^+ can form aprotic IL.[29,30] This distinct difference triggers very unique properties for either of these IL groups. Protic ILs, due to the existence of the proton, are capable of hydrogen bonding and therefore can be used for stabilization of protein,[31] in energy storage to induce pseudocapacitance, [32] or as proton exchange membrane in fuel cell applications. [33] In protic ILs, the ionic compounds are in equilibrium with their neutral counterpart, which will make them partially ionic (note that this depends on the type of ILs). In addition, some protic ILs have larger vapor pressure and can be distilled as a result (i.e., protic ILs with pKa less than 10). [34] On the other hand, aprotic ILs are made of pure ionic compounds, with negligible vapor pressure which make them non-volatile and non-flammable.[29] In addition, they possess high electrochemical and thermal stability, and they are often environmentally friendly compared to most organic electrolytes. These properties have opted aprotic ILs for application in supercapacitors (especially double layer capacitor) and Li-ion batteries. [25] A schematic of these different types can be seen in Figure 2-3.

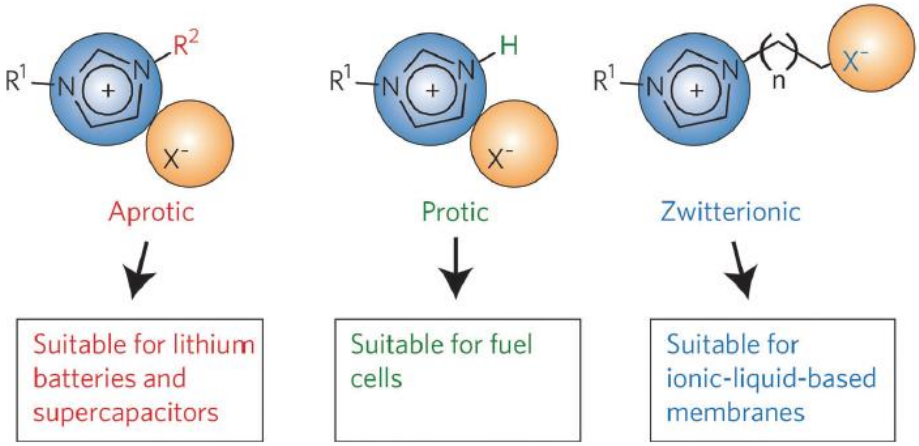

Figure 2-3: Basic types of IL, aprotic, protic and zwitterionic [25]

The cations that are more commonly being used for EDLCs are imidazolium and pyrrolidinium due to their higher ionic conductivity and higher cell operating voltage, respectively, and the anions that are more frequently seen in supercapacitor design are tetrafluoroborate (BF_4^-), hexafluorophosphate (PF_6^-) and bis (trifluoromethylsulfonyl)imide ($TFSI^-$). [25]

Nevertheless, ILs suffer from low ionic conductivity due to their high viscosity, which also typically leads to low specific capacitance especially at high charging/discharging rate due to challenges associated with imbibing nanoporous solids with this more viscous liquid. [25] Figure 2-4 compares the energy density and electrochemical stability window of various anions pairing with imidazolium ($EMIM^+$) for application in graphene-based supercapacitors. [35]

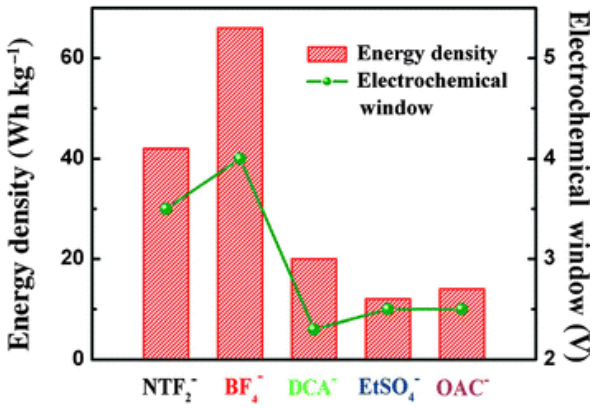

Figure 2-4: Relationship between gravimetric energy density and electrochemical stability windows of EMIM $^+$with various anions for graphene sheet electrode. The gravimetric capacitance were measured using GCD at 1 A/g [35]

2.3.2 Double Layer Capacitance in Ionic Liquids

Since ILs are solvent-free salts, their ionic and electrostatic potential distribution near polarized surfaces cannot be described using Gouy-Chapman-Stern double layer theory. [36] The two main features that arise from having condensed ionic phases, such as the ILs, in contact with electrified surfaces is overscreening and crowding.[36] Overscreening, which is a phenomenon observed at lower potentials, describes a situation where close to electrode surface, the number of counter ions required to neutralize the

charge of the electrode is higher than the original electrode's charge. This will drive more ions in the second layer to screen the counterions. This effect carries on until the electroneutral bulk is reached, resulting in an oscillatory potential and ion density distribution away from the surface of electrode. [36] Overcrowding, on the other hand, occurs at higher potentials, where the counterions cannot neutralize the charge on the electrode and, therefore, line up in front of the electrode, increasing the Debye length and decreasing the capacitance as a result. A schematic describing both phenomena are depicted in Figure 2-5. As a result of this effect, the double layer capacitance shows a camel shaped behavior with respect to potential.

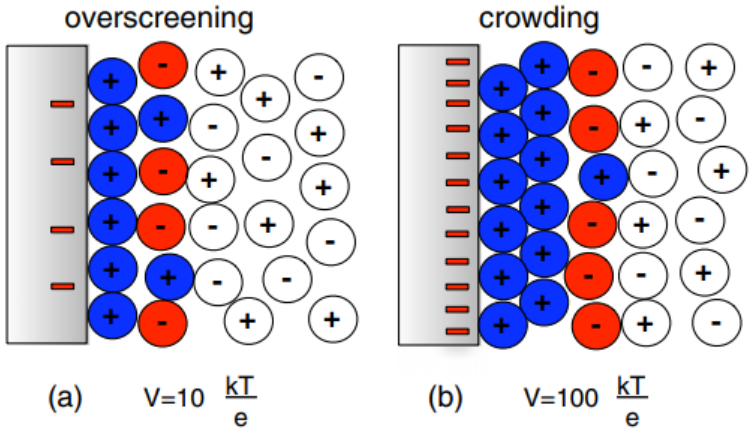

Figure 2-5: Theory of double layer in ILs, a) overscreening of electrode charge at low potentials, b) crowding of counterions on the surface of electrode at high potentials[37]

The minimum of the curve is usually assigned to the open circuit potential (or potential of zero charge), and rises up as a result of overscreening and charge restructuring on the surface of electrode and eventually drops as a result of overcrowding. This curve is usually observed for ILs with lower packing density (i.e., the average concentration of ions in bulk over the maximum concentration of ions on the electrode surface). Figure 2-6 shows an example of a fictitious IL with varying packing density (γ). As it can be observed, the higher the packing density, the sooner the development of overcrowding.

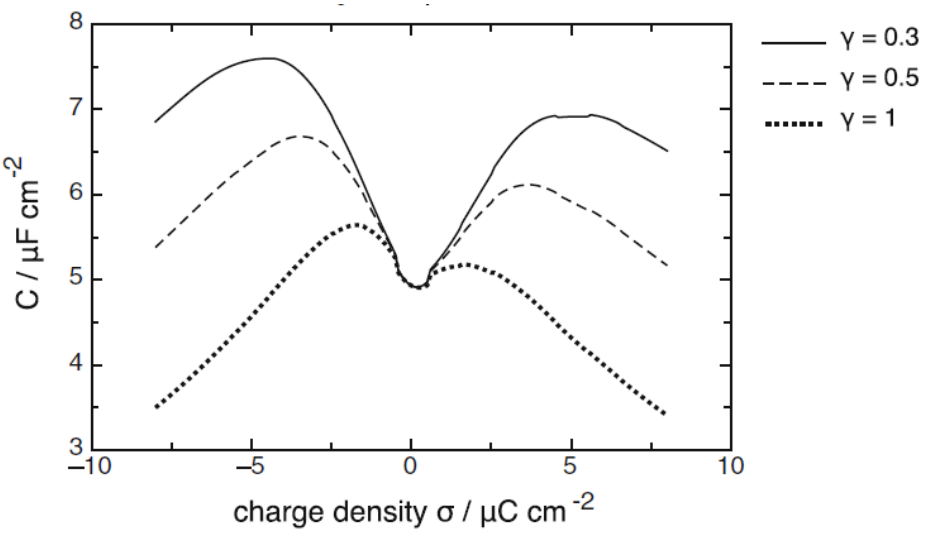

Figure 2-6: Capacity of the interface between graphite and a model IL [38]

2.4 Electrode Materials

The selection of an electrode material has an immense impact on the performance of the supercapacitor and typically defines its type. Carbonaceous materials including activated carbon, carbon nanotubes and graphene are commonly used for EDLCs due to their superior properties such as high chemical and thermal stability, high specific surface area, high conductivity, light weight and low cost. Whereas for pseudocapacitors, conductive polymer and metal oxides are often considered as these materials can support largely reversible faradaic reactions (Figure 2-7). [39]

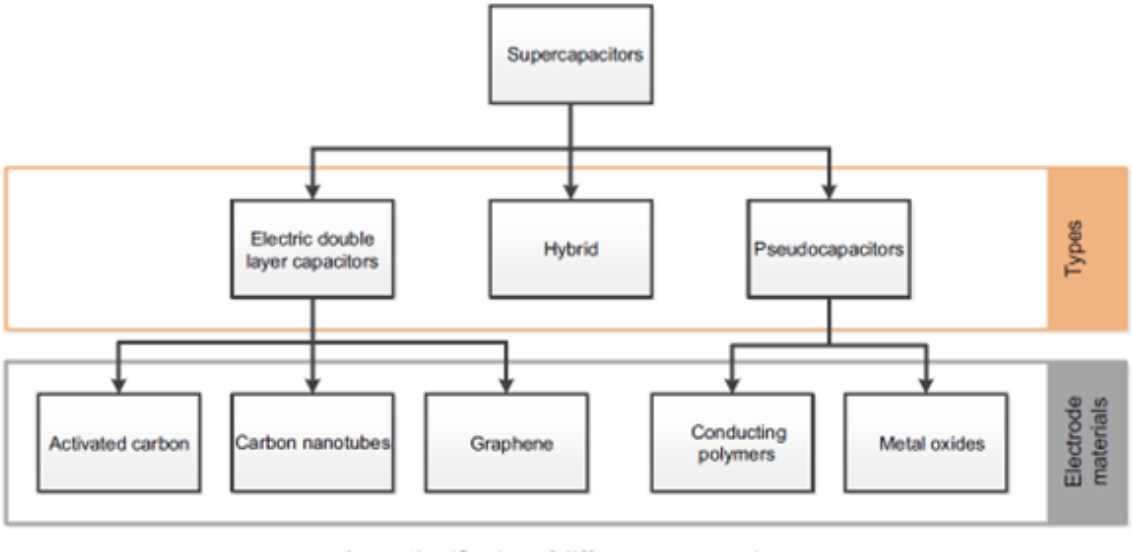

Figure 2-7: Hierarchical representation of supercapacitor electrode materials based on their types

2.4.1 Conductive Polymers

Conductive polymers possess conjugated bond system along their backbone, which will makes them electronically conductive. These polymers display pseudocapacitance, and therefore, they have outstanding capacitance and low internal resistance due to their high conductivity. In addition, they are very cost effective and, since they are flexible, they can be easily processed. The most commonly used conducting polymers are polyaniline (PANI), polythiophene (PTh), poly(3,4-ethylenedioxythiophene) (PEDOT), and polypyrrole (Ppy). The mechanism of charge and discharge in conductive polymers is based on fast faradaic oxidative (p-doped)/reductive (n-doped) processes. As the polymer becomes n-doped (reduced), it will obtain negative charge from the electrolyte which will attract the cations onto its surface, and in p-doping (oxidization) the opposite mechanism happens. [40] Through these charge/discharge mechanisms, conductive polymer can achieve a high capacitance (e.g., capacitance as high as 530 F/g was measured for Ppy).[41] Nevertheless, conductive polymers often have poor cycle life due to their degradation upon repetitive volume shrinkage/expansion.

2.4.2 Transition Metal Oxides

Transition metal oxides also store energy through fast faradic processes, which enables electron transfer between the surface of the electrode and electrolyte. For some metal oxides such as MoO_2, ion intercalation is the main energy storage mechanism. Transition metal oxides, in general, have excellent theoretical capacitance, (e.g., the gravimetric capacitance for RuO_2, CO_3O_4 , and MnO_2 is as high as 2000 Fg^{-1}, 3560 Fg^{-1} and 1380 Fg^{-1} , respectively), [42–44] in practice though, they often can achieve far less capacitance due to their poor conductivity and slow electronic transfer rate, and therefore, they are often used in a composite with carbonation materials or other high conductivity compounds. RuO_2 is an exception with metallic electrical conductivity, high electrochemical stability, and fast and reversible faradaic reaction. The capacitance of 498 Fg^{-1} in 0.5 M H_2SO_4 was reported for this material. [45] However, its toxicity and high-cost limits its large-scale production and application.

2.4.3 Carbon Nanotubes:

Carbon nanotubes (CNT) such as multiwalled nanotubes (MWNTs) and single walled nanotubes (SWNTs) are made of individual rolled graphene sheets. Thus, they possess high electrical conductivity, high thermal conductivity, chemical inertness and mechanical stability. The tubular structure of CNTs offer mesopores which are readily available to the electrolyte. However, CNTs often form bundles due to the van der Waals interactions between the tubes, which, reduces their SSA and capacitance. The capacitance reported for these materials are usually limited to 15 to 80 Fg^{-1}, with SSA between 120 to 400 m^2g^{-1}. [46] Vertically aligned CNTs have been proposed as a solution to such problems enabling excellent rate performance as a result of their open mesoporous structure. [47–49] To increase the specific capacitance further, subsequent chemical oxidation was proposed, which introduces functional groups, resulting in pseudocapacitance.[50] Niu et al. [51] combined vertically aligned MWNTs with oxidative treatment and was able to increase the SSA to 430 m^2g^{-1} and the capacitance to 102 Fg^{-1}. Chemical activation of CNT has also

been successful in further increasing the SSA and capacitance.[52] However, there is a limitation on maximum achievable capacitance from CNT, therefore, they are often combined with conductive polymer[53] as composite to induce pseudocapacitance, which adversely impact their cycle life.

2.4.4 Activated Carbon (AC):

ACs are widely being used in commercial EDLCs due to their high specific surface area and low cost. ACs can be produced by carbonization and activation of carbon rich organic precursors such as coconut shell,[54] silk, [55] lignin [56] etc., as well as synthetic materials such as thermosetting polymers. The carbonization process can be done by heating the precursor in an inert atmosphere. Carbonization will cause thermal/chemical conversion (pyrolysis) of the precursor and further increase in the temperature (>2500 °C) induces graphitization.[57] Carbonization is often followed by subsequent oxidation (activation) in the presence of oxidizing gas such as CO_2, air and steam (700 – 1100 °C), or using activating agent such as sodium hydroxide, potassium hydroxide and phosphoric acid (400-700 °C).[57] Activation process creates hieratically porous structure containing micropores (< 2 nm), mesopores (5-50 nm) and macropores (> 50 nm). The theoretical SSA of AC is estimated to be ~ 3000 m^2g^{-1}. However, this value is often not achieved practically and SSA reported for ACs are usually between 1000 to 2000 m^2g^{-1}.[58] Even with this relatively high specific surface area, the value of capacitance achieved with AC electrode ranges only between 100-300 F/g for aqueous and > 150 F/g for organic electrolytes.[59,60] This is often due to inaccessibility of certain pores specially micropores to electrolyte as well as electrode/electrolyte wetting issue. Therefore, research in this area is mainly focused on engineering the porous structure of ACs for certain electrolyte by considering the electrolyte ion sizes.[61,62]

2.4.5 Graphene-based Materials

Graphene for the first time was introduced by Geim and coworkers,[63] who mechanically exfoliated graphite using micromechanical cleavage into a one atom thick structure called graphene.

Today, many different methods have been developed for the fabrication of graphene such as chemical vapor deposition of graphene;[64,65] micromechanical exfoliation of graphite using AFM or adhesive tape, [63] chemical oxidation of graphite[66] followed by a reduction step, or the milling of graphite in particular solvents.[67] Among these methods, the chemical oxidation of graphite into graphite oxide and the subsequent reduction of the product into reduced graphene oxide (rGO), which have some of the properties of graphene sheets, is a common method frequently observed in the literature for creating graphene. Graphite oxide and its common reduction methods will be discussed in the upcoming sections.

Aside from the high specific surface area that was mentioned earlier in the introduction for graphene (i.e., 2650 m^2/g), graphene has other extraordinary properties including the capability of sustaining high current density, ballistic transport properties (i.e., transport with negligible scattering), chemical inertness and mechanical strength. In addition, its large surface area and tunable band-gap have made graphene a promising candidate for electronic devices and electrode materials.[68,69] Graphite, which is compacted graphene layers, has the highest density among other conducting carbons (i.e., 2.2 g/cm^3) with interlayer spacing of 0.33 nm.[23]

Graphene is composed of a single layer of carbon atoms packed in a hexagonal lattice structure of sp^2 hybridized carbon atoms. In this configuration, each carbon atom is connected to the next carbon atom by a sp^2 hybridized bond forming a continuous aromatic network. Each graphene sheet within graphite is bonded by weak $\pi - \pi$ interactions to the upper and lower graphene sheet allowing the layers to be exfoliated.

When an electrical potential is induced through a graphene sheet exposed to an electrolyte, the capacitor that develops can be divided into two parts: One part is the contribution from the solid called quantum capacitance, which is the intrinsic capacitance of the electrode materials as a result of accumulation of charges within few angstroms away from the electrode surface.[70] This distribution of

charge create a capacitance often smaller than the electrolyte contribution or double layer capacitance. The other part is the contribution from the electrolyte which entails Helmholtz layer and diffuse layer as discussed above:

$$\frac{1}{C_{DL}} = \frac{1}{C_H} + \frac{1}{C_D} + \frac{1}{C_Q} \qquad \textit{Equation 2-11}$$

The diffuse layer capacitance in a concentrated electrolyte (i.e., > 0.1M) is larger than the Helmholtz layer capacitance. Therefore, it can be neglected in the final calculation of the double layer capacitance. The quantum capacitance, on the other hand, does have an effect in the final interfacial capacitance because it is normally the smaller value.[9]

For a single layer of graphene, the quantum capacitance (intrinsic capacitance) can be described by:[9]

$$C_Q = \frac{2e^2}{h v_F \sqrt{\pi}} \sqrt{n} \qquad \textit{Equation 2-12}$$

In this equation, h is the Planck constant, e is the charge of electron, v_F is the Fermi velocity of the Dirac electron and n is the charge carrier concentration (electronic density of states). According to the literature, charged impurities can make a major change in the transport properties of graphene.[71] By increasing the number of defects, functional groups and impurities, we can increase the density of state (DOS), which will be reflected in the quantum capacitance of graphene. The double layer capacitance measured for the IL of $BMImPF_6$, is around 21 μF/cm^2.[9] For aqueous electrolyte, this value typically ranges between 16 to 35 μF/cm^2 depending on the distance of closest approach of the ion to the surface as defined by the Helmholtz layer. Using the theoretical specific surface area of graphene, and assuming C_{DL} ~ 20 μF/cm^2, the upper value obtained for the capacitance of graphene-based materials would be around 450 F/g for graphene with high DOS (i.e., in the order of 10^{23} to 10^{24} eVcm^{-3}) and intrinsic capacitance of above 100 μF/cm^2 .[8]

2.4.6 Graphite Oxide Synthesis

Graphite oxide, a derivative of graphite, has been synthesized for the first time in 1860 by Brodie using $KClO_3/HNO_3$ as oxidizing agents. [72] In 1898, Staudenmaier had improved Brodie's method by using H_2SO_4 and fuming HNO_3 and adding chlorate over the course of the reaction.[73] Later, the Hummer's method was developed in 1958 which used three main components as oxidizing agents (i.e., $KMNO_4$, $NaNO_3$ and H_2SO_4).[74] Although this method was widely used in the literature, it can produce toxic/explosive gases such as NO_2, N_2O_4 and CIO. Later, Tour's group developed a modified version of Hummer's method, which replaced sodium nitrate with phosphoric acid (with the ratio of 9/1 for H_2SO_4/H_3PO_4) and increased the amount of potassium permanganate. Using this new method, graphite oxide is more oxidized plus, no toxic gas is generated during the synthesis, and therefore, the temperature is easily controllable.[66] Tour's modified Hummer's method is being widely used for synthesis of graphite oxide from graphite. Graphite oxide can then be delaminated using high shear stirring or sonication into graphene oxide (GO). Both graphite oxide and GO are widely being used in various applications (e.g., host materials for molecular recognition, conductive composites, ultrathin carbon film, energy storage etc.)[75–78] However, a clear structural model for these materials is really hard to define due to: i) GO is a non-stochiometric compound and its composition slightly changes depending on the synthesis method; ii) It is strongly hygroscopic; and iii) It slowly decomposes at around 60-80 °C.[79] Yet, there have been several attempts to propose a model that can best describe this compound among which Lerf-Klinowski's model based on solid state NMR study found the most popularity.[80–83] In their model, GO was depicted as an amphiphilic compound with regions of flat six member ring benzene surrounded by regions of oxidized, wrinkled alicyclic six-membered ring of bearing carbonyl (-C=C) , hydroxyl (C-OH), and 1,2 ether groups, while on the edges GO is decorated with carboxyl (COOH) and hydroxyl groups.[79]

2.4.7 GO Reduction Methods

rGO which is made from reduction of GO has been widely reported in the literature. Although there are several different methods to produce rGO, here it suffices to briefly list the different methods, but we will explain the most common ones in more details. In general, rGO production can be through chemical,[84–86] thermal,[8,87,88] laser, [89] microwave,[90,91] plasma, [92] hydrothermal, [93] electrochemical reduction [94] etc. Among these methods chemical and thermal reduction methods are the most widely used and reported in the literature due to their ease of processing. Therefore, we will review them more thoroughly.

Chemical reduction methods often use a reducing agent in aqueous solution or organic solvents. Among the chemical reducing agents, the most common ones are hydrazine hydrate [84] and different sodium compounds such as sodium borohydride, [86] sodium cholate [85] etc. Other reducing agents can be named as ascorbic acid, [95] hydroiodic acid [96] and hydrobromic acid.[97] Hydrazine hydrate reducing agent, first introduced by Ruoff's group, [84] has gained popularity in the energy storage application. The C/O ratio reported for hydrazine reduced GO is around 10 with BET surface area of ~ 466 m^2/g which is far below the theoretical surface area of graphene (2630 m^2/g) due to agglomeration of rGO upon reduction. [84] It is also worth mentioning that this method induces nitrogen doping on the final product with C/N ratio of ~ 16 .[84] Hydrazine reduced method was further modified according to principle of colloidal science to produce stable aqueous dispersion of rGO (Wallace method).[98] In this method, by tuning the pH to ~ 10 or 11 (for the GO concentration of 0.5 mg/ml or lower), the remaining negatively charged carboxylic acid groups on rGO can stabilize the dispersion through electrostatic repulsion resulting from zeta potential of ~ 43 mV. [98] As it is well demonstrated in colloidal science, zeta potential of lower than -30 mV is essential for a stable colloidal dispersion.[99]

Thermal reduction of GO has also been widely used for scalable production of rGO. According to Schniepp et al., [87] application of rapid heating (>2000 °C/min) up to a temperature of 1050 °C will expand

graphene sheets by CO_2 evolution resulted from reduction by-products. However, it was shown that the presence of some functional groups and defects will improve the quantum capacitance of graphene due to increase in the number of DOS. [9] An increase of up to 3 to 4 fold in the intrinsic capacitance of rGO was reported with an increase in the density of functional group up to a certain value (usually with C/O ratio of 10 - 20). However, there would be a trade-of between the gain in capacitance and reduction of electronic conductivity, the latter will be manifested as lower rate performance in supercapacitors. [8,88] The best performance was observed for reduction at 1100 °C for 1 min. [8] The loss of electronic conductivity in GO and mildly reduced GO is due to the presence of sp^3 hybridized domain between the sp^2 domain, which will cause electron hoping mechanism of conductivity rather than ballistic (the ballistic transport occurs in purely sp^2 hybridized carbon). At ~ 10% oxygen level, a percolated sp^2 network forms and with further reduction, the band gap decreases resulting in metallic characteristic of graphene.[100] It is therefore worth mentioning that by using thermal reduction method, the electronic properties and DOS of rGO is highly tunable with modification in reduction time and temperature.

2.4.8 Review of Graphene based EDLC

Since Stroller et al. [10] has introduced the first use of rGO in supercapacitors, there has been a large number of attempts to improve the SSA of rGO using a physical spacers. Samulski et al.[11] who pioneered using a physical spacer was able to increase the BET surface area to 862 m^2/g from 44 m^2/g, which increased the capacitance from 14 F/g to 269 F/g in 0.5 N H_2SO_4. In another attempt, Kar et al.[101] have used 1-pyrenecarboxylic acid (PCA) as a spacer that exfoliates graphene flakes, acting much like a molecular wedge. The PCA/graphene dispersion showed high conductivity (since this method does not compromise sp^2 hybridization) in addition to improving the specific surface area of the material. The specific capacitance in 6 M KOH was around 120 F/g with impressive power density of 105 kW/kg and energy density of 9.2 Wh/kg. Examples of the use of other spacer materials such as surfactant,[13] carbon black,[14] mesoporous

carbon,[102] carbon nanotubes [12,103,104] are plentiful in the literature. Although this method is effective in preventing graphene nanosheet from restacking, some problems are associated with it. Using a spacer between the graphene nanosheet will reduce the effective density of the active materials, compromising the energy density of the supercapacitor. Also, using a spacer will create a predefined porous structure that might not necessarily match the sizes of the electrolyte ions. Therefore, in many of these studies, the electrolyte of choice is aqueous which have the smallest ion size. In another approach by Dan Li group,[23] water was used as spacer. Due to the presence of some hydrophilic groups on rGO they can retain water and therefore, the repulsive hydration force prevents the sheets from restacking. This approach leads to unprecedented value of 191.7 F/g and 255 F/cm^3 for gravimetric and volumetric capacitance, respectively, in aqueous electrolyte. Using this solvent exchang, they were able to replace the hydration layer of water with organic electrolyte, which increased the capacitance to 261 F/cm^3. Furthermore, this approach leads to incredible rate performance as a result of already solvated chemically reduced graphene. However, this approach is based on vacuum filtration techniques, which is a time consuming and impractical method. Pope et al [105] have developed a new strategy by incorporating hydrophilic IL into the electrode structure. For this purpose, they dispersed GO in water and introduced hydrophilic IL to the mixture which then formed a gel-like structure, proceeding by drying off the excess water from the mixture and reducing the dried composite by heat treatment. The final product had a specific capacitance of 140 F/g. This work nevertheless, did not utilize intermolecular interaction between IL and graphene surface which would have assisted in the wetting and even distribution of ions. To further expand upon this method and increase the specific capacitance, She et al.[106] have developed an alternative method to incorporate the IL nanodroplets between graphene sheet using a microemulsion system. To achieve this, they used a non-ionic surfactant (Tween 20) to emulsify 1-ethyl-3-methylimidazolium bis(trifluoromethylsulfonyl)imide (EMImTFSI) in water. This emulsion system adsorbed onto the GO nanosheet layer spontaneously. The final slurry was drop casted onto the current collector and dried overnight at room temperature. The GO-microemulsion

composite was further reduced using a thermal reduction method which also evaporated the surfactant (Figure 2-8). The specific capacitance obtained by incorporating 60% IL into graphene nanosheets was around 189 F/g and 145 F/cm^3 at room temperature and 282 F/g and 218 F/cm^3 at 60° C. Furthermore, this method produces high energy density and power density of 67.8 Wh/L and 561.4 W/L, respectively, due to using ILs as electrolyte. This method was also applied to MXenes and rGO micro supercapacitor with improved performance.[107,108]

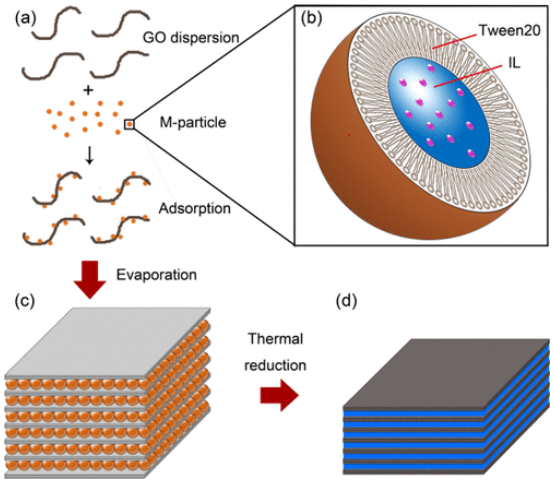

Figure 2-8: Schematic of the fabrication process for IL-mediated reduced GO. (a) Spontaneous adsorption of M-particles on GO surface, (b) enlarged view of EMImTFSI/Tween 20/H2O M-particle, (c) film structure after drop-casting, (d) film structure after removal of Tween 20 [106]

Liu et al.[109] introduced a new approach to overcome the van der Waals attraction by creating curved graphene that can act as spacer. Using high voltage window IL of $EMImBF_4$, they were able to achieve record high energy density of 86.5 kW/kg at room temperature, and 136 kW/kg at 80 °C. The specific capacity of 154.1 F/g was reported for this electrode at 1 A/g current density. Later Luo et al. [110] used crumbled GO for fabrication of electrode materials and demonstrated that this structure outperformed flat chemically converted graphene sheets and wrinkled sheet. According to their study, crumbling GO improved the ohmic resistance, as well as rate performance, plus, scaling up the electrode mass to 20

mg/cm^2 did not change the capacitance at low current density of 0.1 A/g (Figure 2-9). A gravimetric energy density as high as 150 F/g at 0.1 A/g was reported in 5 M KOH solution. Nevertheless, this method potentially leaves large gaps between sheets that will reduce the density of the electrode resulting in reduction of the volumetric energy density.

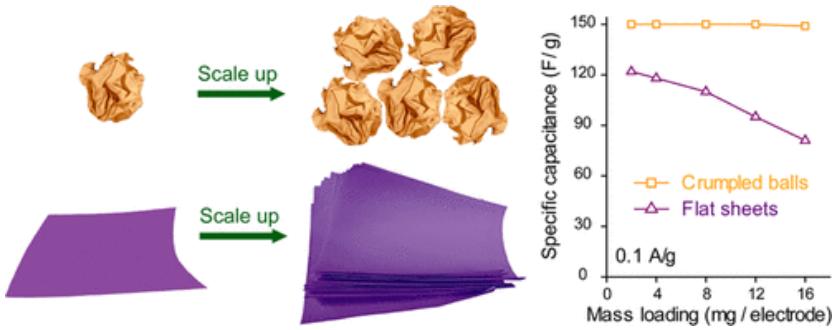

Figure 2-9: Performance of crumbled graphene vs. flat graphene in scaling up [110]

Holey graphene, which is perforated graphene made with exposing GO to H_2O_2 in a hydrothermal reactor has been successful in improving the SSA as well as ion diffusion in electrode. The record high gravimetric and volumetric capacitance of 289 F/g and 209 F/cm^3, respectively, was reported for this material in $EMImBF_4$. In addition, the electrodes maintained high performance even at high loading of 10 mg/cm^2.[111]

Another effective method to increase the SSA of rGO is activation. Zhu et al.[112] used activation of microwave exfoliated graphite oxide (a-MEGO) with KOH to create both micropores and mesopores within the microwave exfoliated and reduced graphite oxide. The reported BET surface area of the resulting a-MEGO was 3100 m^2/g which yielded C_G of 165 F/g while C_V reached 59.8 F/cm^3 in $EMImBF_4$/AC electrolyte.[112] They later modified their method by producing crumpled GO using spry drying of aqueous GO. These crumbled GO then went through microwave exfoliation and KOH activation to produce macro

and mesopores with BET surface area of 3290 m^2/g. This modification resulted in C_G and C_V of 173 F/g and 102 F/cm^3, respectively in EMImTFSI/AC electrolyte.[113]

Another series of studies were focused on getting a synergistic improvement in capacitance of graphene by combining it with pseudocapacitive materials such as conductive polymers (PANI,[114–116] Ppy,[117]), and metal oxide (MnO_2,[118] RuO_2 [119]) as composite materials. Zoa et al.[114] have investigated the synergic combination of graphene with PANI. In this work, the composite was made by in situ polymerization of aniline monomer in the presence of GO in acidic condition, followed by reduction with hydrazine hydrate. PANI was further reoxidated and reprotonated to give rise to PANI/graphene composite. The specific capacitance of 480 F/g in 2M H_2SO_4 at 0.1 A/g was reported for composite with 80 wt. % GO. While the BET surface area was quite low (4.3-20.2 m^2/g), this increased in capacitance is attributed to the pseudocapacitance from PANI. The cycle stability improved compared to that of PANI alone, indicating the effect of graphene. In all these studies, due to the pseudocapacitance arising from the redox active materials, the capacitance increases, and the cycle stability improves compared to the case with redox active materials alone. However, to induce pseudocapacitance, aqueous electrolyte is often being used in these studies, in practice though, aqueous electrolytes are not being used in commercial applications due to their low voltage windows and low energy density. Commercial supercapacitors are based on organic electrolyte, which, as it was discussed earlier, are flammable and toxic. As a result, research in this area should focus on using more environmentally friendly and safer electrolytes. Aprotic ILs with their high electrochemical stability window, wide operating temperature (-40 – 200° C) non-flammability, and nontoxicity can provide an excellent replacement. Rao et al. [120] reported the first use of ILs for graphene-based supercapacitors. However, their specific capacitance was fairly small (75 F/g), with an energy density of 31.9 Wh/kg. This can be attributed partly to the graphene-based materials tendency to agglomerate; however, the other issue is the wettability of rGO by the IL which is an important hurdle to overcome. To improve the wettability

of IL with graphene-based materials, Kim et al. [121] synthesized a poly(ionic liquids)/rGO composite, with EMImTFSI as electrolyte (Figure 2-10). This novel technique yielded a capacitance of 187 F/g and maximum energy density of 6.5 W/kg and power density of 2.4 kW/kg.

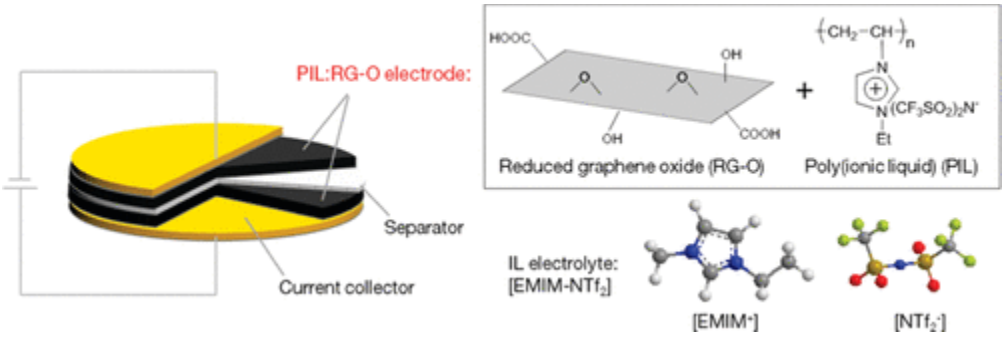

Figure 2-10: Schematic of Poly-ionic liquids/rGO combination for improvement in wettability of IL on rGO surface.[122]

2.5 Summary of Challenges and Thesis Layout

As it was briefly mentioned in Section 1, supercapacitors offer excellent power capability but suffer from low energy density which makes them inferior to batteries in applications where energy is needed for longer period of time such as use in electric vehicle. Therefore, the main challenge in research associated with supercapacitors is to improve their energy density and, particularly, their volumetric energy density. Increasing volumetric energy density requires an increase in electrode's SSA while maintaining its high ρ_B. As it is very challenging to maintain both high ρ_B and SSA, optimizing the pore size of electrode for certain electrolyte ion sizes is the best strategy as is depicted in Figure 2-11.

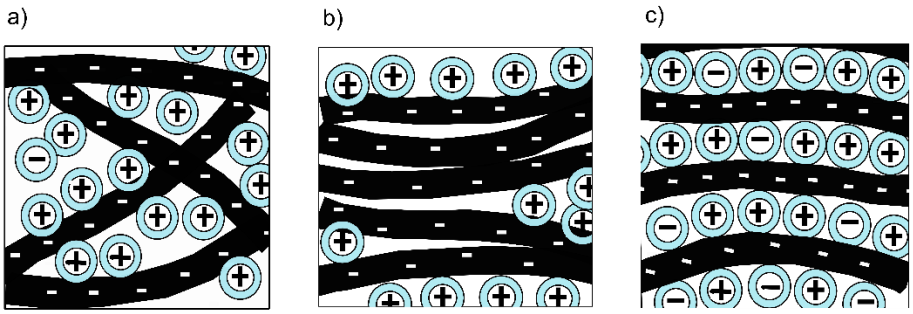

Figure 2-11: Challenge of increasing SSA and ρ_B a) increase in SSA but reduction in ρ_B, b) increase in ρ_B but reduction in SSA, c) optimizing the SSA and ρ_B by matching the ion size with pore size

In addition, as it was mentioned in Section 2.4.5, the electrode is required to have high quantum capacity, which originates from large number of DOS. For graphene, this means having defects and disorders in the structure which can often be achieved by reducing GO. Therefore, the degree of reduction is essential in achieving high number of DOS. On the electrolyte side, the main focus should be on using electrolytes with high electrochemical stability windows such as ILs. Furthermore, the double layer capacitance is dependent on the electrode/electrolyte combination. Therefore, an electrolyte which can provide high C_{DL} and large electrochemical voltage window is required. It is also important to note that while optimizing these parameters for improvement of $E_{V,}$ the cycle life and power performance should not be compromised since these parameters are the primary advantage of supercapacitors over batteries. As it was outlined in Section 1 and further discussed in Section 2.4.8, rGO has been proven as an effective energy storage material given its high DOS, electronic conductivity and theoretical SSA of 2670 m^2/g. Nevertheless, due to sheet-sheet van der Waals attraction, it will lose considerable amount of its mass specific surface area. Thus, using an electrolyte to create space between graphene sheets can be an effective strategy to overcome its interlayer van der Waals attraction while optimizing electrode spacing for the electrolyte being used. This idea was implemented by She et al.[106] using non-ionic surfactant of Tween 20 as self-assembly media and carrier for IL molecules. In his study, surfactant was self-assembled with

hydrophobic IL (EMImTFSI) in aqueous media, and the resulting nanostructures were instantly adsorbed on the GO surface. The following dispersion of IL/surfactant/GO was drop cast, dried and heat treated to evaporate the surfactant and reduce GO. Nevertheless, the heat treatment process posed some technical challenges such as: i) partial degradation of the IL; ii) incomplete reduction of GO which results in low electronic conductivity (due to limitation imposed by thermal decomposition of IL); iii) a large volume of surfactant was necessary for the self-assembly (4:1 surfactant to IL) which resulted in the evolution of large pores on electrode surface as surfactant is removed by evaporation/decomposition . This lowered the ρ_B of the electrode. In this research, we tried to tackle these challenges by exploring the possibility of eliminating the heat treatment, and lowering the volume of surfactant used. Thus, we investigate the double layer formation with the presence of these surfactants. Aligned with the aforementioned, in Chapter 3, we studied the self-assembly of surfactant/IL in water using multi angle dynamic light scattering (DLS) and their self-assembly on GO surface using fluorescence spectroscopy, and AFM. In this study we explored the possibility of using TX-100, as self-assembly media and compared its adsorption behavior with that of Tween 20. Using TX-100, the effective mass ratio of surfactant/IL was lowered to 3 (compared to 4 for Tween 20), while the adsorption isotherm of TX-100/IL was identical to Tween 20/IL. The surface roughness and thickness of the adsorbed layers were measured and compared. The thickness values reported from AFM correlated closely with the interlayer spacing of the dried composite film of GO/surfactant/IL calculated from the XRD diffraction angles. Finally, P123, a triblock copolymer with ability to stabilize IL in even lower surfactant/IL ratio of 1, was also studied and the adsorption properties of its complexation with IL on GO surface was compared with that of TX-100/IL and Tween 20/IL systems.

In Chapter 4, we studied the C_{DL} of self-assembled IL/TX-100 on glassy carbon using impedance spectroscopy. We then compared its C_{DL} with P123. In addition, the ionic conductivities of the two assemblies were measured using impedance spectroscopy, and then compared with the calculated ionic

conductivities using diffusivities from PFG-NMR and the measured viscosities of the electrolyte mixtures. And finally, we calculated the apparent hydrodynamic radii of each electrolyte mixtures and related that to ionic correlations in the electrolyte. Using this analysis, P123 appeared to be more effective in reducing the ionic correlations in the electrolyte mixture being studied.

Chapter 5 is dedicated to exploring the possibility of replacing GO with rGO and eliminating the heat treatment step. On the same note, using our finding from the first and second projects, we created self-assembly of IL/P123 on rGO at different weight ratio of IL/P123 and percentage of surfactant and evaluated the performance of the electrodes for each combination. For this process, we used freeze drying to lock in the self-assembled structures while evaporating the water, which resulted in a fluffy powder that was assembled onto current collector using a press die. Using this method, we were able to optimize the performance of the electrode in terms of both volumetric and gravimetric capacitance. We further enhanced the rate performance of the electrodes and capacitance retention of 80% after 10000 cycle was achieved.

Chapter 3

Aqueous, Mixed Micelles as a Means of Delivering the Hydrophobic Ionic Liquid EMIM TFSI to Graphene Oxide Surfaces

Most ionic liquids (ILs) are not surface-active and cannot, alone, be directed to assemble at surfaces – despite their potential as non-volatile structure-directing agents and use as advanced materials in a multitude of applications. In this chapter, we investigated aqueous systems of common non-ionic surfactants (Triton X-100 and Tween 20) which we use to solubilize 1-ethyl-3-methylimidazolium bis(trifluoromethylesulfonyl)imide. The resulting solution of mixed micelle leads to spontaneous adsorption of the IL/surfactant complex onto graphene oxide (GO) surfaces, forming a compact film. Adsorption isotherms generated by fluorescence labeling of the IL and surfactant phases are used to quantify the extent of adsorption. While sensitive to the GO dispersion concentration, upwards of 3 g IL/g GO adsorb under dilute conditions. Atomic force microscopy is used to show that the adsorbed layer uniformly distributes as a ~1 nm thick coating (per graphene oxide side) as the system reaches the first plateau of a Langmuir-type isotherm. Adsorption beyond this plateau is possible but leads to thicker (> 30 nm), inhomogeneous adsorbed layers. Both micellar size in solution and adsorbed layer thickness reduce upon addition of IL to the surfactant phase suggesting significant interactions amongst the materials and non-ideal mixing of the components.

The result of this chapter was published in Langmuir as: Aqueous, Mixed Micelles as a Means of Delivering Hydrophobic Ionic Liquids to Graphene Oxide Surfaces. [123]

I designed the experiments in consultation with Dr. Michael Pope. The experiments were performed entirely by myself. I also wrote the manuscript for publication and Dr. Mahshid Chekini and Dr. Pope helped with organization and editing of the manuscript for publication. Dr. Pal helped with editing of the manuscript. This project was funded by NSERC discovery grant.

3.1 Introduction

Ionic liquids (ILs) are salts with melting points lower than 100° C and composed entirely of ions.[124] Due to their strong solvation power, high ionic conductivity, thermal stability and effective non-volatility (enabling easy recycling), ILs are being increasingly used for green chemical synthesis,[125] separation[126,127] and, more recently, to engineer nanostructured materials[128,129] and electrochemical devices such as batteries[130,131] supercapacitors[7,132,133] and sensors.[134] In the latter applications, the IL is used as a functional device component (i.e., the electrolyte) or template for the growth of nanoparticles or mesoporous materials. Directing the spatial distribution of the IL phase on solid support through methods such as self-assembly is becoming increasingly important to furthering these and future applications.[106]

Various self-assembly phenomena have been explored using ILs over only the past two decades.[135,136] When mixed with non-ionic surfactants, ILs are capable of supporting micelle formation[137–140] and in ternary systems can form microemulsions[140] or mixed micelles.[141] For example, so-called microemulsions of ILs have been used extensively as nanoreactors to grow various nanoparticles.[142–144] Using microemulsions of ILs for enzyme storage under harsh conditions is another example.[145] These microemulsions can also be used as a vehicle to decorate nanoparticles on a surface of choice creating ordered composites with desired properties.

While a significant amount of work has been carried out to examine surfactant adsorption onto various surfaces,[146–151] little is known regarding the surface adsorption behavior of the mixed IL/surfactant systems discussed above. In this study, we aim to provide a more detailed analysis of the adsorption behavior and adsorbed layer structure of both the IL/Tween 20 system as well as the more commonly used IL/TX-100 system on GO surfaces. Using dynamic light scattering (DLS) and the fluorescent probes Rhodamine B (Rh B) and pyrene, which partition into the IL phase and surfactant phases, respectively, we elucidate the structure of the micellar system and the adsorption behavior onto GO. We also use non-contact, tapping

mode, AFM to probe the distribution and morphology of both surfactant and IL/surfactant adsorbed layers on dried films at various points in the adsorption isotherms. These results provide a useful starting point to understanding the adsorption behavior, adsorbed layer structure after drying and how to better assemble various GO/IL composites for future applications.

3.2 Experimental Methods

Materials:

All reagents were used as received. 1-Ethyl-3-methylimidazolium bis-trifluoromethylsulfonyl)imide (EMImTFSI) was purchased from Io-Li-Tec (99% purity). TX-100 and Tween 20 were purchased from EDM Millipore corporation and Sigma-Aldrich, respectively. Pyrene and Rhodamine B were both purchased from Sigma-Aldrich

Methodologies:

GO was synthesized from natural flake graphite (Alfa Aesar, 99.9% purity, -10 mesh) according to Tour's modified Hummers' method. [66] In this method, a mixture of 3 g of graphite flakes, 360 mL sulfuric acid, 40 mL phosphoric acid and 18 g potassium permanganate were heated overnight at 45°C in a round bottom flask. After 16 h, the resulting thick purple slurry was added slowly to deionized (DI) water (around 200 ml) which was placed in an ice-cold water bath. H_2O_2 was added slowly to the dispersion to reduce unreacted potassium permanganate which changed the dispersion color from brownish/purple to bright yellow. The resulting GO was washed twice with 10 % hydrochloric acid and 4 times with ethanol by centrifugation using Fisher Scientific accuSpin3 at 3000 rpm for 30 min. Then it was dispersed in DI water and dialyzed for ~4 days until the pH of the dispersion was ~4.

The synthesized GO has a C/O ratio of 1.67 (by atomic ratio) which was analyzed by energy dispersive X-ray spectroscopy (EDS) using a field emission scanning electron microscope (SEM, ZEISS Ultra Plus FESEM). The samples were prepared by drop casting aqueous dispersion of GO (5 mg/ml) several times

on the substrate until a thick layer of material was deposited. The spectra were taken under 1000× magnification, using 10kV acceleration voltage.

DLS was performed on the micellar structures using a Brookhaven laser light scattering instrument, with a BI200SM goniometer and a 636 nm laser source. The analysis of the time correlation function was performed using GENDIST software. The samples were prepared at 1.33 wt.% for TX-100 and at 1.76 wt.% for Tween 20 since any lower concentration would result in an average count rate lower than 100 kcps. The prepared samples were then filtered using 0.1 μm pore size filter to eliminate any dust or large aggregates. The measurement was performed at different angles of: 60°, 75°, 90°, 105°, 120°, 135°, 150°. Each test was repeated three times. For each angle, the decay rate (Γ) was calculated through analysis of the DLS data, and the magnitude of scattering angle was calculated using the equation:

$$q = {}^{4\pi n}/_{\lambda_0} \, sin\frac{\theta}{2} \qquad \textit{Equation 3-1}$$

where n is the refractive index of the solvent, λ_0 is the vacuum wavelength of the incident light, and θ is the scattering angle in radians. The data were then plotted using a scatter plot and a linear curve was fitted to the data points according to the relation: [152]

$$\Gamma = Dq^2 \qquad \textit{Equation 3-2}$$

The slope of the curve was taken as the diffusion coefficient (D). Using the Stoke-Einstein equation, the hydrodynamic radius can be estimated as:

$$R_h = \frac{BT}{6\pi\mu D}, \qquad \textit{Equation 3-3}$$

where B is the Boltzmann constant, T is the absolute temperature and μ is the viscosity of the solvent. [153]

The functional groups on the GO were probed using Fourier transform infrared spectroscopy (FTIR). Samples for transmission measurements were prepared by taking aqueous dispersions of GO which were

drop cast onto a plastic weighing boat and left to dry overnight. The resulting free-standing thin film was characterized using a Bruker Tensor 27 with a scan resolution of 4 cm^{-1} and averaging over 32 scans.

Adsorption isotherms were generated by adding the fluorescent probe, Rh B to the IL phase and probing the fluorescence of the supernatant after centrifuging out the coated GO. To prepare samples for fluorescence spectroscopy, GO dispersions in DI water were diluted to different concentrations (0.1 mg/mL, 0.5 mg/mL and 2 mg/mL). For each GO concentration, a stock dispersion was created by first dissolving the desired amount of surfactant (TX-100 or Tween 20) into the GO aqueous solution by stirring using a magnetic stir bar for several minutes, and then adding the IL/Rh B dye to the GO/surfactant dispersion. The concentration of Rh B in IL was kept at 0.481 mM. After the Rh B/IL mixture was added to the GO/surfactant dispersion, it was bath sonicated (AnonKia, 360W) for 3 min which was long enough to convert the initially two-phase water/IL into a translucent dispersion and to break up any large agglomerates of GO. In case of pyrene, the same procedure as Rh B was applied, the concentration of pyrene was kept at 0.1 mM in surfactant (TX-100) and 0.025 mM in IL for both TX-100 /IL and P123/IL complex adsorption on GO. The surfactant to IL ratio was kept constant at 3, 4 and 1 for TX-100 and Tween 20, and P123, respectively. These ratios were chosen based on the least amount of surfactant that would create a transparent and stable dispersion. The stock dispersion was then diluted to different concentrations of surfactant using the same concentration of GO aqueous dispersion. The concentrations for TX-100 dispersions were varied from 0.016 to 1.33 wt.% whereas for Tween 20, they were varied from 0.022 to 1.76 wt.% (both based on total solution mass). For reference, the critical micelle concentration (cmc) of TX-100 and Tween 20 in the pure water are 0.015 and 0.00614 wt.%, respectively. [154] The resulting dispersions were mixed thoroughly and then kept at room temperature for 3 hours to allow for adsorption onto the GO surface. For the lowest concentration (0.1 mg/mL GO), the adsorption took longer to complete and the dispersion was left to reach an equilibrium overnight. Next, each concentration was centrifuged

using Eppendorf centrifuge 5424 at 1500 rpm for 10 min. This was enough for the dispersion to sediment. The supernatant was separated from the top of the vials and tested by fluorescence spectroscopy using a Variance Cary Eclipse. Emission spectra for Rh B were taken from 560 nm to 650 nm. The excitation wavelength was at 550 nm. For pyrene the emission spectra were taken from 350 nm to 600 nm and the excitation wavelength was at 337 nm. The excitation slit was set to 5 nm.

For each surfactant and GO concentration, a control concentration series was prepared to keep everything the same while excluding the GO. The control samples were tested using fluorescence spectroscopy where the concentration of the IL was plotted vs. emission intensity. The resulting linear relationship between fluorescence intensity (I_F) and concentration c at low concentrations can be described by:

$$I_F = 2.3\phi_F I_0(\lambda_E)\varepsilon(\lambda_E)lc \qquad \textit{Equation 3-4}$$

where ϕ_F is the fluorescence quantum yield, $I_0(\lambda_E)$ is the intensity of excitation light, $\varepsilon(\lambda_E)$ is the molar absorption coefficient ($L\ mol^{-1}cm^{-1}$), l is the optical path in sample (cm) and c is the concentration of fluorophore ($molL^{-1}$).[155]

This calibration curve was used later on to determine the unknown concentration of the supernatants after adsorption onto GO. The concentration of free Rh B in the supernatant of experimental groups was subtracted from the control to generate the adsorption curve. For each surfactant, the procedure was repeated three times and the average value was reported in the plots. The error bars represent the standard deviation (σ) of the three repeats.

Samples for AFM were prepared using the same method mentioned above for fluorescence spectroscopy. The only difference was that the dye was not included in the sample. Instead of centrifuging, the dispersion (0.1 mg/mL of GO) was spun coat onto freshly cleaved mica at 2000 rpm. The coated samples were dried and tested using non-contact, tapping mode AFM (MultiMode/Digital Nanoscope IIIa system,

Veeco Instruments). The tips used (Bruker, model TESPAW-V2) were silicon doped (radius of curvature less than 10 nm) with the resonant frequency of 320 kHz and spring constant of 42 N/m.

The AFM images were analyzed using Gwyddion software. Adsorbed layer thicknesses were determined by manually drawing line profiles (in the scan direction) over the entire area of the adsorbent. The thickness of the sample was determined using a custom Matlab code which fit both the flat mica background and step heights to parallel lines and determined the average thickness as the difference. This was only carried out in flat regions free of large agglomerates to generate histograms of the adsorbed layer. To measure the thickness of larger agglomerates of IL/surfactant mixture adsorbed to the GO at concentrations beyond the plateau region of the isotherms, a similar procedure was employed but the maximum height was chosen and reported in the histogram. The root mean square (S_q) roughness of the adsorbent surface was analyzed by studying the roughness of 10 points with an area of (0.7×0.7 μm) on the surface of the adsorbent using Gwyddion's statistical quantities.

X-ray diffraction of drop cast films of 0.5 mg/ml GO of different concentration of IL/TX-100 and TX-100 were performed using a Rigaku MiniFlex II from $2\theta = 3$ to 12 ° at 2 ° /min and scan width of 0.02 °. The d-spacing was calculated based on Bragg's law:

$$d = \frac{\lambda}{2\sin\theta}, \qquad \textit{Equation 3-5}$$

where λ is the wavelength of the incident light (Cu kα), θ is the incident angle, and d is the d-spacing between the two planes.

Optical microscopy was performed using Leica DM 2700 M. The samples of GO/IL mixture were simply spread over a glass slide using a spatula and was observed under the microscope at 10, 20 and 50X magnifications.

3.3 Results and Discussion

In the following, we attempt to elucidate the adsorption behavior and adsorbed layer structure of ternary mixtures of hydrophobic IL (EMImTFSI)/non-ionic surfactant (TX-100 and Tween 20)/water onto dispersed GO after it has been dried. Adsorption of this and similar IL/non-ionic surfactant systems are being increasingly used as a tool to assemble 2D material/IL nanocomposites for energy storage where the IL/surfactant helps to prevent the 2D material from restacking and enables bypassing the electrolyte (i.e., the IL) imbibition step as it is already part of the electrode assembly process.[106–108] To better understand the entire adsorption process, we first take a closer look at the sizes of the dispersed phases formed by the adsorbates in water. We then use two fluorescent labels with significantly different properties to follow the adsorption of both the IL and surfactant phases onto the GO at varying concentrations. After elucidating the adsorbed layer characteristics in dispersion, we attempt to assess the adsorbed layer morphology and thickness in dried films by AFM and XRD and compare the results to the adsorption isotherms, keeping in mind potential artifacts caused by drying.

Characterization of mixed micelles and graphene oxide dispersion:

As shown in Figure 3-1a, EMImTFSI is a hydrophobic and water-immiscible IL and clearly phase separates from water. The hydrophobicity of ILs is usually dictated by their anion type and the TFSI anion is only sparingly soluble in water.[156] The leftmost image of Figure 3-1b shows water/EMImTFSI/TX-100 mixture after shaking with TX-100 to IL mass ratio of less than 3. This creates a cloudy emulsion that quickly phase separates. Adding increasing amounts of surfactant (TX-100) to the water/IL mixture reduces the turbidity of the solution. When a 3:1 surfactant to IL ratio is reached, the mixture becomes optically transparent and remains so for several months (Figure 3-1b, rightmost image). This is an indication of the formation of stable micellar-like structures that are too small to scatter visible light.

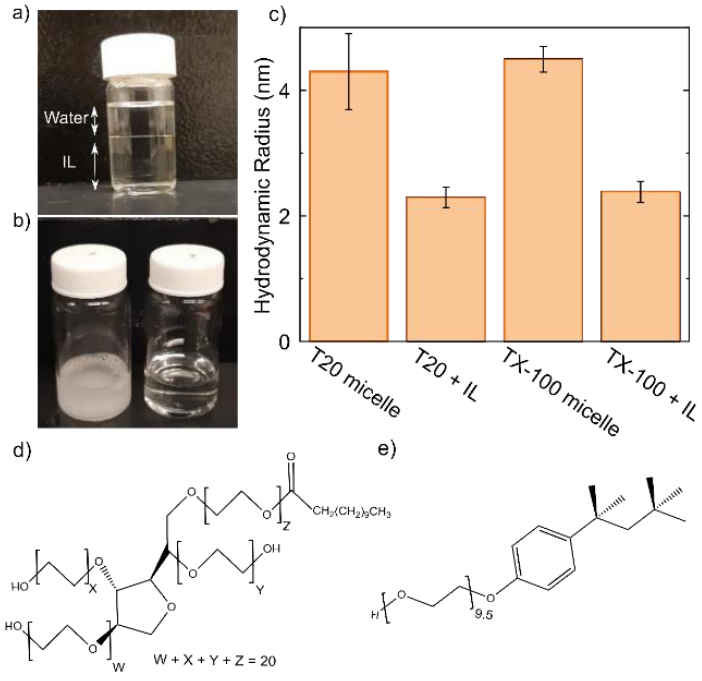

Figure 3-1: Colloidal particle analysis, a) EMIM TFSI in water; b) left vial: Aqueous TX-100 solution with EMIM TFSI (Surfactant to IL less than 3), right vial: Aqueous TX-100 solution with EMIM TFSI with surfactant to IL of 3, c) Particle size analysis using DLS, d) Tween 20 chemical structure, e) TX-100 chemical structure

DLS was used to measure the hydrodynamic radius of these micellar-like structures as shown in Figure 3-1c for both TX-100 and Tween 20 with and without the presence of IL. In the absence of IL, the hydrodynamic radius of TX-100 micelles in water was 4.5 ± 0.2 nm in accordance with the previously reported values ranging from 3.2[157–159] to 4.5 nm [160] due to polydispersity of TX-100 surfactant.[161]

A measured micellar size for Tween 20 was 4.3 ± 0.6 nm, with a larger standard deviation compared to TX-100, portraying more diversity of the micellar shape and size, which is in line with the reported 3.6 ± 0.6 nm micellar size by Elka et al.[162] In the presence of IL, the micellar-like structures in the water/surfactant mixture can change as a result of different IL/surfactant interactions giving rise to formation of different shapes and sizes.[135,137,138]

The IL/surfactant interactions within the micellar phase can cause close-packing and micellar shrinkage as observed by the addition of EMImTFSI to both Tween 20 and TX-100 where it shrunk their micellar diameter by 47% and 48 %, respectively (Figure 3-1c). This behavior has been previously reported for TX-100 micelles in contact with 1-butyl-3-methylimidazolium tetrafluoroborate, 1-butyl-3-methylimidazolium hexafluoroborate and 1-butyl-3-methylimidazolium hexafluorophosphate,[137] as well as for Tween 20 in contact with 1-pentyl-3-methylimidazolium tetrafluoroborate.[163] The chemical structure of TX-100 and Tween 20 are shown in Figure 3-1d and e respectively. A schematic of possible IL/surfactant interactions is presented in (Figure 3-2). These are summarized into three main interactions: i) The hydrophobic interactions between the alkyl chain of imidazolium cation and the hydrophobic chain of TX-100; ii) Hydrogen bond between C_2-H of imidazolium cation and the oxygen atom of PEG chain of TX-100 and between the fluorine of hexafluorophosphate and tetrafluoroborate and the hydroxyl hydrogen of TX-100; and iii) Dipole-dipole interaction between the aromatic ring of TX-100 and the imidazolium ring of IL.[137,140,141] We postulate that similar interactions within the micellar phase can be the cause of micellar shrinkage in our system.

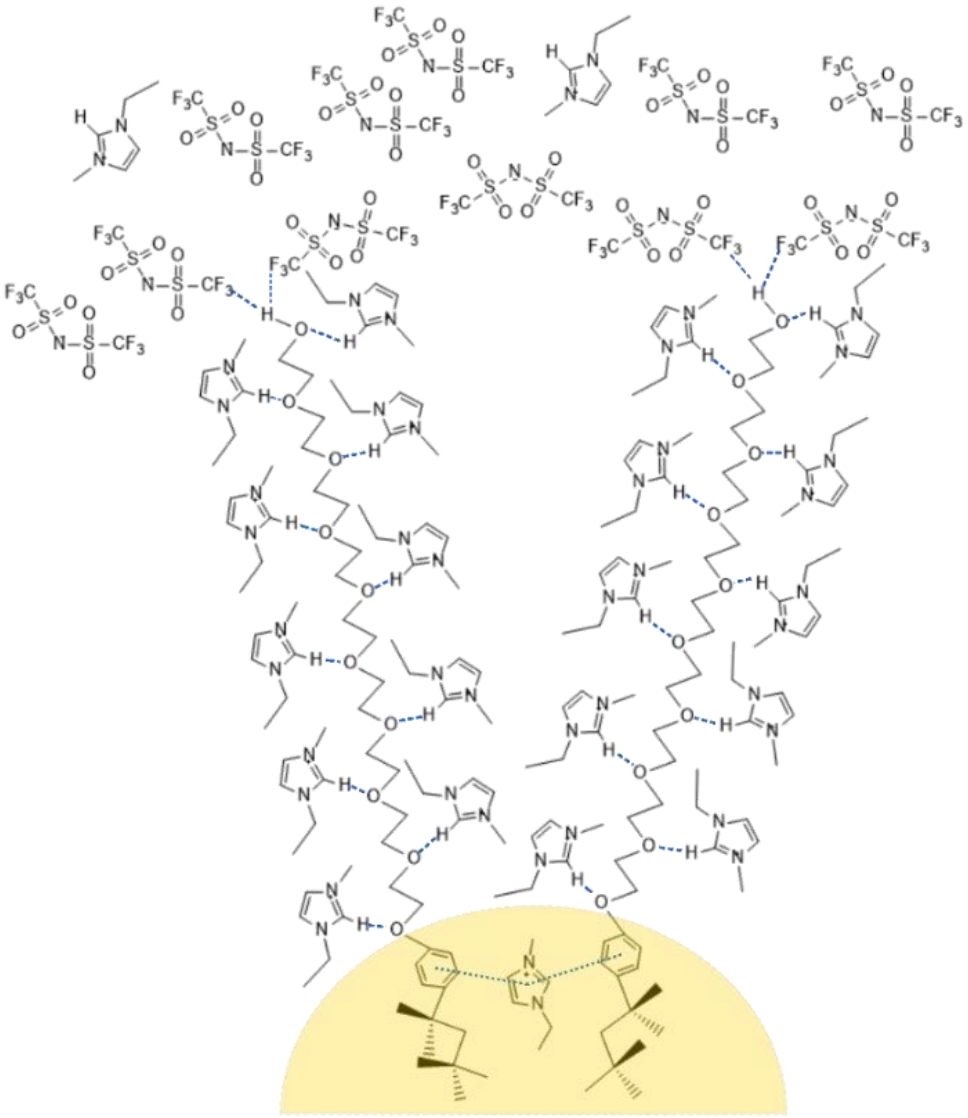

Figure 3-2: Possible interactions between EMImTFSI and TX-100 in mixed micelle (dashed blue line represent hydrogen bonding between C2-H of imidazolium and oxygen atom of PEG group in TX-100, and between F atom in TFSI and hydrogen hydroxyl of TX-100, dotted blue line represent dipole-dipole interaction between aromatic ring of TX-100 and IL

Characterization of GO:

GO is used as the adsorbent in this study. The FTIR spectra of as-synthesized GO is provided in Figure 3-3. In this spectrum, the C-H bending vibration of alkynes can be found as a broad band in 662 cm^{-1} (700 – 610 cm^{-1} regions, grey band), the first overtone of which appears as a weak broad band in 1372 cm^{-1}

(1370-1220 cm^{-1}, purple band). The O-H stretching of free hydroxyl group of alcohol and phenol absorb strongly in the 3592 cm^{-1} (3700-3584 cm^{-1}, blue band). The band at lower frequencies of 3380 cm^{-1} (3550-3200 cm^{-1}, green band) is the result of O-H stretching vibration of water molecules. The C-O stretching vibrations in alcohol and phenol are affiliated with absorption at 1250 cm^{-1} (1260-1000 cm^{-1}, peach orange band). The C=C stretching of vinyl ethers occurs in the 1629 cm^{-1} (1660-1610 cm^{-1}, yellow band) and finally, the carbonyl group (C=O) of aldehyde appears at around 1730 cm^{-1} (1740-1720 cm^{-1}, orange band).[164]

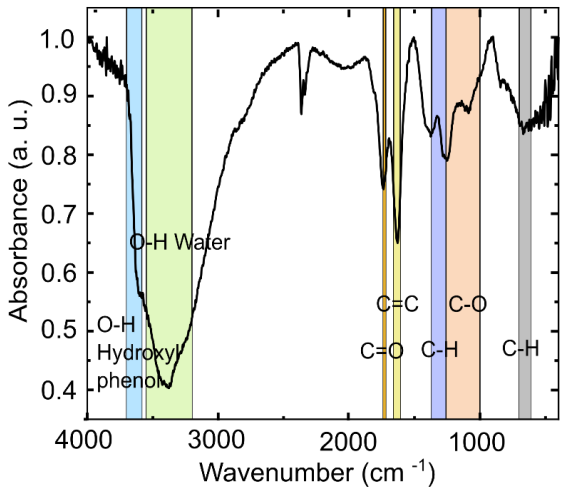

Figure 3-3: FTIR spectra of GO. Each functional group is color coded: grey for C-H first overtone of bending vibration of alkyls, peach orange for C-O stretching vibration in alcohol and phenol, purple for C-H bending vibration of alkyls, yellow for stretching vibration of C=C bond from ether, C=O carbonyl group of aldehyde, green for O-H stretching vibration of water molecules, and blue for O-H stretching vibration of hydroxyl group of alcohol and phenyl.

The thickness and lateral dimension of the synthesized GO that was used for the adsorption test were analyzed using AFM. The synthesized GO sheets' lateral dimensions follow a normal distribution with a median of 0.74 µm (Figure 3-4). The thickness distribution is discussed below alongside the adsorption results.

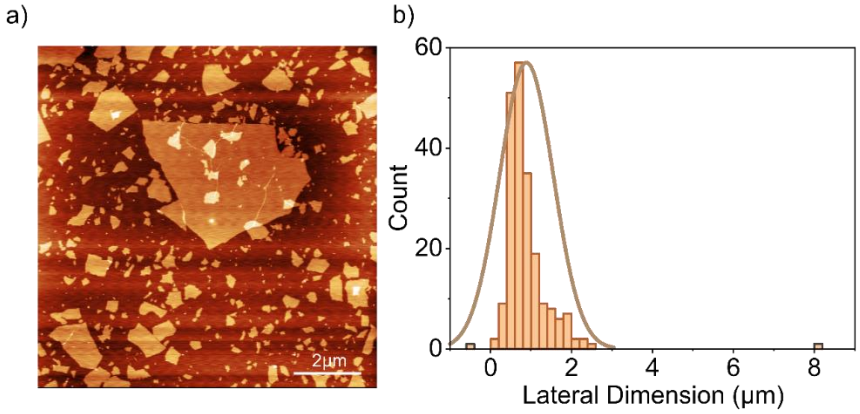

Figure 3-4: The lateral dimension of GO, a) tapping mode AFM image of GO particles, b) Histogram of lateral dimension analysis (N=102)

Interaction of IL and GO:

Before analyzing the adsorption of these mixed micelles onto the GO surface, interactions of IL and GO without any surfactant is studied (the adsorption of IL alone on GO could not be studied due the low solubility of EMImTFSI in water). Emulsifying the IL by ultrasonication in a GO dispersion resulted in the formation of a viscous gel as shown in Figure 3-5 and Figure 3-6. With increasing the concentration of GO, the color of the mixture changes into light brown and the viscosity of the mixture increases. At 90% IL, for 5 mg/ml of GO, a thick gel structure forms that flows very slowly under gravity upon tilting the vial as illustrated in Figure 3-5.

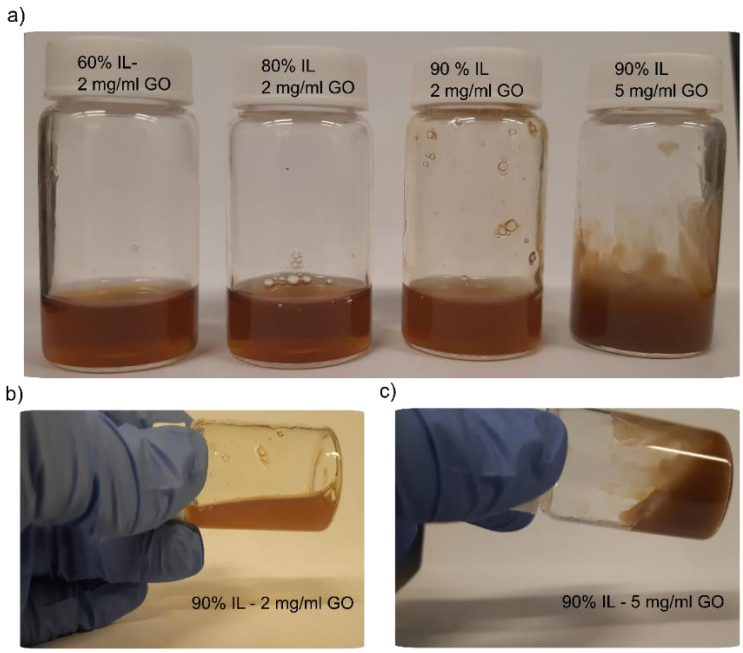

Figure 3-5: Interaction of EMImTFSI with GO (no surfactant) at different concentration of IL and GO; a) GO/EMImTFSI mixture with increasing the concentration of IL (60%, 80% and 90 % IL), b) 90% IL (2 mg/ml GO), c) 90% IL (5 mg/ml GO)

This demonstrates that a 3D network is formed between the GO and IL. To determine the structure of this gel, we performed optical microscopy on the samples with 60%, 80% and 90% IL (Figure 3-6). Small globular-like structure can be observed throughout the dispersion which grow to larger spherical shapes with increasing IL concentration at constant GO concentration. This demonstrates that a two-phase system remains and that the IL has been emulsified and becomes trapped within a network of GO. When increasing the concertation of GO, while keeping the IL to GO ratio the same (90 %IL), the size of the spheres becomes smaller which is likely due to an increase in the network density of the GO in the initial dispersion.

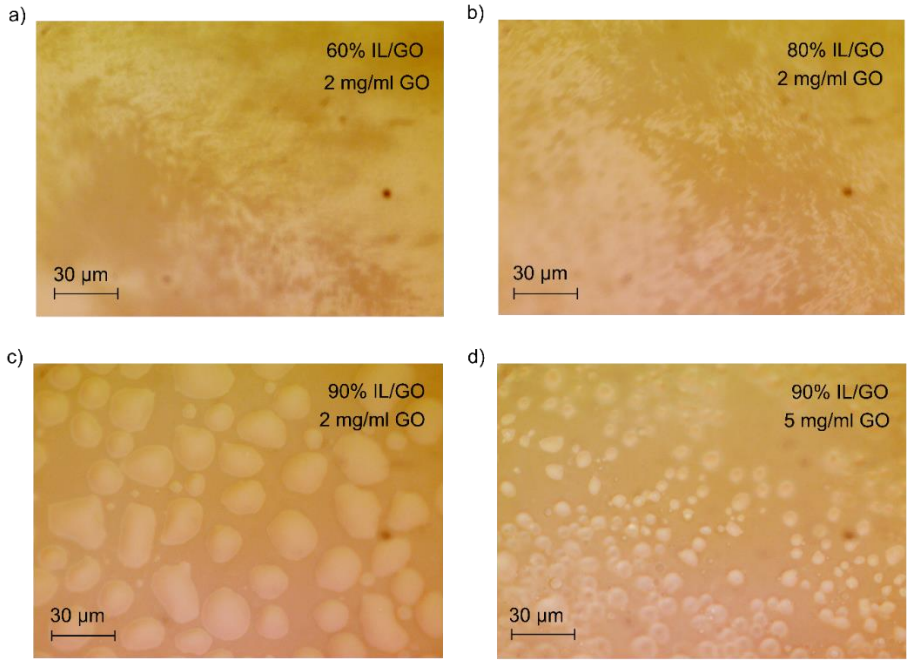

Figure 3-6: Optical microscopy image of GO/EMImTFSI (no surfactant) at different concentration of IL and GO; a) 60% IL, 2 mg/ml GO; b) 80% IL, 2 mg/ml GO; c) 90% IL, 2 mg/ml GO; d) 90% IL, 5 mg/ml GO.

Adsorption of IL on GO:

To study the amount of IL adsorbed to the GO surface, we used Rh B dye as a fluorescent marker. Rh B was chosen since it has a strong tendency to interact with EMImTFSI phase. Before getting into the details of the adsorption study, a more detailed study of the interaction of Rh B with GO, TX-100 and Tween 20 is provided in (Figure 3-7).

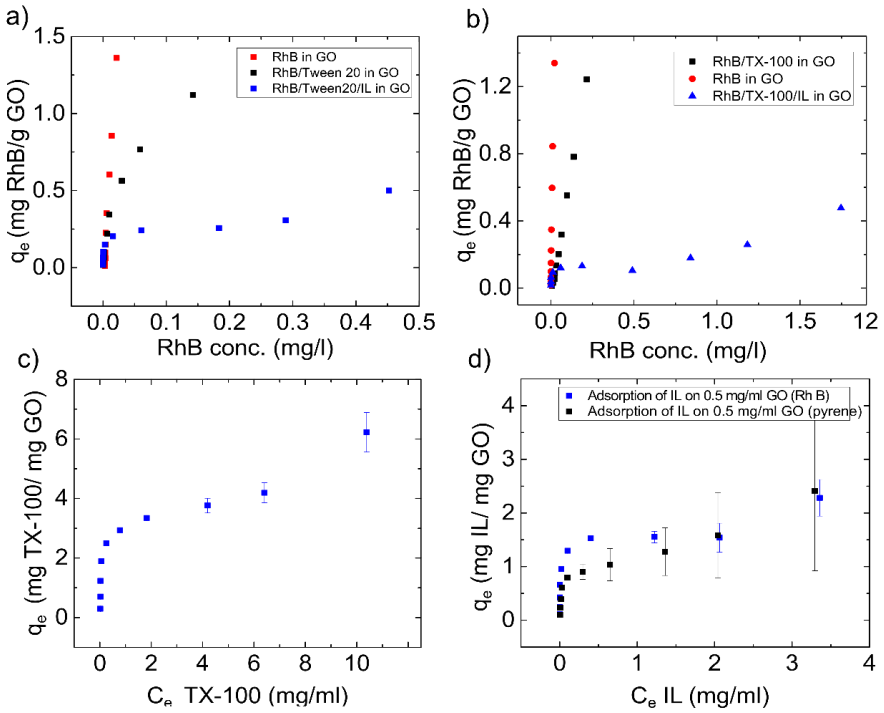

Figure 3-7: Interaction of Rh B and Pyrene with GO/TX-100 and EMImTFSI a) Interaction of Rh B with GO alone, GO and T-20 and GO/T-20 and EMImTFSI, b) Interaction of Rh B with GO alone, GO and TX-100 and GO/TX-100 and EMImTFSI, c) Adsorption isotherm of TX-100 on GO using Pyrene, d) Comparison of adsorption isotherm of EMImTFSI/TX-100 on GO using Pyrene and Rh B (Pyrene and Rh B are dissolved in IL phase)

When Rh B is first dissolved in water (without partitioning into the IL phase), and exposed to GO, it adsorbs strongly to GO as shown in Figure 3-7a and b. When TX-100 or Tween 20 is present in the solution, the Rh B adsorption is weakened but still remains strong. However, when the Rh B is first dissolved in the EMImTFSI, the adsorption isotherm takes a completely different path and follows the stepwise adsorption (Figure 3-7a and b). While we believe that Rh B does not significantly adsorb to the GO when complexed with the IL, we cannot rule out the possibility of some enhanced apparent adsorption via Rh B that might dissolve into the water phase and adsorb directly to the GO. For this reason, we also confirmed our results using pyrene which is insoluble in water and strongly complexes with the non-ionic surfactant. In Figure

3-7c, the adsorption isotherm of TX-100 alone on GO using pyrene is shown. It demonstrates a similar behavior to the TX-100/IL complex adsorption shown using Rh B. Since pyrene is soluble in both the IL and TX-100, it can also be used to label the complex and can be used to probe the TX-100/IL complex adsorption. In Figure 3-7d, we compare adsorption isotherms for the IL using this system vs. using Rh B as a probe (that is only soluble in the IL phase) and obtain similar results but with a reduced Q_{max} for pyrene. This could be due to some non-complexed Rh B adsorbing to the GO in addition to the IL/TX-100 complex as a result of its water solubility.

Figure 3-8a compares the fluorescence intensity of the Rh B in water (left vial in the inset) and the Rh B in equilibrated water /IL system (right vial in the inset). As shown in Figure 3-8a, Rh B strongly partitions into the IL phase in the immiscible water/IL system. Therefore, we assume that the mixed micelle of IL/TX-100/water is labeled with Rh B. Next, we compared the intensity of Rh B fluorescence emission in the mixed micelles (IL/TX-100/water) with and without GO. The inset of Figure 3-8b on the left shows a mixture of IL/TX-100/water prepared with an IL concentration of 0.9 mg/mL as control and, on the right, a beaker containing the same composition of IL/TX-100 in water but also containing 0.1 mg/mL of GO. The same concentration of Rh B is present in both samples. As shown in Figure 3-8b, the control mixed micelle (left beaker, blue line) has a higher emission intensity compared to the mixed micelle with GO as a result of adsorption of dye-labeled IL onto the GO and the quenching properties of GO.[165] GO can quench fluorophores which lowers their quantum yield if the fluorophore is located within a few nanometers of the GO surface. The Rh B fluorescent quenching mechanism by GO was attributed to static quenching in which the fluorophore forms a non-fluorescent complex with the quencher[165] and provides a non-radiative decay route for the relaxation of the excited electrons.[166] Surface adsorption and Pi-Pi stacking of the fluorophore and GO causes a redshift in the emission spectrum of the quenched fluorophore[167] that is an indication of a decreased energy gap between the ground state and the excited electronic state.

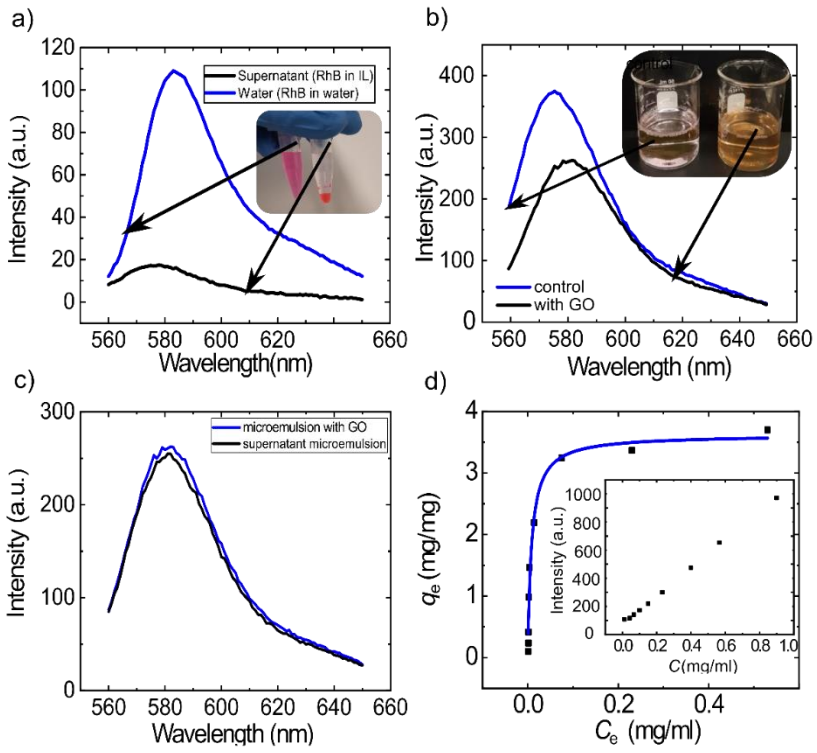

Figure 3-8: Adsorption analysis using fluorescence. a) The fluorescence intensity of Rh B in water compared to when we have Rh B in IL in equilibrium with water (inset: leftmost figure is a picture of Rh B labeled IL in water illustrating preference of Rh B for EMImTFSI phase of a water/EMImTFSI mixture (no surfactant) and rightmost figure is Rh B in water); b) Fluorescence spectra demonstrating fluorescence quenching of GO (inset: left beaker contains EMImTFSI/TX-100 in water with Rh B, right beaker contains EMImTFSI/TX-100 in water with Rh B and GO); c) Fluorescence spectra of dispersion and supernatant before and after centrifugation, respectively; d) Adsorption isotherm for TX-100/IL using 0.1 mg/ml GO. The solid line is the Langmuir fit (the inset shows the linear increase in fluorescence with no GO which was used as a calibration curve).

To further confirm the adsorption of dye-labeled IL onto the GO, we separated the GO from the solution by centrifugation. As shown in Figure 3-8c, both the fluorescence intensity of the supernatant alone and the supernatant with dispersed GO was nearly identical. Both spectra in Figure 3-8c also showed the same reduced emission intensity which we attribute to the depletion of dye-labelled IL from the bulk solution due to adsorption. To ensure that the mixed micelle distribution in the solution was not significantly impacted by centrifugation, we compared the fluorescence emission of a mixed micelle dispersion (no GO)

before and after centrifuging. The emission intensity is unchanged and thus we conclude that any decrease in fluorescence intensity is caused only by adsorption of the dye-labeled IL and the quenching of Rh B by the GO (results not shown).

From this data, adsorption isotherms were generated for dye-labelled IL for the different surfactants. An example for TX-100 mixtures exposed to 0.1 mg/mL GO is shown in Figure 3-8d. The adsorbed amount (q_e) follows a Langmuir isotherm which can be described by:

$$q_e = {Q_{max} K_L C_e}/{1 + K_L C_e}, \qquad \textit{Equation 3-6}$$

where C_e is the equilibrium concentration of IL (mg adsorbate/mL of dispersion), K_L (ml adsorbate/mg GO) is a measure of the affinity of the adsorbate to the adsorbent and Q_{max} (g adsorbate/g GO) is the maximum adsorbed amount. As shown in Figure 3-8d, the isotherm rises steeply at low C_e and reaches Q_{max} ~ 0.1 mg IL/mL where the adsorption plateaus. The inset of Figure 3-8d shows the calibration curve used to map the fluorescence intensity to the concentration of dye-labelled IL in the absence of the GO. Using a similar approach, we analyzed the adsorption of TX-100 on GO in the absence of IL. Due to the lack of affinity between Rh B and TX-100, pyrene was used which is soluble in TX-100 and insoluble in water. Pyrene is expected to associate with the hydrophobic tail of the TX-100 more so than the hydrophilic hydrated GO surface. However, pyrene is not appropriate as a label for IL as it can interact with the TX-100 component of the complex.

In order to determine the impact of GO concentration on the adsorption isotherms, we carried out experiments at various GO concentrations in the range of 0.1 - 2 mg GO/ml as shown in Figure 3-9. Langmuir isotherm closely fit the adsorption data with R^2 values above 0.9 except for the 2 mg/mL GO concentrations. As shown in Table 3-1, the Langmuir constants are strongly influenced by the GO concentration. For both surfactants, K_L and Q_{max} values increase with decreasing GO concentration due to better GO dispersion, hydration, and as a result higher available surface area for interaction. At high GO

concentration, there are more interactions between adjacent GO in solution as the network of high aspect ratio, ultra-thin sheets mechanically percolates, which limits the available surface area for adsorption and causes a higher rate of desorption by the mechanical sweeping of sheets against each other. The lower Q_{max} at higher GO concentration suggests that these closely packed interacting GO particles do not effectively interact with IL/surfactant which reduces their extent of adsorption. By further decreasing the concentration of GO from 0.1 to 0.05 mg/mL (results not shown), the isotherm remained unchanged which implies the maximum adsorption happens at 0.1 mg/ml.

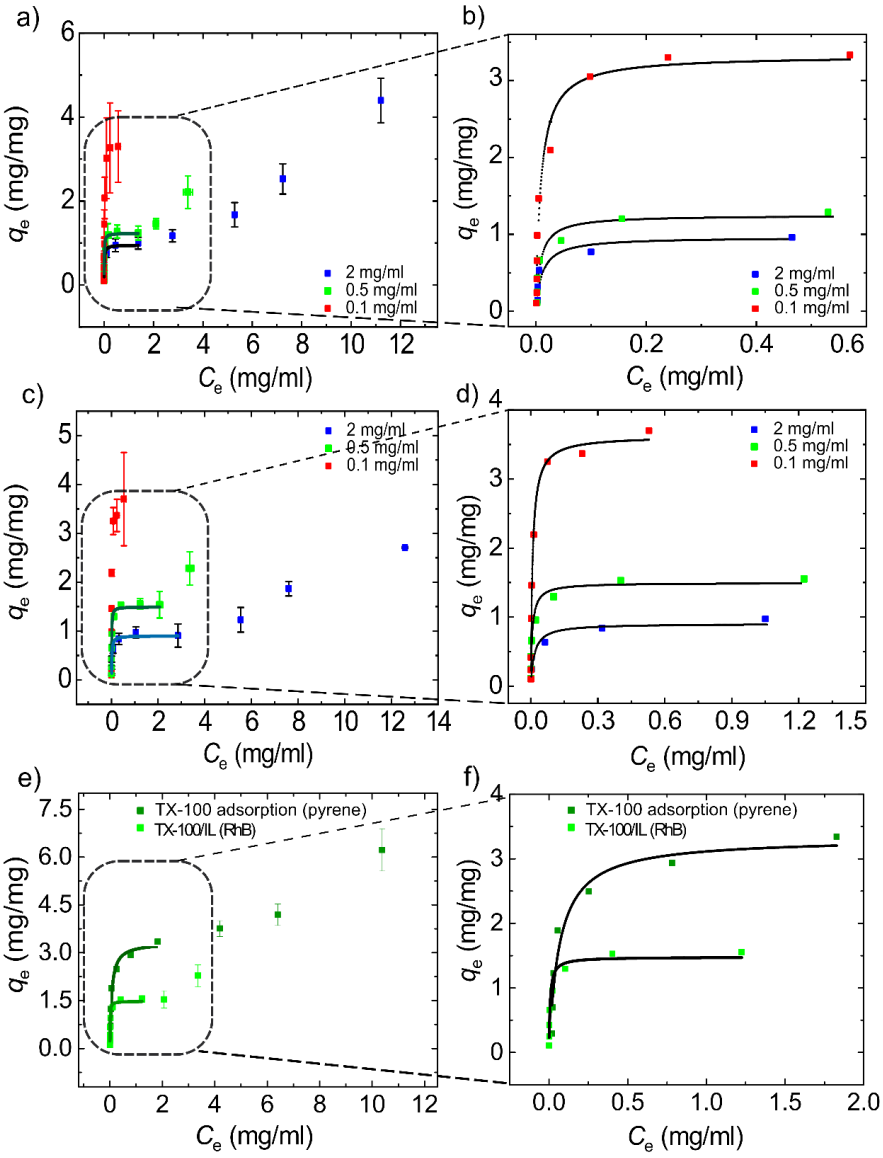

Figure 3-9: Adsorption isotherm and corresponding Langmuir fit for both Tween 20 and TX-100 mixed IL, solid lines represent the Langmuir fit for the corresponding concentration a) Adsorption isotherm of EMImTFSI/ Tween 20 mixed micelle on 0.1, 0.5 and 2 mg/ml GO, b) Langmuir fit for EMImTFSI/Tween 20 at 0.1, 0.5 and 2 mg/ml of GO c) Adsorption Isotherm for EMImTFSI/ TX-100 mixed micelle on 0.1, 0.5 and 2 mg/ml GO, d) Langmuir fit for EMImTFSI/TX-100 at 0.1, 0.5 and 2 mg/ml of GO, e) Adsorption isotherm for TX-100 on 0.5 mg/ml GO (pyrene as label) compared to the same concentration of TX-100 with IL (Rh B as a label), f) Langmuir fit for TX-100 and TX-100/IL on 0.5 mg/ml GO

While in all cases the isotherms show Langmuir-type adsorption at low C_e, at higher concentrations of GO (0.5 mg/mL and above) and higher C_e (> 1 mg/ml), a stepwise increase in the adsorbed amount can be seen (Figure 3-9a, c and e). This behavior is often attributed to the rearrangement of adsorbates on the absorbent surface enabling an increase in the packing density[168] and has been reported for adsorption of p-nitrophenol, [169] and naphthalene 2-sulfonic acid on graphite.[168] With more efficient packing, a second rise in the slope of the curve appears and at the point of maximum packing density, the second plateau point arises. Figure 3-9e and f compare the adsorption isotherm of TX-100 alone (using pyrene as label) and TX-100/IL mixed micelle at 0.5 mg/ml of GO. As it is apparent from the figure, both for TX-100/IL and TX-100 alone, a similar adsorption isotherm is observed, suggesting that the adsorption of IL follows that of TX-100 which implies that the non-surface-active IL adsorbs together with TX-100 in a complex form. Using the value of Q_{max} for both isotherms, TX-100 alone adsorbs around three times more than the IL in the mixed adsorbate (3.7 mg /mg GO for TX-100 vs. 1.77 mg/mg GO for IL). As the mass ratio of IL to TX-100 is also 1 to 3, this result confirms that the IL/TX-100 adsorbs as a complex with similar composition to the bulk mixed micelles. In addition, the first adsorption plateau for TX-100 alone happens at around the same concentration as IL adsorption (~0.4 mg/ml), further supporting the co-adsorption of IL and TX-100 which we refer to as mixed adsorbate. However, the K_L value is smaller for TX-100 ($K_L = 38 \pm 2$ ml/mg vs. 83 ± 67 ml/mg for the Rh B case), which may be due to the hydrophobicity of pyrene and its lack of affinity towards oxygen-containing functional groups on the GO.

Table 3-1: Calculation of the Langmuir parameters using a Langmuir fit

	Conc. of GO (mg/ml)	Q_{max} (mg adsorbate/mg GO)	K_L (ml/mg)	R^2
TX-100/IL	0.1	3.16 ± 0.64	179 ± 83.7	0.98
	0.5	1.72 ± 0.32	83 ± 67	0.95
	2	1.03 ± 0.14	66 ± 38	0.79
Tween 20/IL	0.1	3.01 ± 0.38	167 ± 81.2	0.97
	0.5	1.13 ± 0.15	102 ± 27.7	0.94
	2	0.79 ± 0.12	79 ± 56	0.70
TX-100	0.5	3.65 ± 0.39	34 ± 27.6	0.93

In an attempt to visualize the adsorbed structure, we carried out *ex situ* AFM on dried films prepared from the various dispersions discussed above. *In situ* liquid-cell AFM was attempted but the system was very challenging to work with and definitive results could not be obtained. In these *ex situ* AFM studies, since the concentration of adsorbate will increase continuously as the thin film dries onto the mica substrate, this could potentially lead to a higher equilibrium concentration causing more surfactant/IL to adsorb or deposit onto the GO during the few second evaporation process. To mitigate this source of error, in the discussion below, using our adsorption equilibrium data, we provide an estimate of how much bulk material could possibly add to the film and potentially skew our thickness analysis. Using the adsorption isotherms as a guide, dispersions at various steps of the adsorption isotherm for the 0.5 mg/mL GO concentration case were spun coat onto mica and imaged after drying. Figure 3-10a shows the AFM images of bare GO with an atomically flat surface and a median thickness of 1.11 nm, this value is within the reported range (0.7-1.1) for single-layer GO thickness.[66,84,170] The thickness profile is provided in the inset image of Figure 3-10a ii, showing the low roughness value of S_q = 114 pm (the roughness and thickness values are compared

in Figure 3-13a and b, respectively). Figure 3-10b shows an AFM image of GO obtained from dispersion with C_e = 0.005 mg IL/mL (see Figure 3-9d for corresponding isotherm) which corresponds to the initial rise in the adsorption isotherm and far from the plateau. A clear textured surface is visible in some regions and the height profile illustrates a rougher structure (S_q = 768 pm) than the bare GO surface. The median thickness slightly increased to 1.12 nm while the height distribution broadened. Due to the strong adsorption at this concentration, we expect most of the surfactant/IL complex to be adsorbed to the GO but with a small amount remaining in solution. This remaining material dispersed in the bulk would also dry onto the mica and GO. To have an estimate of how much this remaining materials might affect our final result, we estimate the percentage of unabsorbed materials from the adsorption isotherm which is the value of C_e divided by C_1 (concentration of IL in the original dispersion before adsorption occurs) which equals 1.5 % and will not contribute significantly to the measured height profiles.

Figure 3-10c shows the surface morphology of GO sheets at the first plateau region in the adsorption isotherm at Figure 3-9d, obtained from a dispersion with C_e = 0.4 mg IL/mL. In this region, the GO surface exhibits a textured morphology, evidenced by the line profile (inset of Figure 3-10c ii). The line profile shows a relatively uniform but patchy morphology varying in thickness from 2 to 3 nm with S_q = 735 pm. Analysis of the line profiles reveals that the thickness distribution has shifted to higher values and the maximum thickness of the GO + adsorbed layer has a median value of 2.5 ± 1.29 nm as illustrated in the histogram of Figure 3-10c. Using the same analysis as above, according to the adsorption isotherm, 36% of the IL remains in the bulk dispersion at this concentration which represents the maximum uncertainty in our measurements.

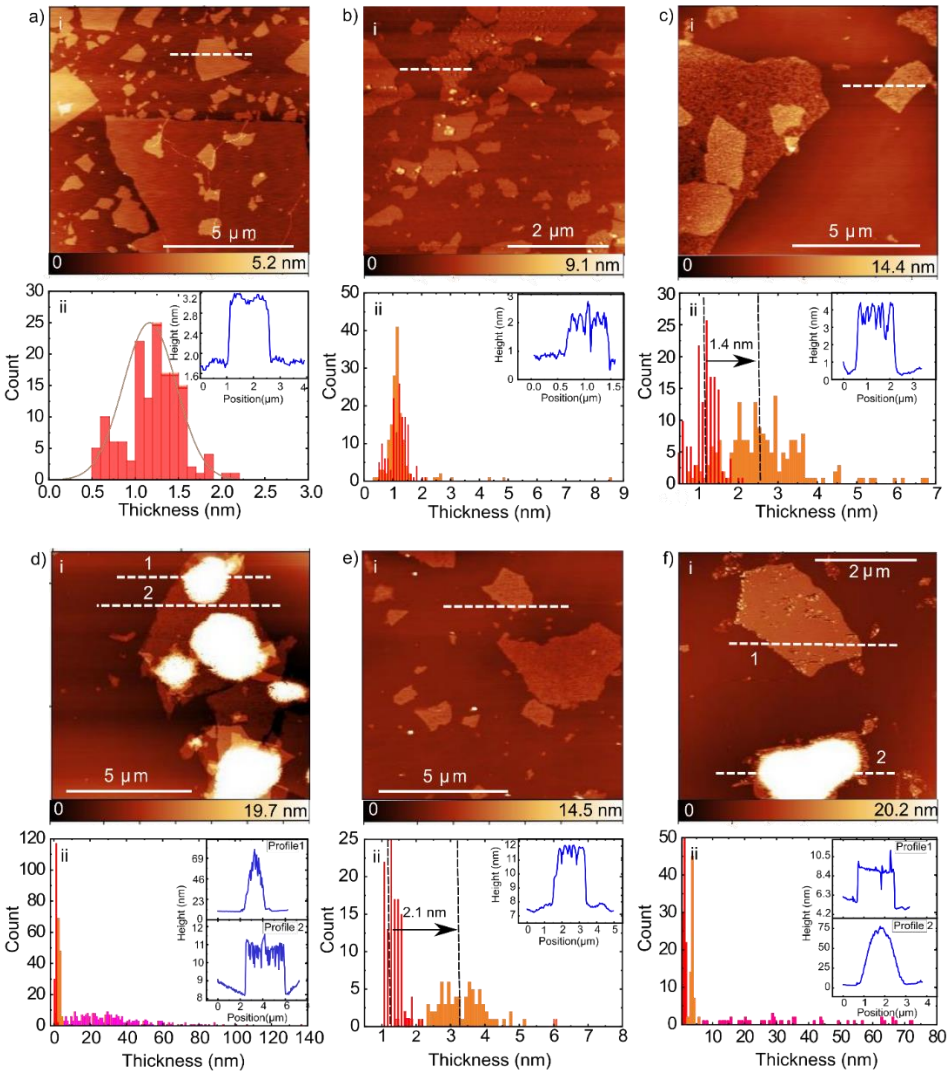

Figure 3-10: AFM analysis and thickness distribution of different adsorbate on 0.5 mg/ml GO, red represent the GO population, orange represents the monolayer adsorbate and magenta represent the agglomerated adsorbate, the insets in (ii) represent the line profiles in (i), a) i. AFM image of bare GO, ii. Thickness analysis of bare GO (N =149), b) i. AFM image of adsorption of 0.11 wt.% TX-100 (TX-100/IL) on GO, ii) thickness analysis of 0.11 wt.% TX-100 (TX-100/IL) adsorption (N =151), c) i. AFM image of adsorption of 0.34 wt.% TX-100 (TX-100/IL) on GO, ii. Thickness analysis of 0.34 wt.% TX-100 (TX-100/IL) adsorption (N=188), d) i. AFM image of adsorption of 1.33 wt.% TX-100 (TX-100/IL) on GO, ii. Thickness analysis of 1.33 wt.% TX-100 (TX-100/IL) adsorption (N = 660), e) i. AFM image of adsorption of 0.34 wt.% TX-100 on GO, ii. Thickness analysis of 0.34 wt.% TX-100 adsorption (N=79), f) i. AFM image of adsorption of 1.33 wt.% TX-100 on GO, f) ii. Thickness analysis of 1.33 wt.% TX-100 adsorption (N=120)

AFM images of the GO surface sampled from regions beyond the first plateau, corresponding to C_e = 3.35 mg IL/ml (on Figure 3-9d), show two distinct regions. First, uniform but textured regions similar to the adsorbed layer at the first plateau region (Figure 3-10c) with a lower roughness of S_q = 347 pm. Second, regions at the center of the sheets with a thicker adsorbed layer appear as spherical caps spanning several microns and a maximum height of about 25 nm (Figure 3-10d). The percentage of unabsorbed materials for this concentration is now much higher and contributes significantly to the uncertainty in the AFM measurement as, from the adsorption isotherm, around 70% of the IL remains in the bulk and could add to the adsorbed layer thickness during drying of the thin film formed during spin coating.

To differentiate between the surfactant alone and the mixed phase, we performed the same AFM analysis on neat TX-100 (no IL) as adsorbate. Similar behavior is observed when the surfactant alone is adsorbed on the GO surface. Figure 3-10e and f show AFM images of the GO after exposure to TX-100 with the same concentration as in the previous two cases with IL (C_e = 0.78 mg TX-100/mL and C_e = 10.38 mg TX-100/mL on Figure 3-9f). At the lower TX-100 concentration, a median thickness of 3.2 ± 0.75 nm is observed (Figure 3-10e) with a narrower distribution compared to the case with IL (σ = 1.29 nm). The narrower distribution is likely a result of having only one type of adsorbate. Nevertheless, the behavior is similar to what was observed for TX-100/IL mixture. At the highest TX-100 concentration (Figure 3-10f) two distinct regions of adsorbed layers were observed similar to the TX-100/IL mixed system. One exhibits a uniform coverage while the other appears as agglomerated masses of adsorbate with a thin spherical cap. As inferred from analysis of the AFM images and the corresponding height profiles (Figure 3-10e and f), the uniform film coverage of the higher concentration of TX-100 is smoother (455 pm compared to 615 pm for the high and low concentration cases, respectively) and thus likely denser compared to the lower concentration case which can indicate that the maximum packing density has not been met for the TX-100 at the lower concentration.

The same AFM analysis was also performed for the higher GO concentration (2 mg IL/ml) exposed to TX-100/IL mixture at 1.67 wt.% TX-100. As shown in (Figure 3-11) it follows similar behavior.

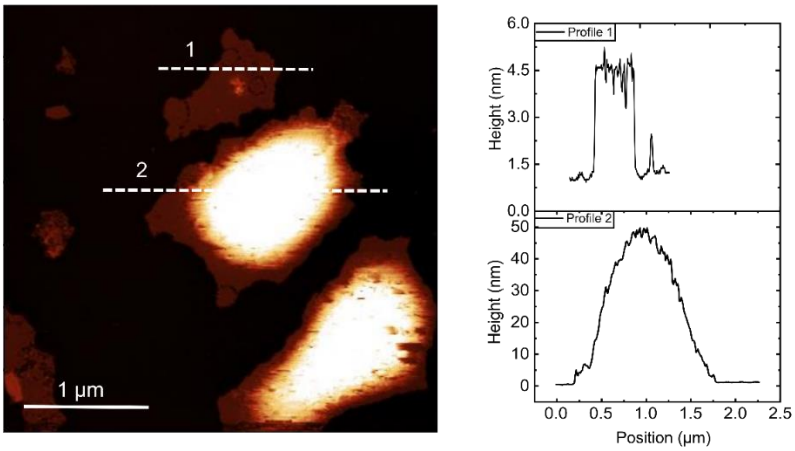

Figure 3-11: AFM analysis of adsorption of 1.67 wt.% TX-100/IL on 2 mg/ml GO

Adsorption of Tween 20/IL mixture on 0.5 mg/ml GO was also analyzed using AFM. Similar results were observed suggesting similar adsorption phenomena for Tween 20 and IL (Figure 3-12). Figure 3-12a shows an AFM image of adsorption of 0.13 wt. % (before the plateau in Figure 3-9a) of adsorbate (Tween 20/IL). From this image, it can be inferred that the particles (surfactant and IL) adsorb on the surface horizontally, as the thickness of the line profile shown (inset of Figure 3-12d) has not changed compared to the bare GO. In Figure 3-12d, thickness distribution of the adsorbent (0.13 wt.%) and bare GO is compared. According to this histogram, no significant increase can be observed in the thickness. Nevertheless, the AFM image in Figure 3-12a shows the appearance of adsorbate sporadically on GO surface. As the concentration of the adsorbate increases (0.46 wt.%, plateau region in Figure 3-9a), the thickness of the adsorbate film also increases. From Figure 3-12b, the surface of GO is covered with patches of adsorbate which increases the GO thickness by about 0.5 nm. Figure 3-12e can also detect that the

average thickness has barely increased. By increasing the adsorbate concentration up to 1.76 wt.%, a major change in GO thickness can be seen. Figure 3-12c shows the AFM image of the adsorbent, which depicts the appearance of thick layer of adsorbate adding up to 4 nm to the thickness of bare GO. The adsorption is uniform up to the plateau region of Figure 3-9a of Tween 20/IL (0.46 wt.%), However, at higher concentration, agglomeration of the adsorbate can be seen on the GO surface.

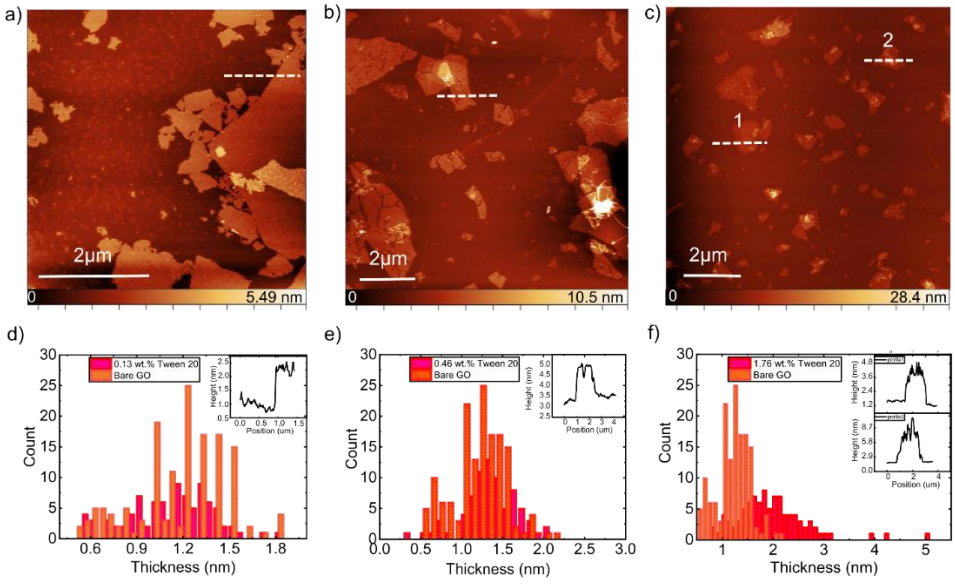

Figure 3-12: Thickness analysis of Tween20/IL mixed adsorbate on GO (0.5 mg/ml), a) AFM image of 0.13 wt.% Tween20/IL adsorbate on GO, b) AFM image of 0.46 wt.% Tween 20/IL adsorbate on GO, c) AFM image of 1.76 wt. % Tween 20/IL adsorbate on GO, d) Thickness analysis of 0.13 wt.% Tween 20/Il on GO (N = 91), e) Thickness analysis of 0.46 wt.% Tween 20/Il on GO (N= 78), f) Thickness analysis of 0.1.76 wt.% Tween 20/Il on GO (N = 95)

A summary of the area-averaged roughness data together with the adsorbent surface thicknesses for TX-100/IL is plotted for comparison in Figure 3-13. Neat GO has the lowest roughness value. The roughness value increases the most with almost no change in thickness value for C_e of 0.003 mg IL/ml, for TX-100/IL mixture, suggesting that the adsorbate lies flat and sparsely decorates the surface (Figure 3-13 b). As more adsorbate is added, the roughness is reduced while the thickness increased until it plateaus,

suggesting a maximum packing density is approached. For TX-100 alone (no IL), a similar trend is observed. Comparing the roughness between TX-100 and TX-100/IL mixture, at the lower concentration case (C_e = 0.4 mg IL/ml and C_e = 0.78 mg TX-100/ml), the roughness of TX-100 is lower, which can also be observed from Figure 3-10c and e. However, Sq for the TX-100/IL is lower than the neat TX-100 case at the higher concentration (C_e of 3.35 mg IL/ml), which can be explained due to local asperities/cavities in the surface of adsorbed TX-100. From the AFM images (see Figure 3-10f), it is clear that, locally, the surface of TX-100 adsorbed on GO is smoother. Figure 3-13c and d illustrate these concepts better. As illustrated in Figure 3-13c, just like how the micelle with IL has a smaller diameter, the thickness of the adsorbed layer with IL is also smaller and rougher than TX-100 alone. The effect of adsorbate concentration on the roughness and thickness is illustrated in Figure 3-13d, where increasing the adsorbate concentration, leads to their vertical alignment and close-packing which increases the thickness and reduces the roughness. By observing the thickness distribution, monolayer adsorption is our first speculation. However, the thickness measured by AFM is thinner than what we would expect based on the size of TX-100. – It should be noted that additional accumulation of IL/surfactant complex resulting from sample preparation (spin coating and drying) would act to increase this thickness, not reduce it. According to Robson and Dennis[171], the arrangement of the PEO chains in TX-100 micelle is around 3.4 nm if fully extended (zigzag) and 1.7 nm if contracted or in meander form. The contracted model may best represent our dry AFM samples, which for neat TX-100/GO measure at maximum 3.72 nm in total thickness. Since the GO itself should take up ~0.7 nm of this thickness (we measure 1.1 nm on average – likely due to adsorbed water but it is known that dry GO typically yields inter sheet spacing closer to 0.7 nm when observed by X-ray diffraction. This would lead to an adsorbed layer thickness on each side of the GO at maximum of ~3/2 = 1.5 nm and thus slightly below what we might expect from the meander conformation. On the other hand, for the mixed TX-100/IL case, the maximum measured thickness is $t_{\text{total, meas}}$ = 2.7 nm. Using the same analysis as above would only give about 1 nm of adsorbed layer thickness on either side of the GO meaning that the adsorbed

layer complex shrinks by ~41% compared to what we expect from molecular dimensions of TX-100 (1 nm vs. 1.7 nm). This follows the same trend observed for the mixed micelles measured by DLS for which the radius was also observed to shrink by 48 %. These discrepancies again point to the strong interactions and non-ideal mixing between the three components GO, IL and TX-100 or Tween 20. Furthermore, the large equilibrium constant suggests that the IL/surfactant complex physisorbed strongly to the GO which may shrink the apparent thickness of the adsorbed layer even more.

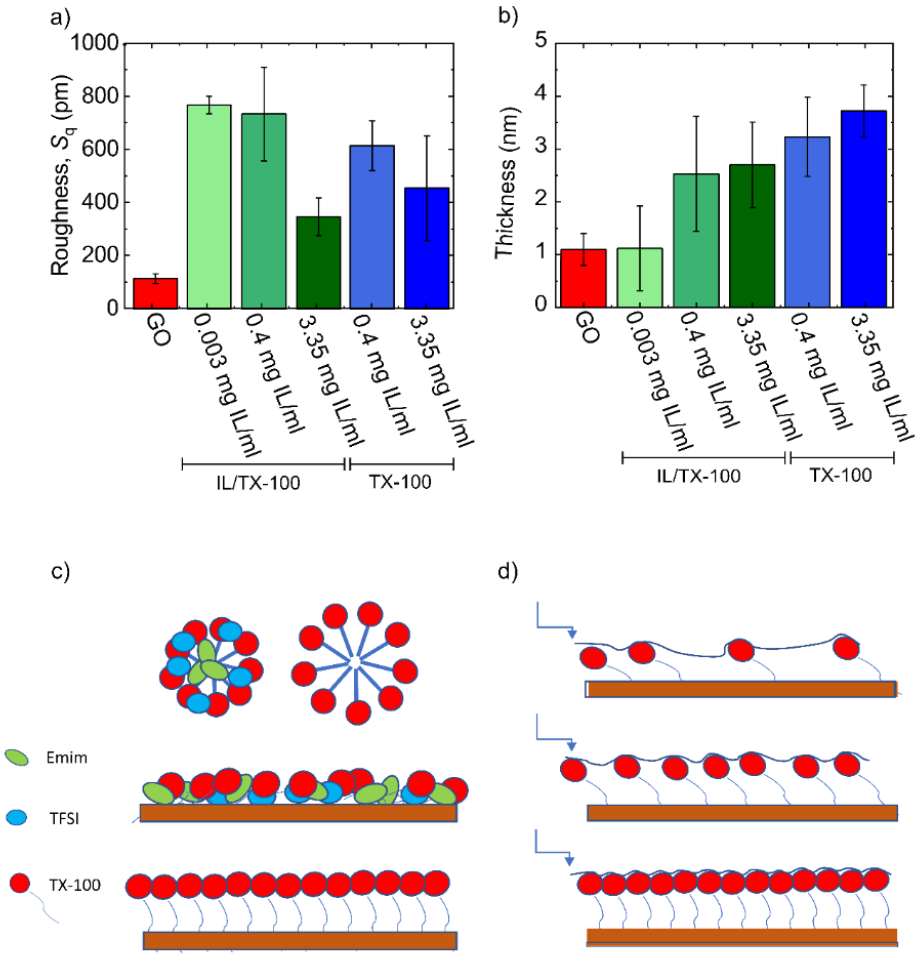

Figure 3-13: Analysis of surface thickness and roughness, a) roughness analysis only for monolayer region, b) thickness analysis for monolayer region only. For TX-100 alone, the value for C_e is the nominal values to facilitate the comparison with TX-100/IL mixture, c) schematics comparing IL/TX-100 mixed micelle and TX-100 micelle and their adsorption on GO, d) Illustrations of increase in thickness with a reduction in roughness as the concentration increase

The various trends observed by AFM were confirmed in thicker, cast films (taken on drop cast films of 0.5 mg/ml GO) by powder XRD as shown in Figure 3-14, which reveal the existence of two separate peaks for each concentration of IL and TX-100/IL suggesting that ordered domains remain after drying of a multi-layer composite. The associated d-spacings are shown in Table 3-2. Films dried with surfactant alone at the concentrations corresponding to those analyzed by AFM imaging, exhibit sharper and more intense peaks than those which also contain the IL. This is consistent with the smoother, more uniform films observed from AFM imaging. The more intense peak near $2\theta \sim 4°$ corresponds to a d-spacing of 2.1-2.2 nm. Since the measured d-spacing of our GO is calculated to be 0.82 nm, the corresponding adsorbed layer thickness is 1.3-1.4 nm for the two different concentrations and quite close to our values measured by AFM. However, the weaker peaks observed at $2\theta > 6°$ indicate that some regions possess less adsorbate in the dried film and, of course, XRD cannot probe the non-ordered domains of the film. From the data in Table 3-2, for samples with IL/TX-100 mixed adsorbate, the d-spacing is generally smaller than for the samples with TX-100 only. Although the difference is smaller than expected from what is shown by AFM resulting in an adsorbed layer thickness of 1.19 nm. Thus, XRD confirms the various trends observed.

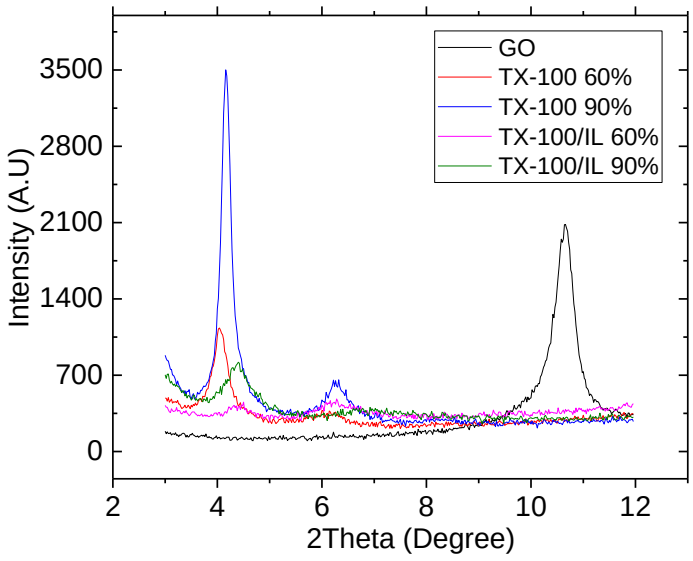

Figure 3-14: XRD analysis of the drop casted film of 0.5 mg/ml GO at different concentrations of TX-100 and TX-100/IL mixtures

Table 3-2: Calculation of the d-spacing based on recorded 2Theta of XRD

	Peak 1		Peak 2	
	2θ (degree)	d- spacing (nm)	2θ (degree)	d-spacing (nm)
GO	10.68	0.82	NA	NA
GO/TX-100 (90%) (3.35 mg IL/ml)	3.98	2.22	6.3	1.40
GO/TX-100 (60%) (0.4 mg IL/ml)	4.18	2.11	6.28	1.40
GO/TX-100/IL (60%) (0.4 mg IL/ml)	3.38	2.012	6.18	1.42
GO/TX-100/IL (90%) (3.35 mg IL/ml)	3.38	2.01	6.74	1.31

IL/surfactant self-assembly introduced by She et al.[106] has been repeatedly used for device fabrication.[107,108] However, the original assumption was based on the adsorption of microemulsion on the GO surface while the effect of adsorbent and adsorbate concentrations on the adsorbed layer was overlooked (Figure 3-15 a). The adsorption mechanisms revealed by our results are counter to previous assumptions[106] that droplet-like microemulsions of IL/surfactant adsorbed onto GO surfaces. A more accurate description is that strong interaction between IL and TX-100 or Tween 20 forms mixed-micelle complexes in solution. These complexes strongly adsorb onto the surface of GO but as a dense, uniformly distributed, mixed adsorbed layer (mixed adsorbate) which is much thinner than the size of the micelles in solution (Figure 3-15 b). The adsorbed layer thicknesses closely match the molecular dimensions of TX-100 and EMIM TFSI considering the non-ideal mixing and strong interaction of GO and adsorbate.

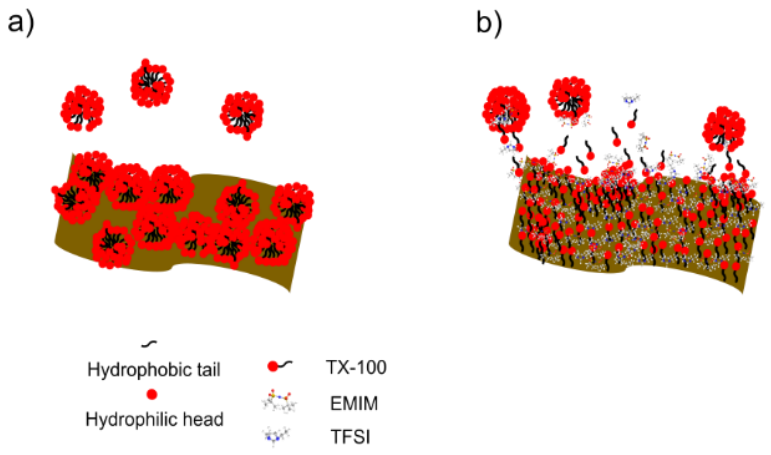

Figure 3-15: Graphical representation of She et al. hypothesis vs. our finding, a) She et al. model, b) our findings

Lastly, in this chapter, we would like to compare the adsorption of TX-100/IL and Tween 20/IL with that of P123/IL on 0.5 mg/ml GO using pyrene as a hydrophobic dye. This comparison was made since P123 was found to form a stable dispersion with IL at lower mass ratio of P123/IL = 1. As it was mentioned earlier in this chapter, pyrene interacts with IL as well as with hydrophobic groups of P123, TX-100 and

Tween 20 through hydrophobic interactions. Figure 3-16 compares the adsorption isotherm between these three systems.

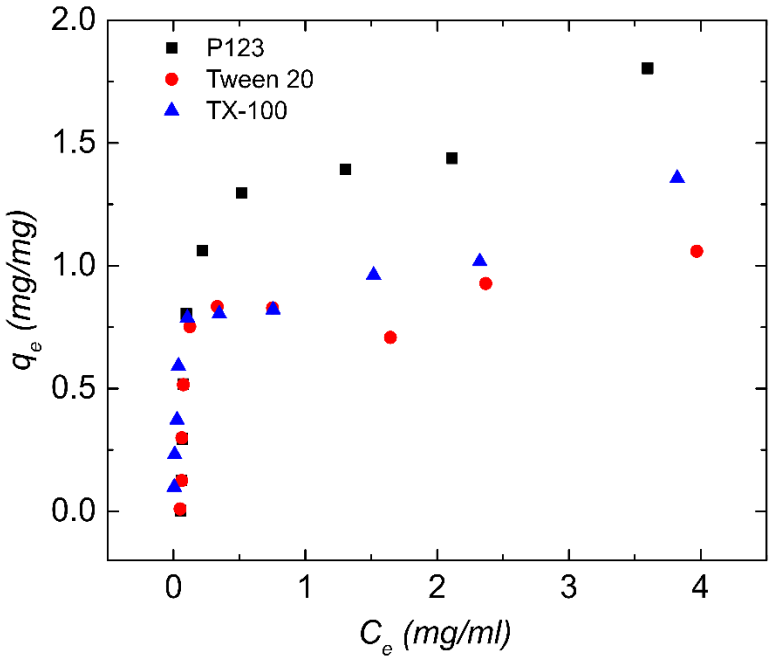

Figure 3-16: Adsorption of P123, Tween 20 and TX-100 complexed with IL on 0.5 mg/ml GO

As it can be seen using pyrene as a hydrophobic dye, the adsorption of TX-100/IL and Tween 20/IL has lowered compared to when using Rh B dye as fluorophore (Figure 3-9 a and c). Which again is due to the hydrophilic nature of Rh B dye. In addition, P123/IL complexed has considerably higher adsorption compared to Tween 20/IL and TX-100/IL complexes on GO surface. As this surfactant is also more effective in complexing with IL at lower concentrations, P123 can be a good replacement for Tween 20 as well. In the following chapter, we will explore the effect of these two surfactants on the double layer capacitance of the IL interfaced with carbonaceous electrode.

We hope that this study showcases how to selectively load significant quantities of non-surface active ILs like EMIM TFSI onto GO and, likely, related oxide-decorated surfaces. Even in the first plateau region the amount of IL contained within the adsorbed layer translates to upwards of 75 wt.% IL (considering only IL and GO) and thus a convenient way for immobilizing electrolytes for batteries and supercapacitors among other promising applications. However, the strong concentration dependence on the equilibrium adsorbed amount suggests that dynamic aspects might be important for creating dried, consolidated nanocomposites and should be investigated in future work.

3.4 Conclusions

In this work, we studied ternary mixtures of the water-immiscible ionic liquid EMIM TFSI in water and two common non-ionic surfactants (TX-100 and Tween 20). Both systems form visibly transparent dispersions containing mixed micelles which are ~48% smaller than the surfactant micelles alone suggesting a non-ideal mixing of the IL and surfactant phases. The adsorption isotherm was probed using Rhodamine B and pyrene as fluorescent probes for the ionic liquid and surfactant/IL phases respectively. At low equilibrium concentrations, Langmuirian behavior was observed while at high equilibrium concentrations, a second step in the adsorption isotherm begins to emerge indicative of multi-layer adsorption. Reducing the concentration of adsorbent significantly improved the adsorbed amount due to reduction in sheet percolation and enhanced available surface area.

Atomic force microscopy carried out on adsorbate covered graphene oxide surfaces exhibit a thickness distribution between 2-3 nm around the concentration of the first plateau described well by the Langmuir isotherm. By increasing the concentration of adsorbate, this thickness increased and a lower roughness was observed suggesting the film transitioned to a higher packing efficiency. At higher concentrations of the adsorbate, large spherical caps were observed on most of the GO surfaces. Furthermore, the thickness of

the mixed TX-100/IL complex was found to be smaller than TX-100 alone by about 41% following a similar trend as the mixed micelles in the solution phase.

Comparing the results of mixed surfactant/IL adsorption and pure surfactant (TX-100), (Figure 3-10) we can infer that surfactant alone follows the same adsorption path as the mixed surfactant/IL adsorbate does and therefore IL acts as an amphiphilic substance in the adsorption process when accompanied by surfactant. Using this method, uniform coating of IL/surfactant on GO can be applied in various applications such as energy storage.

Lastly, adsorption isotherm of P123/IL was compared to TX-100 and Tween 20 complexed with IL which revealed higher capability of this surfactant to complexed with IL as well as higher amount of adsorption of P123/IL on GO surface.

Chapter 4

Ionic Liquid/Non-Ionic Surfactant Mixtures as Versatile, Non-Volatile Electrolytes: Double-Layer Capacitance and Conductivity

Ionic liquids (ILs) are being increasingly used as processing aids to formulate electrode/electrolyte composites where the electrolyte acts as a template, defining the effective electrolyte-filled pore space between 2D materials such as graphene and MXenes. This is often facilitated with non-ionic surfactants. However, little is currently known about how these surfactants impact double-layer formation and ionic conductivity. In this chapter, aligned with my previous study on adsorption of mixed micelle on GO surface in Chapter 3,[123] I analyzed the double layer formation for two commonly used non-ionic surfactants, P123 and TX-100 mixed with the IL, EMImTFSI. A significant increase in the minimum capacitance is observed at 40 wt% surfactant by up to 88% and 102% for P123 and TX-100, respectively. On the other hand, the higher viscosity of the mixtures, lowers the ionic conductivity from 8.5 mS cm^{-1} (neat IL) to 1 mS cm^{-1} (40 wt% surfactant). Despite the significantly higher viscosity of P123/IL mixtures compared to TX-100/IL, both electrolyte series show the same reduction in ionic conductivity with respect to concentration. Pulse field gradient nuclear magnetic resonance was also used to show that for both electrolyte series, the diffusion coefficients follow a similar trend.

The results of this chapter are published in the Journal of Electrochemical Society as: Ionic Liquid/Non-Ionic Surfactant Mixtures as Versatile, Non-Volatile Electrolytes: Double-Layer Capacitance and Conductivity. [172]

For this project, I designed the experiments in consultation with Dr. Pope and all experiments were entirely conducted by myself, except NMR measurement that was performed using NMR facilities at Guelph University by Dr. Al-Abdul-Wahid. I also prepared the manuscript. Dr. Pope and Dr. Pal helped in editing of the manuscript.

This project was funded by NSERC discovery grant.

4.1 Introduction

Room temperature ILs are promising next-generation electrolytes for electrochemical applications due to their negligible volatility (at room temperature) low flammability, high ionic conductivity and thermal stability while exhibiting a wider electrochemical stability window compared to organic and aqueous electrolytes. IL's ESWs of 3-5 V promise 9 to 25-fold higher energy density compared to aqueous electrolyte for the same C_G. However, C_G is usually lower than the expected value in an IL for a variety of reasons. Ion correlations in the IL cause the effective ion concentration to be lower than expected. This reduces the intrinsic capacitance to less than 10 $\mu F/cm^2$. The high surface energy[173] and relatively high viscosity of an IL can cause wetting the entire accessible surface area of a porous electrode challenging.[174] The ions are also relatively bulky, reducing the Stern-layer capacitance and resulting in crowding effects at high voltages (i.e., high charge densities).[36] Furthermore, the relatively high viscosity can lead to comparably low ionic conductivity which can reduce their power density.

To remedy some of these challenges, diluents such as acetonitrile (AN)[175] or propylene carbonate (PC),[176] common solvents used to prepare organic electrolytes are added in some of the top performing IL-based EDCLs.[23,112] This reduces ion correlations, increases the intrinsic capacitance,[177] boosts the ionic conductivity,[177] and improves wetting.[174] However, these additives make the electrolyte systems volatile and flammable, negating most of the benefits of using an IL in the first place.[178] Alternatively, IL mixtures have been used to improve the overall performance of the device through synergic effect. [179]

In Chapter 3, we showed that non-ionic surfactant mixed with IL can impart surface active properties to IL and therefore, improve the wetting of electrode's surface. While already clearly improving the surface activity, non-ionic surfactants are also non-volatile, non-flammable, non-toxic and largely unreactive additives that could potentially be used as a diluent in place of AN or PC as discussed above. The formation

of block copolymer/IL gels have been frequently investigated as an attractive pseudo-solid-state electrolyte.[180,181] However, the presence of the surfactant in the IL phase and its effect on double-layer formation has yet to be explored.

Herein, we study the voltage-dependent capacitive behavior and the ionic conductivity of one of the top-performing and most commonly used ILs for supercapacitors, EMImTFSI and its mixtures with two commonly used non-ionic surfactants, P123 and TX-100. As it was previously mentioned, the spontaneous adsorption of IL/Tween 20 complexes onto GO by She et al. [182] reported the possibility of using Tween 20 as a self-assembly vehicle for adsorption of EMImTFSI on GO. TX-100 was chosen due to its higher capacity for complexing EMImTFSI than Tween 20 (3:1 surfactant to IL is required vs. 4:1 surfactant to IL, respectively).[123] P123 was also studied and compared to TX-100 since this surfactant contains a long PEO chain which is thought to reduce ion associations in similar ILs due to its high polarity.[183] It can therefore potentially add beneficial attributes to the electrolyte system. Furthermore, according to our preliminary studies, the required amount of this surfactant for stabilization of EMImTFSI is even less than TX-100 (1:1 surfactant to IL) and it resulted in higher adsorption of IL on GO surfaces (Chapter 3). Mixtures of up to 60 wt.% and 50 wt. % surfactant for TX-100 and P123 respectively are investigated using model, polished, glassy carbon electrodes in a 3-electrode configuration. These results are compared to measurements of viscosity and self-diffusion using pulse field gradient nuclear magnetic resonance (PFG-NMR).

4.2 Experimental Methods:

Materials:

EMImTFSI was purchased from IoLiTec (high purity 99%, Germany), TX-100 was purchased from EDM Millipore Co., P123 was purchased from Aldrich, dichloromethane (DCM) was purchased from

Honeywell and ferrocene (Fc) was purchased from Aldrich. The aluminum oxide polishing powder and polishing pads were purchased from CH instruments.

*Methodologies**:***

Three electrode measurements were carried out by placing 3 ml of electrolyte into a clean, glass electrochemical cell (CH Instruments) which was covered with a Teflon cap and sealed using a silicon O-ring. A 3 mm diameter glassy carbon (GC) rod electrode (CH Instruments) was used as a working electrode, a Pt mesh (Alfa Aesar) as counter electrode and a Pt wire (CH Instruments) was used as a pseudoreference electrode. The GC was polished before use on three different micro-cloth pads using a 1, 0.3 and 0.05 MicroPolish powder and sonicated in ultrapure water for 10 min. The Pt mesh counter electrode was cleaned by performing cyclic voltammetry in 0.5 M sulfuric acid and then sonicating in acetone and ultrapure water for 10 min. The Pt wire was placed in an enclosed glass capillary with porous Teflon tip which was filled with pure EMImTFSI. The potential of the pseudo reference electrode was calibrated using the known redox potential (0.4 V vs. SHE) of 1 mM Fc dissolved in EMImTFSI immediately after each measurement.

Each electrolyte was made by mixing the required amount of surfactant and IL with DCM (DCM/IL: 1/1 weight ratio) in a glass vial, then stirring them using a Teflon stir bar for 1 hour, followed by drying under flowing dry nitrogen overnight. This mixing procedure was adopted since it was proven to yield the most uniform and thermodynamically stable mixture (According to Lodge et al. [184] the self-assembly of surfactant in ionic liquid is path-dependence). The final mixture was then dried under vacuum at 110° C for 7 hours to remove any excess water and solvent impurities. The final mixture is a uniform, transparent liquid with a higher viscosity than the pure IL. The increase in viscosity limited the maximum concentration to 50 wt.% for P123 electrolyte series. Higher concentrations would no longer flow into the 3-electrode cell. For TX-100 up to 60 wt.% of surfactant was tested. The moisture content of the mixtures was tested

using Karl Fischer titration and found to be under 200 ppm. The addition of surfactant lowered the voltage stability window likely due to impurities that the surfactant introduces into the system.

Electrochemical testing was performed using a Biologic SP-300 and with electrodes housed in a three-electrode cell. Cell assembly was performed in an argon-filled glovebox with water and oxygen content of less than 1 ppm. The cell was then sealed in an air-tight bag and immediately transferred into a glove bag which was purged three times with nitrogen and kept under flowing nitrogen during the test. This was to eliminate some of the noise we found when testing was performed inside the glovebox. CV was performed at 50 mV/s, at first, to determine the electrochemical stability window (ESW) and then, before each test to clean the glassy carbon surface of adsorbed contaminants. The cut off current chosen for the ESW measurement was 10 $\mu A/cm^2$. In the literature, the cut off current is normally taken as 0.1 mA/cm^2. [185] However, we chose this smaller value to better eliminate any residual faradaic response from trace water and other contaminants. Ohmic drop compensation was carried out using the ZIR function in the EC-lab software using a frequency of 10 kHz at 80% compensation. The resulting solution resistance was recorded and used as a relative measure of the electrolyte conductivity to supplement conductivity testing in a 2-electrode cell. A schematic of both two-electrode cell and three electrode cell is depicted in Figure 4-1 for comparison. Potentiostatic Electrochemical Impedance Spectroscopy (EIS) was then conducted using a perturbation of 10 mV at frequencies ranging from 1 MHz to 0.1 Hz from open circuit voltage (V_{OC}) to approximately -1 V vs. Fc with an increment of 0.1 V. The electrode was then rested at V_{OC} for 30 min and polarized to +1 V vs. Fc. Between each voltage increment, the electrode was kept at rest for 2 mins. This method has been deemed to be the best practice to avoid hysteresis at the IL/electrode interface.[186]

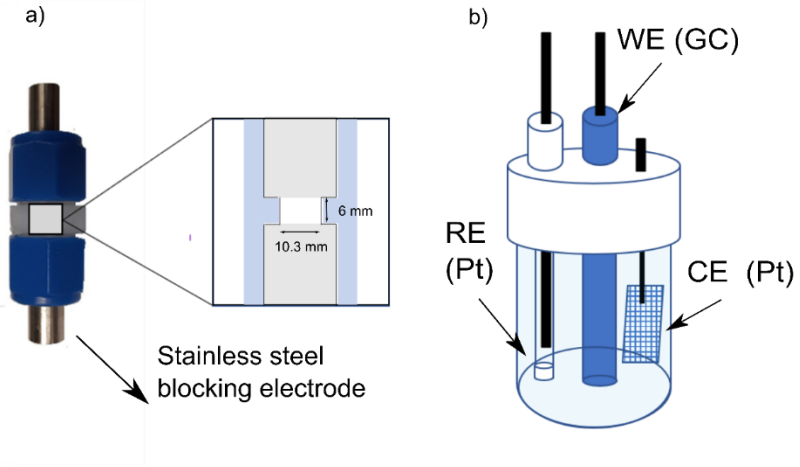

Figure 4-1: Cell configuration, two electrodes vs. three electrode a) two electrode cell (Swagelok), b) three-electrode cell

The differential capacitance data were calculated by fitting the impedance data to an equivalent circuit model (using EC-Lab's Zsim fitting routine). An RQ equivalent circuit model[185] (series resistance and constant phase element) was used over specified frequency ranges which will be discussed in the Results and Discussion section. The double layer capacitance was averaged over the chosen frequency range using eq. 4-1.

$$C_{dl} = Average\left(\frac{Q(2\pi f)^{\alpha-1}}{sin\left(\frac{\alpha\pi}{2}\right)}\right) \qquad \textit{Equation 4-1}$$

where f is the frequency, Q is a fit parameter, and α is an exponent signifying the non-ideal behavior of the impedance. The closer the value of α to 1, the more ideal the capacitor.

To evaluate the equivalent series resistance (ESR) of the system, the data were fitted to a series combination of a resistance with a parallel RC component. Each experiment was performed three times to

confirm the repeatability of the data. The frequency ranges for this modeling were chosen to encompass the semicircle region on the impedance plot.

Measurements of the ionic conductivity were performed in a Swagelok cell, between stainless steel rods, and calibrated using a standard electrolyte solution with conductivity of 1431 µS/cm. The measurement was performed at ambient temperature (~20°C). NMR molar conductivities were calculated from the Nernst-Einstein relation using NMR diffusivity values:

$$\Lambda_{NMR} = \frac{Ne^2}{BT}\,(D_+ + D_-) \quad , \qquad \textit{Equation 4-2}$$

where N is the Avogadro's number, e is the electric charge on each ion, B is the Boltzmann constant, T is the absolute temperature and D_+ and D_- are diffusivities for cations and anions, respectively.

To estimate conductivity from the NMR results, the molar conductivities in Sm^2/mol were multiplied with the IL's molar volume (3890 mol/m^3 at 20°C).[187] For the electrolyte/surfactant mixture series, this molar volume was corrected for the added volume of the surfactant assuming they formed an ideal mixture.

Rheological measurements were performed on a Kinexus Pro (Netzsch, Germany) rheometer using a cone and plate geometry with angle of 2° and diameter of 4 mm. Cone and plate geometry is often used in rheological measurement of IL.[188–191] The measurements were carried out in rotational mode. To avoid the adsorption of water into the already dried IL, the cone and plates were covered using a solvent trap under flowing nitrogen. The electrolyte was sheared over a frequency range of 1 to 1000 Hz. At frequencies ranging from 10 to 1000 Hz, Newtonian behavior was observed and the viscosities were reported in this range.

The PFG-NMR were performed on a Bruker AVANCE III 600 MHz spectrometer, using a room temperature probe equipped with a 5.57 G/cm*A gradient coil. The sample temperature was regulated at 20° C and calibrated using a 4% methanol sample prior to each set of experiments. Diffusion measurements

were performed using the BPP-LED (bipolar pulse pair – longitudinal-eddy-current delay) sequence of Wu et al.[192] (*i.e.* the *ledbpgp2s* sequence as provided by the spectrometer vendor). 1H DOSY measurements were performed using encoding/decoding gradient pulses of a smoothed-square shape (SMSQ10.100 as provided by the spectrometer vendor), 1.5 ms in duration (i.e., 3 ms for each bipolar pulse pair), and with intensity varied in 24 linear steps from 2.51 to 47.6 G/cm (i.e., 5 to 95% of maximum power). The diffusion time between the gradient pairs was set to 350 ms. 16 transients were collected at each gradient strength, with a ~8 second relaxation delay between scans, for a total experiment time of roughly 1 hour. 19F DOSY measurements were collected using similar parameters, except that encoding/decoding gradient pulses were increased to 2 ms in duration (i.e., 4 ms for each bipolar pulse pair). The data analysis was performed by fitting the data to[193]

$$Ln(E) = Ln\left(\frac{S}{S_{g=0}}\right) = -\gamma^2 g^2 D\delta^2(\Delta - \frac{\delta}{3}) \quad , \qquad \textit{Equation 4-3}$$

where *S* is the spin echo signal intensity, δ is the duration of the field gradient with magnitude g, γ is the gyromagnetic ratio and Δ is the interval between two gradients pulses and *D* is the diffusion coefficient. The fitting was performed using Dynamic Centre provided by Bruker. An example of the fitted curve is provided in Figure 4-2.

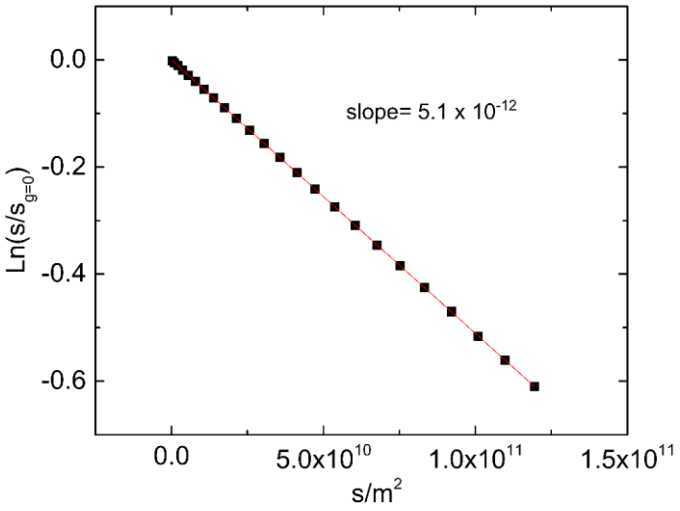

Figure 4-2: Example diffusion coefficient analysis using Dynamic Center software for anion in 40% P123, the slope of the curve is the value for diffusion coefficient

4.3 Results and Discussion

Figure 4-3 shows a representative CV of the dried EMImTFSI from -2.5 to +1.5 vs. Fc. A significant oxidative decomposition did not occur until 2 V vs. Fc and significant reduction did not occur until the potential was brought lower than -2.5 V vs. Fc, demonstrating the high intrinsic ESW for EMImTFSI of 4.5V (chosen based on cut-off current of 0.1 mA/cm^2) which is comparable to values reported in the literature.[177] The ESW chosen for double layer testing, however, was based on a cut off current of ~10 µA/cm^2. This small cut off current was chosen to avoid faradaic contributions from trace contaminants.

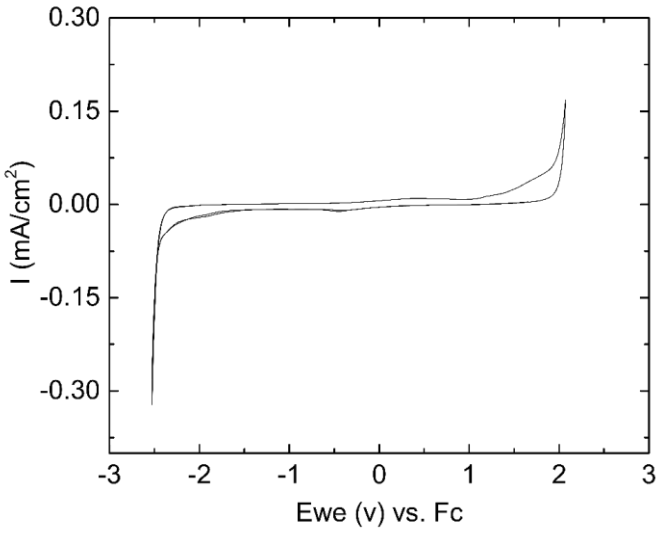

Figure 4-3: Representative CV of dried EMImTFSI

Addition of surfactant was found to lower the ESW of EMImTFSI which can be seen in Figure 4-4 for a subset of concentrations for each surfactant. This effect was reported for addition of water to LiTFSI/AC electrolyte,[194] and several ionic liquids.[195] Both surfactants reduce the ESW by about 1 V. The TX-100 electrolyte series displays the same ESW regardless of the amount of surfactant. However, for P123, the ESW shrinks with further increase in the amount of surfactant.

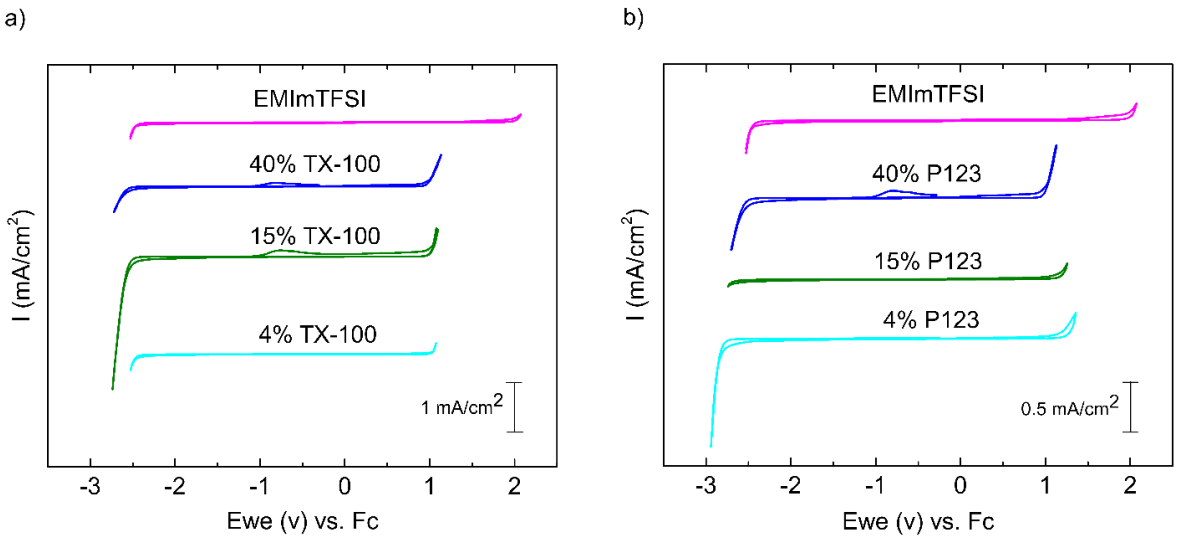

Figure 4-4: Electrochemical stability windows for electrolyte series, a) 4, 15 and 40 wt.% TX-100 electrolyte series, b) 4, 15 and 40 wt.% P123 electrolyte series

This reduction in ESW of ILs is potentially due to several interactions and bonding between IL and surfactants molecules. This should be noted when this electrolyte system is used in a device such as a supercapacitor or battery where the potential limit of the positive electrode will have to be reduced. For both surfactants, at 40 wt.%, a peak appears on the oxidation curve, which is likely the oxidation of the decomposition product from reduction at ~ -2.5 V vs Fc. This peak is also observed for 15 wt.% TX-100 which went to a slightly higher negative limit and generated more decomposition product. To further confirm the source of this peak, we refer the reader to Figure 4-5, where the CVs of these electrolytes in the narrower potential window were shown demonstrating the absence of such peak.

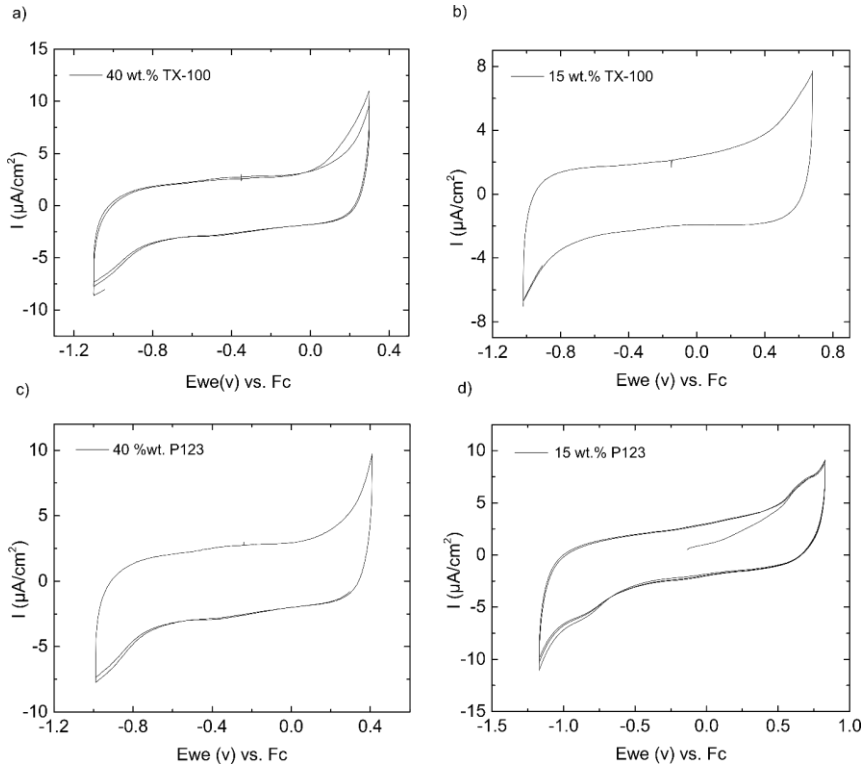

Figure 4-5: CVs for selected electrolyte series depicting voltage windows chosen for EIS, a) 40 wt.% TX-100, b) 15 wt.% TX-100, c) 40 wt.% P123, d) 15 wt.% P123

In Figure 4-3 a, the Nyquist plots of pure EMImTFSI at different voltages are plotted. A deviation from ideal capacitive behavior is observed, especially at higher polarizations which is known to be due to voltage-induced inertial motion which contributes to a distribution of time constants.[196] At -1.0V, faradaic charging mechanisms become more noticeable as observed by the emergence of a low frequency semi-circle in the Nyquist plot (Figure 4-3 a) and a significant deviation from the expected -90° phase angle for capacitive charging (Figure 4-6 b).

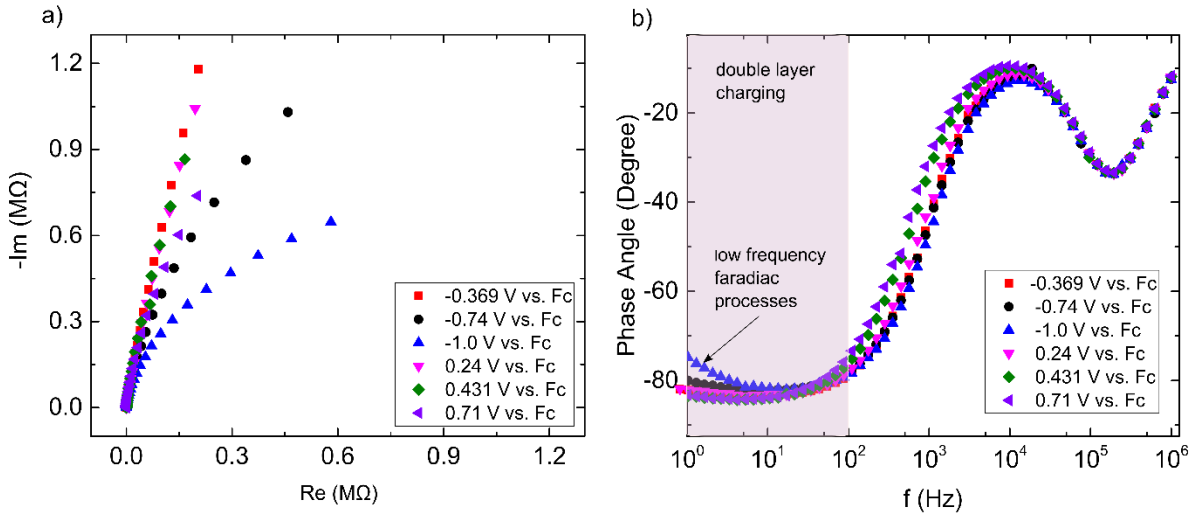

Figure 4-6: Impedance plot and phase angle comparison for chosen potentials, a) Impedance plot of chosen voltage, b) Phase angle vs. frequency curve for EMImTFSI at different potentials

This faradaic charging is the result of a trace contaminant that was found to be present in some batches of the IL used. However, we believe this contamination did not influence our capacitance measurement since a stricter cut off current (10 μA/cm^2) was chosen for these measurements to avoid potentials with significant faradaic response. These narrower voltage windows were shown in Figure 4-5.

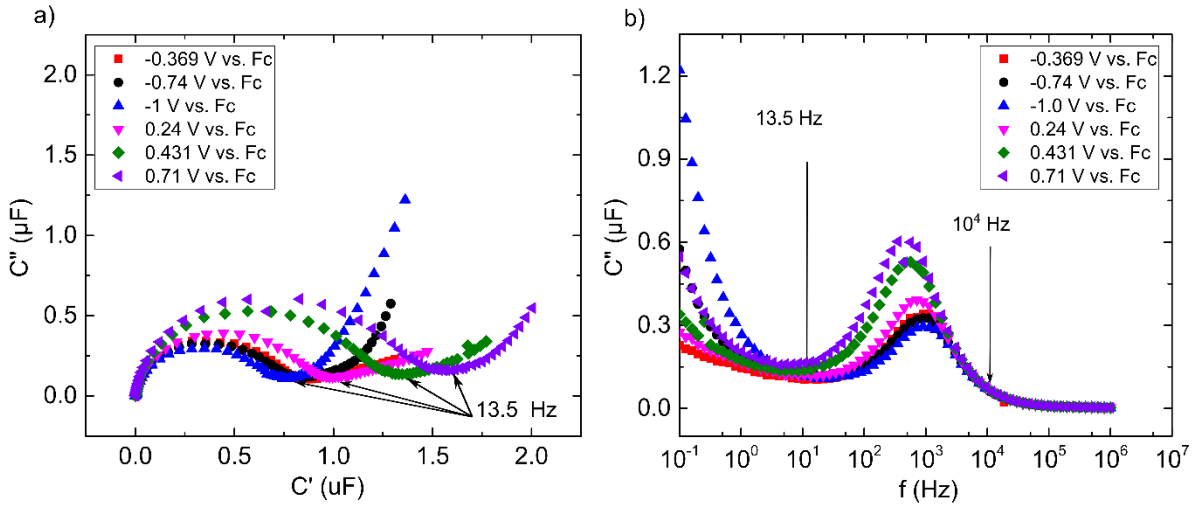

Figure 4-7: C-C plot and imaginary capacitance vs. frequency, a) C-C plot for the chosen voltage, b) Imaginary capacitance vs. frequency for chosen voltages

Figure 4-3a, shows the complex capacitance plot (C-C plot) for the chosen voltages. At high frequencies, depressed semicircles are observed followed by a linear rise. According to Drüschler et al.[197] a perfect semicircle signifies an ideal capacitive behavior whereas a depressed semicircle indicates the existence of non-ideal capacitive charging. The first semicircle demonstrates fast capacitive behavior with relaxation time of ~0.2 ms which was described by Rolling et al.[198] in more details. As it can be seen from the Figure 4-7a, up to a frequency of 13.5 Hz, this fast capacitive phenomenon is observed. At lower frequencies, the onset of another capacitive process emerges which is not in the scope of this study and therefore was not fully captured. Figure 4-3b, shows the complex capacitance vs. frequency range. According to this plot, the area enclosed between the two arrows shows the frequency domains chosen for our equivalent circuit fits.[196]

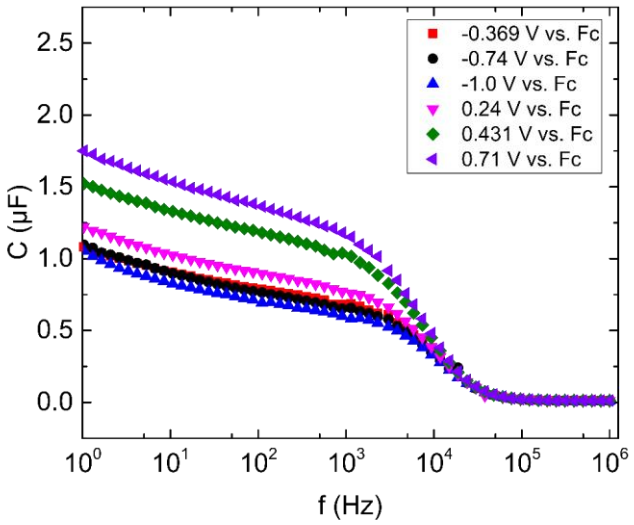

Figure 4-8: Frequency dependence of capacitance of EMImTFSI, the knee frequency shift to lower values from negative to positive potentials

Figure 4-8 shows the frequency dependent behavior of EMImTFSI at different studied potentials. The capacitance dispersion can be observed through all potential range studied and is usually attributed to inhomogeneity of surface structure and charge distribution.[198] The knee frequency shifts to smaller values as we move from negative potentials to more positive potentials and the overall capacitance increases.

Analysis of double layer with respect to surfactant concentration and electrode potential:

In this section, we analyze the capacitive charging mechanisms at the GC/IL interface when up to 60 wt.% non-ionic surfactant is mixed with the EMImTFSI. Figure 4-9c shows the capacitance vs. potential plot for the neat EMImTFSI follows a wide V-shape which is flatter at more negative potentials with a steeper rise at positive potentials. These results match those of Bozym et al.[177] who studied a similar electrochemical window with the same electrolyte. As can be seen in Figure 4-9a and b, the capacitance at the open circuit voltage ($C_{dl\text{-}voc}$), which we assume is similar to point of zero charge (PZC), increases with increasing the percentage of either surfactant and reaches a maximum near 40 wt.%.

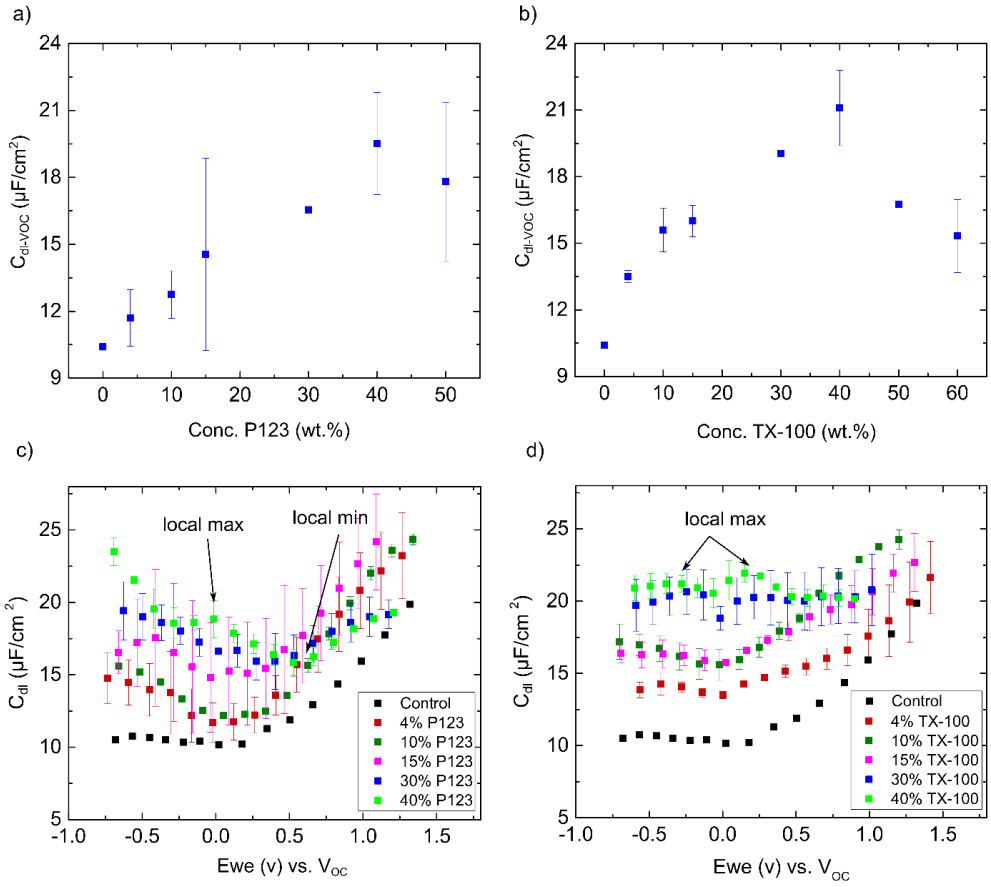

Figure 4-9: Electrochemical characterization of IL/surfactant mixtures; a) Cdl-Voc of P123/EMImTFSI series electrolyte vs. concentration of P123, b) $C_{dl\text{-}Voc}$ of TX-100/EMImTFSI series electrolyte vs. concentration of TX-100, c) C_{dl} of P123/EMImTFSI electrolyte series vs. potential, d) C_{dl} of TX-100/EMImTFSI electrolyte series vs. potential

The capacitance estimated at a single frequency is also provided in Figure 4-10: which largely follows the capacitance calculated based on modeling over the frequency range shown in Figure 4-3a and b. The single frequency measurements were performed at 10 Hz where it is located half way between the knee frequency and the very low end of frequency on a straight line based on analysis of capacitance vs. frequency curve in Figure 4-8. Each method estimates a capacitance of ~10 μF/cm^2 for the neat EMImTFSI which is slightly smaller than the values reported by Klein et al.[196] 12.78 μF/cm^2 who fit over an extended

frequency range and the 12 μF/cm^2 reported by Namjundia et al.[199] whose estimate was based on a fixed frequency of 1 kHz.

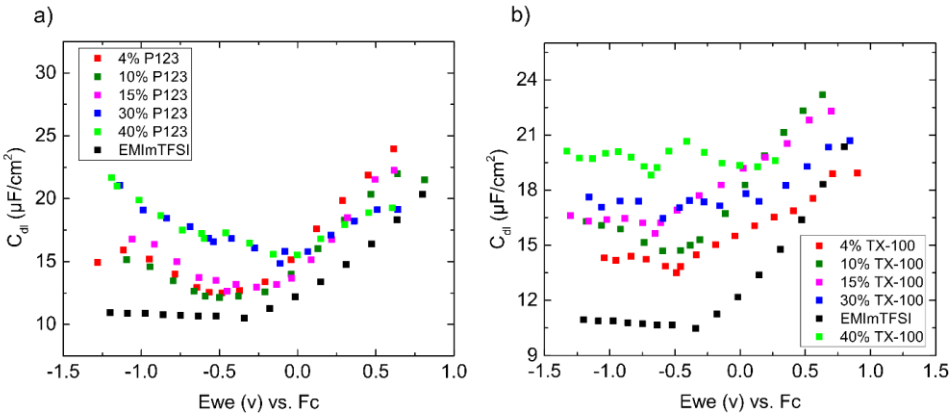

Figure 4-10: Single frequency (10 Hz) double layer capacitance measurement, a) P123/ EMImTFSI series, b) TX-100/EMImTFSI series.

Upon further increase in the surfactant concentration up to 50 wt. % and 60 wt. % for both surfactants, the capacitance starts decreasing (Figure 4-11 a and b). This decrease can be explained by the lowering of the ion concentration as we dilute the electrolyte with surfactant. However, the original increase in capacitance with surfactant addition is anomalous. The capacitance vs. potential plots for concentrations above 40 wt.% are shown in Figure 4-11. In addition, the drop in capacitance is also shown in Figure 4-9 a and b.

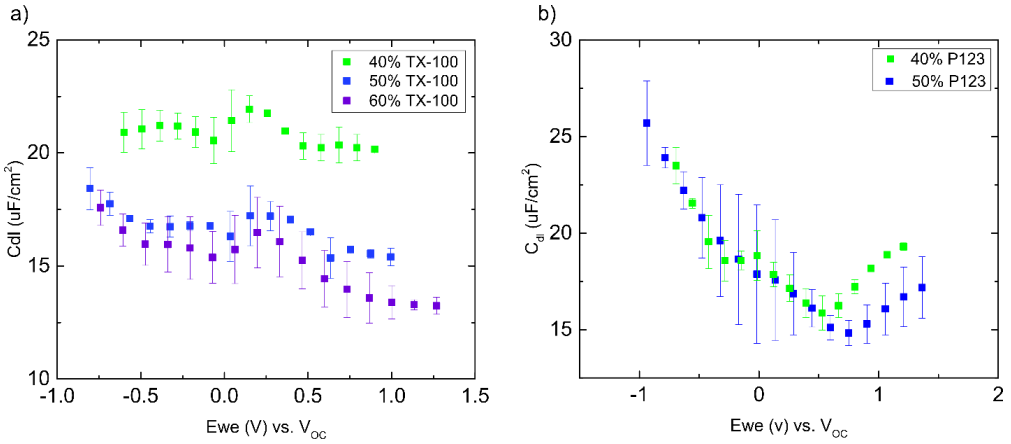

Figure 4-11: Comparison of capacitance vs potential curve for 40%, 50% and 60% surfactant, a) 40%, 50% and 60% TX-100 addition to EMImTFSI, b) 40 % and 50% P123 addition to EMImTFSI

The increase in capacitance with addition of surfactant implies that despite the relatively low dielectric constant and high viscosity of the neat non-ionic surfactants, there is a significantly beneficial effect on the capacitance (an increase by a factor of 88 % and 102 % for P123 and TX-100, respectively). It suggests that non-volatile additives can play a similar role to organic solvent-based diluents which are able to reduce the effect of ionic associations in pure ILs. [200] The positive impact of low dielectric constant on capacitance was also observed by Bozym et al. [177] where the capacitance in the EMImTFSI system was found to be highest in DCE, followed by AN and PC. Lee et al.'s scaling analysis demonstrated that this effect, in concentrated electrolytes, can be explained by the increase in effective charge acquired by the ions when surrounded by a lower dielectric constant solvent. Thus, dilution in this regime reduces the effective Debye length. [201] This can also be explained in terms of ionic associations: the surfactant interactions with IL molecules could result in breaking the ionic association in ILs that are responsible for reducing the average charge on each ion. With further increase in the surfactant concentration, the capacitance drops. As we move from 40 wt. % surfactant to 50 wt. % surfactant, we are changing the system from a solvent-in-salt system to a salt-in-solvent of low dielectric constant surfactant. According to Gouy-Chapman model, a drop in concentration from 3.67M (4 wt.%) to 1.23 M TX-100 (60 wt.%) will lead to a monotonous drop in

diffuse layer capacitance from 139 μF/cm^2 to 81 μF/cm^2 (assuming the relative permittivity of TX-100 to be 8), [202] which will reduce the observed capacitance when added in series with Helmholtz capacitance. However, our data shows a nonmonotonic behavior of capacitance with respect to concentration. This behavior which was also observed for electrolytes of high concentration is likely caused by the Debye length being a nonmonotonic function of concentration. [203] We should also note that increasing the surfactant amount can drastically change the composition of the Stern layer. On one hand, it is likely that a thicker layer of low dielectric constant surfactant will exist within the Stern layer. On the other hand, ion-ion interactions will be lessened reducing the effective solvation shell of ions at higher concentrations (to be discussed in more detail further). A combination of all these factors results in the observed maximum in the capacitance.

As shown in Figure 4-9c, addition of P123 to the IL significantly changes both the shape and magnitude of the capacitance curve. For P123, the near-flat curve observed for pure EMImTFSI at negative potentials, rises more steeply with the overall capacitance at all potentials increasing in magnitude. The increasing slope in the negative branch may be correlated with the reduction of the packing factor (φ) in Konyshev's theory of double layer in ILs. [36] This was also observed by Seddon et al. [204] and can indicate a more efficient packing of the cations when the electrode is negatively polarized. The minimum capacitance for pure EMImTFSI is near the V_{OC}. For all concentrations of P123, the V_{OC} remained fairly constant with values ranging between ~ -0.5 V and -0.6 V vs Fc with no systematic variation as shown in Figure 4-12a. As depicted in Figure 4-9c, with increasing the concentration up to 40% P123, a local maximum emerges near ~ V_{OC}. This shifts the global minimum in the capacitance to more positive potentials.

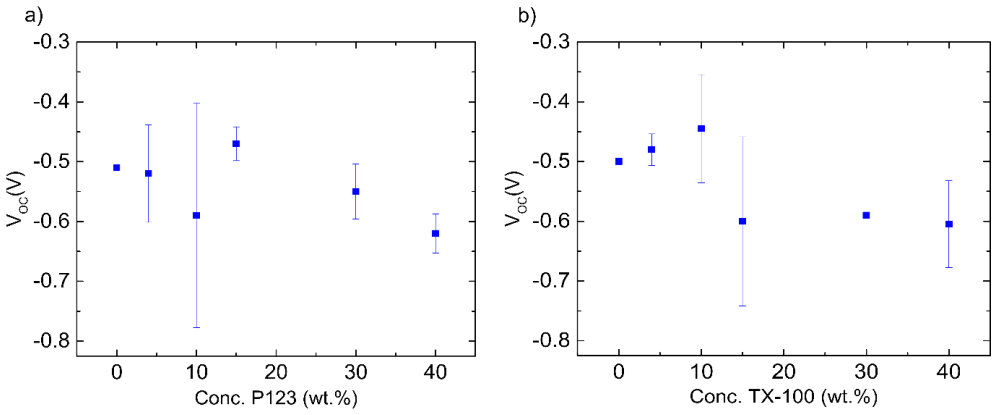

Figure 4-12: The location of potential of zero charge vs. Fc, a) Potential of zero charge (V_{OC}) with respect to concentration of P123, b) Potential of zero charge with respect to concentration of TX-100

In Figure 4-9d, the capacitance vs. potential for TX-100/EMImTFSI mixtures are shown. The overall increase in capacitance is larger than what is observed for the P123/EMImTFSI mixtures. Contrary to the P123 case, the slope of the negative branch doesn't increase significantly. Similar to the P123 case, increasing the surfactant concentration causes local maxima to emerge again near ~0.15 V vs. V_{OC} accompanied by an adjacent maximum as indicated on the plot at just above ~-0.3 V vs. V_{OC}. In the literature, these maxima or camel-shaped curves are often attributed to the points at which the maximum packing density is achieved for anions/cations in the first monolayer of adsorbed ions to the electrode surface. [196] However, the potential range between these features is too narrow compared to previous reports (1.38 V between maxima in the Kornyshev's model vs. ~0.53 V between maxima in our case). At higher positive potentials, the capacitance further increases, which is also evidence that suggests that these maxima are not due to packing density limitations. It is more likely that specific adsorption induced by the presence of the surfactants may play a role in establishing these features. Similar to the P123 case, the V_{OC} is fairly constant with concentration (Figure 4-12 b). While specific adsorption often shifts the V_{OC} in ionic systems, the non-ionic surfactants studied are not charged and thus would not be expected to change the charge density upon adsorption.

Effect of surfactant on the ion diffusivity, viscosity and conductivity:

We now determine the impact of the non-ionic surfactant diluents on the ionic conductivity using EIS measurements in a two-electrode cell and compare these results to changes in viscosity and self-diffusion carried out by PFG-NMR. As shown in Figure 4-13a, for both non-ionic surfactants, the conductivity dropped monotonically with surfactant addition from 8.5 mS/cm for the neat IL, which is close to the value reported in the literature, [199] to nearly 1 mS/cm with 40 wt.% surfactant. The decrease in ionic conductivities is indicative of a shift in knee frequencies for both electrolyte series which will be discussed later in this chapter.

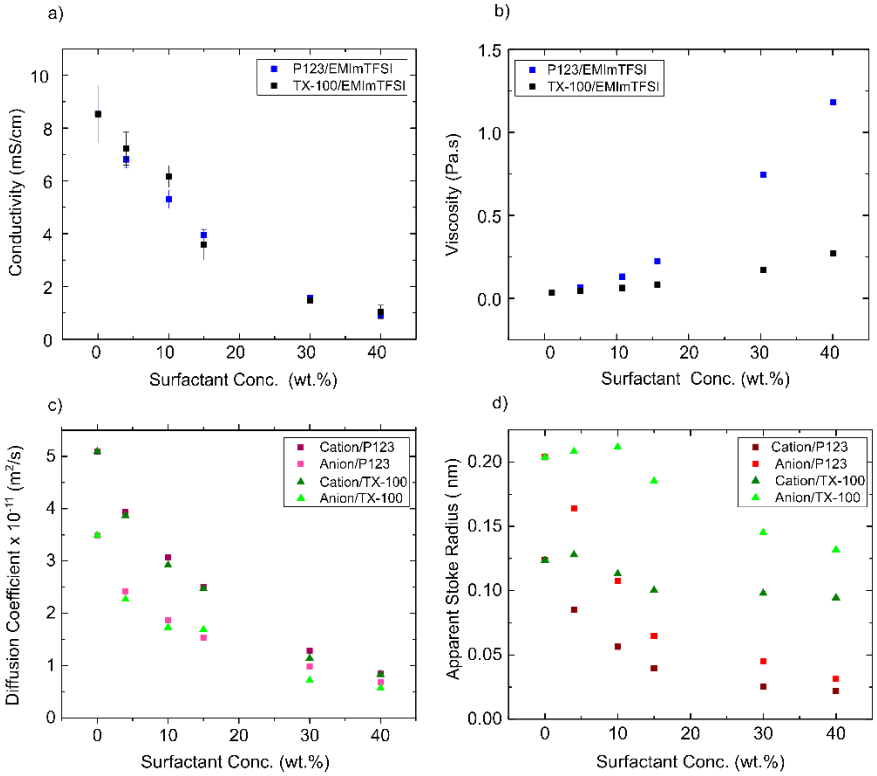

Figure 4-13: Diffusion coefficient, conductivity and viscosity of electrolyte series, a) EIS conductivity of both P123 and TX-100/EMImTFSI electrolyte series, b) Viscosity of P123 and TX-100/EMImTFSI electrolyte series, c) Diffusion coefficient for P123 and TX-100/EMImTFSI electrolyte series, d) The relation between Stoke-Einstein radius and surfactant concentration in both electrolyte series

This monotonic drop is contrary to organic solvent diluents which typically show a conductivity maximum at intermediate dilution due to their ability to lower the mixture viscosity. [177] On the other hand, as shown in Figure 4-13b, the viscosity of the IL/non-ionic surfactant mixtures increase monotonically upon the addition of the non-ionic surfactant. However, there was a significant difference observed between P123 and TX-100 with mixtures containing P123 being nearly sixfold more viscous at 40 wt.% - a difference which was not reflected in the conductivity measurements. Ionic conductivity should be inversely proportional to the viscosity as this decreases the diffusion coefficient based on the Stoke-Einstein relation:

$$D = \frac{BT}{C\pi\eta r} \quad , \qquad \textit{Equation 4-4}$$

where B is the Boltzmann constant, T is the absolute temperature, η is the viscosity, r is the effective hydrodynamic radius of the molecules, C is a constant which depends on the system being studied (usually between 4-6), and D is the self-diffusion coefficient. To further investigate this discrepancy, we used PFG-NMR spectroscopy to measure the self-diffusion coefficient in our electrolyte series. The measured self-diffusion coefficients of each ion for both surfactant groups at 20 °C are shown in Figure 4-13c. The values reported for pure EMImTFSI largely agree with the literature values reported for this IL at the same temperature.[187] As shown in Figure 4-13c, the cation self-diffusivity is higher than for the anions. This is likely related to their larger van der Waals (vdWs) volumes (143 Å^3 for TFSI compared to 118 Å^3 for EMIm).[191] However, comparing the calculated vdW radius (r_{vdW}) ratios with the ratio of the diffusivities for both ions ($r_{vdW\text{-}EMIm}/r_{vdW\text{-}TFSI}$ = 0.93 vs. D_{TFSI}/D_{EMIm} = 0.68), the hydrodynamic radius (r) of TFSI should be larger than its vdW radius. This is similar to what has been observed by Hussey *et al.*[205] and others[206] who have observed that the diffusivity of the anion is roughly half what would be expected based on its ionic radius as it drags tightly bound cations with it. This is observed for both surfactants and at all concentrations. The self-diffusivities of cations and anions for the electrolyte series with both surfactants become smaller with increased surfactant concentration as expected due to the increase in solution viscosity. At higher

surfactant concentrations, the diffusivities for cations and anions are closer in value likely due to the breaking up of ion-ion interactions for surfactant-ion interactions. However, it is clear that in all cases, the diffusivities measured in both surfactant groups are quite similar despite their largely different viscosity which is in line with the conductivity measurements carried out by EIS but is inconsistent with the Stoke-Einstein relation. To better illustrate this deviation, in Figure 4-13d, we plot the apparent Stokes radius (r_S) of ions using a value of 6 for the constant C in Stoke-Einstein relation (the exact value is difficult to know precisely).[207] According to Figure 4-13d, r_S decreases with increasing surfactant concentration with a stronger decrease with P123 due to the larger viscosity change. While maybe a simplified view, this may indicate that both surfactants and, in particular, P123, reduce interactions between the ions which now diffuse more as naked ions rather than as a complex as indicated by the reduction in the apparent r_S. To understand why such different behavior is observed, we take a closer look at the polarity and structure of both surfactants. TX-100 is a relatively small molecule with molecular weight (MW) of 625 g/mol compared to 5800 g/mol for P123 which is reflected in their viscosity differences. TX-100 consists of a phenyl group, an alkyl tail and a polyethylene oxide (PEO) with chain length of, on average, 9.5 units. P123 on the other hand, is a triblock copolymer with polyethylene oxide (PPO) of 70 units, which is bonded to PEO (30 units) in a symmetrical fashion. Although the polarity values of these surfactants are not available in the literature, we can make some estimates according to their PEO chain length. Since the dipole moment of PEO increases with its chain length,[208] the average polarity of P123 with longer PEO chain likely exceeds that of TX-100. According to Osti et al.[183] a solvent with higher polarity, is able to better screen ion-ion interactions. This effect was also observed in a PEO-imidazole ionic liquid oligomer electrolyte which demonstrated that an increase in the chain length of PEO up to a certain point led to more ionic dissociation and improvements to the ionic conductivity. Further increases in the chain length (i.e., MW > 750) led to a significant reduction in conductivity due to the higher viscosity of the higher MW polymers.[209] In addition, the reduction in Stokes-Einstein radius data with an increase in the surfactants' concentration implies a

reduction in size of the solvation shell. This reduction in effective size normally results in a higher diffusivity. [210] However, in our case, the high viscosity caused by the addition of the surfactant has a more significant impact on the ionic diffusivities, causing them to be smaller with increasing surfactant amount. Overall, this result implies that viscosity plays a more prominent role in dictating the self-diffusivity than the solvation effect. Figure 4-14 compares the conductivity values obtained by NMR and EIS methods. Both show a very similar trend but are offset with NMR conductivities being consistently higher. This difference may be a result of our assumption of ideal mixing or volume additivity which is likely highly non-ideal and provides significant uncertainty in our estimation of the concentration of IL and thus the NMR conductivity. Furthermore, there is a significant difference in the time scales of each measurement technique: 0.350 s for PFG-NMR compared to ~0.3 ns for EIS. Regardless, both results show similar trend where the conductivity for P123 and TX-100 electrolyte series are reducing with surfactant concentration but remain high enough for most applications. The difference between NMR and EIS conductivity estimates with ILs has been observed in the literature and was associated with ion-pair effect in ILs.[187] However, recent analysis and modeling contradict the existence of such permanent ion-pairs and referred to the effect of dielectric screening of the ionic charges due to short-lived ionic correlations.[211] In pure ILs, the dielectric screening reduces the average charge of the ions to lower than the value assumed in Nernst-Einstein relation. As was discussed in the previous section, by adding low dielectric constant solvents such as non-ionic surfactant, the dielectric screening will be reduced which will result in an increase in the average charge on each ion.

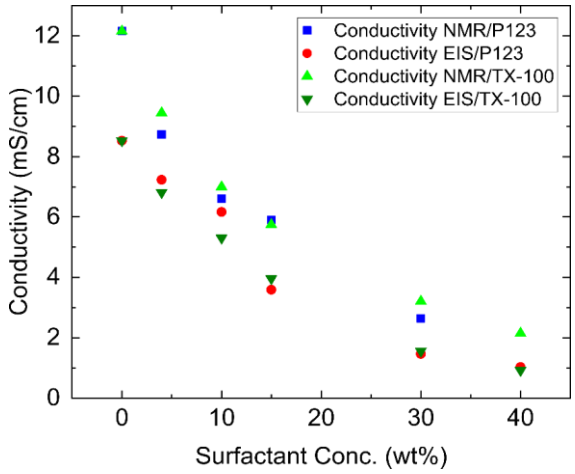

Figure 4-14: The comparison between NMR and EIS conductivity for both P123 and TX-100 electrolyte series

To further study the effect of surfactant on the performance of the electrolyte, the knee frequencies of the electrolyte series is compared in Figure 4-15. Figure 4-15a and b demonstrate the average values of the frequency dependance of double layer capacitance for both electrolyte series in three electrode configurations. As it can be seen for both surfactants, the capacitance increases with the concentration of the surfactant and the knee frequency shifts to the lower values which can be more clearly seen on Figure 4-15c and d. As the knee frequency is related to the frequency at which the capacitance starts to degrade, the higher the knee frequency, the better the rate performance of the device.

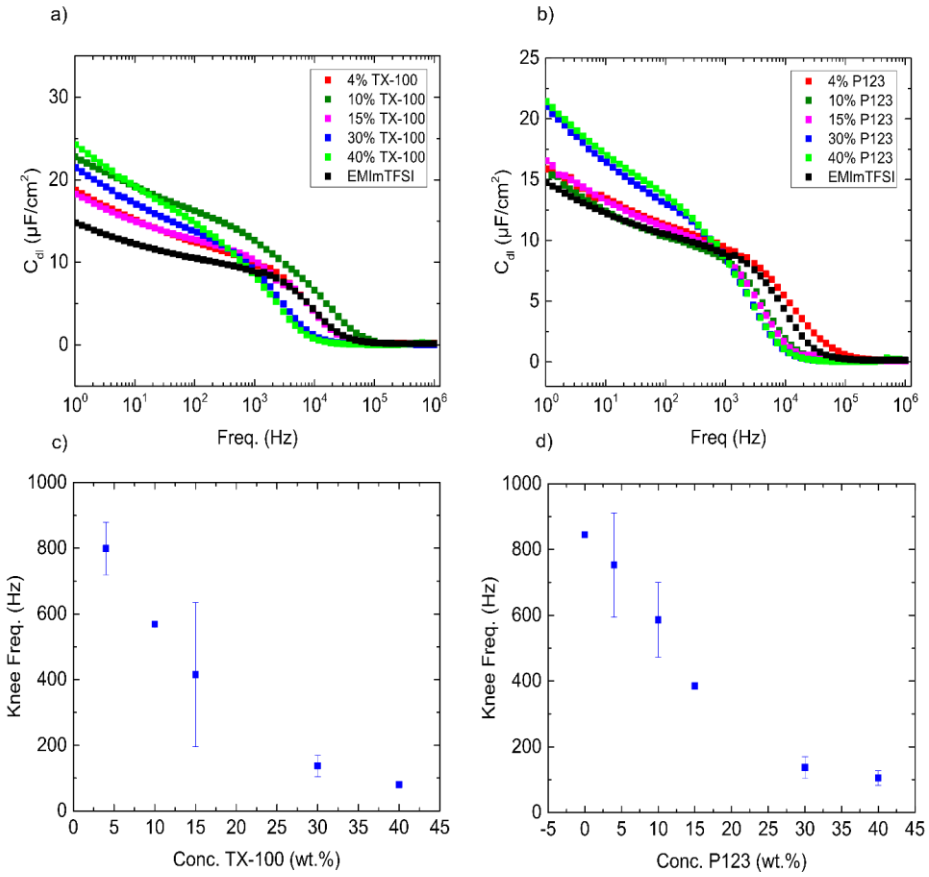

Figure 4-15: Knee frequency and frequency dependence of capacitance at V_{OC}, a) dependence of double layer capacitance to frequency for TX-100/EMImTFSI series, b) dependance of double layer capacitance to frequency for P123/EMImTFSI series, c) Knee frequency of TX-100/EMImTFSI electrolyte series, d) Knee frequency of P123/EMImTFSI electrolyte series

To make sure the values reported for conductivity of electrolyte series based on two electrode system match our three electrode configurations, we have compared the resistance from two-electrode cell with that of three electrode cell (Figure 4-16) which shows very similar behavior. However, the three-electrode cell shows higher resistance at all concentration of surfactant. This can be attributed to the difference in the geometry of the two cells which will impact the cell constant.

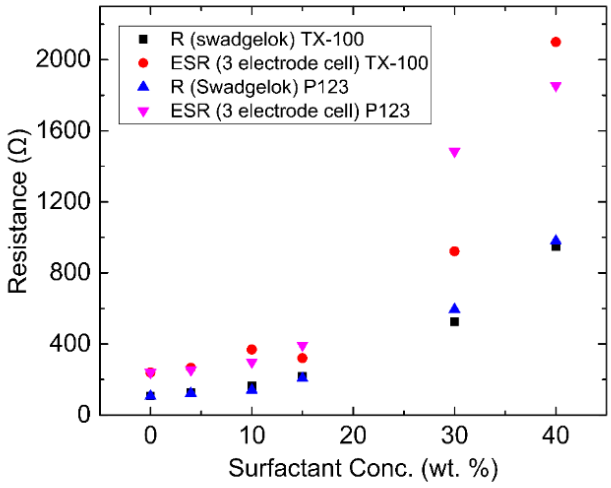

Figure 4-16: Comparison of the resistance of two electrode cell with three electrode cell

4.4 Conclusions

Using a three-electrode cell and Electrochemical Impedance Spectroscopy (EIS), we measured the double layer capacitance of various IL/non-ionic surfactant mixtures in contact with glassy carbon as a function of concentration and DC potential. We demonstrate a significant enhancement of the double-layer capacitance up to 40 wt.% surfactant addition using these non-volatile additives, a behavior contrary to the Gouy-Chapman model. Since ILs are concentrated electrolytes, their double layer behavior cannot be fully explained by Gouy-Chapman-Stern model. Upon further dilution, with both surfactants, a reduction in capacitance was observed. This behavior is analogous to the role that some volatile organic solvents such as AC and PC play when mixed with ILs. This effect can also be explained by considering the low dielectric constant of the non-ionic surfactants as well as their specific molecular interactions with EMImTFSI which leads to an increase in the average charge of each ion. Since these surfactants are increasingly added to ILs in self-assembly based electrode strategies, or as gelators, our work suggests that they do not need to be removed and can positively impact the electrochemical performance of energy storage devices like supercapacitors. However, the required surfactant/IL ratio for making a stable aqueous, mixed micelle

system for self-assembly is 3:1 and 1:1 for TX-100 and P123, respectively. According to our results, this high volume of surfactant can cause potential degradation to the capacitance and the performance of the final device. Therefore, to achieve optimal performance, the amount of surfactant, especially TX-100 needs to be reduced. In this sense, P123 is more promising since its optimal performance is very close to the processing requirement

However, unlike organic solvent-based diluents, the increased viscosity of IL/non-ionic surfactant mixtures decreases the ionic conductivity down to ~1 mS/cm at room temperature at the highest surfactant loading studies (40 wt.%). While still high enough for many applications, it suggests that the enhanced capacitance induced by the surfactant will be offset by poorer performance at current densities. Furthermore, the addition of surfactant adversely influenced the electrochemical stability windows of EMImTFSI, reducing it from 4.5 to 3.5 V through a reduced oxidation stability which should be noted in device fabrication using these electrolyte series which will require more stringent limits on the positive electrode potential. Despite P123 and Triton X-100 exhibiting the same dependence of concentration on the ionic conductivity, P123 was found to be much more viscous at high concentrations causing a more significant deviation from the behavior that would be expected if the electrolyte followed Stokes-Einstein behavior. We investigated this further using pulsed field gradient nuclear magnetic resonance measurements from which we could extract the self-diffusivities of both cations and anions of EMImTFSI in the various mixtures. The resulting estimated conductivities were similar to those estimated by EIS. From this data, the effective Stokes radius was calculated, which showed that increasing the concentration of surfactant causes a smaller effective ion size. This suggests that both surfactants and, in particular, P123, reduce interactions between the ions which now diffuse more as naked ions rather than as a complex. A closer look at the polarity of both surfactants suggests that P123 is more polar that TX-100, leading to a larger reduction in ion-ion interaction, and solvation which could potentially lead to higher diffusion

coefficient. Nevertheless, the high viscosity of P123, due to its large MW, offsets this effect causing a reduction of the cation/anion diffusivity and the resulting conductivities. Choosing a surfactant with a higher polarity and lower MW can possibly improve both the rate performance and the capacitance.

Chapter 5

Supercapacitor Electrodes Fabricated using IL/P123 Mixed Electrolyte Spacer

In the following project, based on the findings of chapters 4 and 5, I used P123 as a self-assembly vehicle for IL to fabricate symmetric supercapacitor with rGO/P123/IL composite electrode. By varying the concentration of P123 (from 10 wt. % to 80 wt.%), and the ratio of IL/P123 (to 1, 2 and 3), several dispersions of rGO/P123/IL were prepared and flash freeze dried to yield composite powders which were pressed onto current collectors. The concentration of rGO in all dispersions was kept at 0.2 mg/ml to yield maximum adsorption. Overall, the gravimetric capacitance of the electrodes increased linearly with an increase in the total added spacer mass (IL + P123). Higher adsorptions of IL/P123 complex were observed at IL/P123 of 1 and 2. The electrodes with 60 wt.% P123 at IL/P123 = 3 resulted in the highest C_G = 247.3 F/g. The ρ_B of the electrode decreased as the total mass of spacer increased giving rise to $\rho_B \sim 0.18$ g/cm^3 compared to the calculated theoretical values of 1.5 g/cm^3, amounting to ~ 70% porosity. This porosity is found to be resulted from several air gaps which was trapped during the pressing process and reduced the C_V to 45 F/cm^3 from 365 F/cm^3 based on theoretical bulk density ($\rho_{theo.}$) The 20 wt. % P123 with IL/P123 =2 electrodes showed higher ρ_B of 0.54 g/cm^3 but lower C_G of 158 F/g resulting in the highest C_V of 80 g/cm^3 among the series. The rate performance of these two electrodes were comparable and showed 55 % reduction in charge transfer resistance compared to the rGO control electrodes. The volumetric energy density and power density of 20 wt.% P123 (IL/P123= 2) electrode were 27 Wh/L and 0.44 kW/L, respectively. While for 60 wt.% P123 (IL/P123=3), these values were reduced to 10 Wh/L and 0.11 kW/L. The areal capacitance vs. mass loading for 20 wt.% P123 (IL/P123=2) show linear increase up to mass loading of 1.58 mg/cm^2 which implies good ionic and electronic transport properties, nevertheless, the rate performance suffers at high loading which can be as a result of hindered electronic and ionic transport. The

presence of large porosity can also contribute to loss of electronic and ionic conductivity as the percolation network gets interrupted by the presence of pores and gaps.

For this project, I designed the experiments in consultation with Dr. Pope and all experiments were entirely conducted by myself. I also wrote the manuscript and Dr. Pope and Dr. Pal helped with editing of the manuscript.

This project was funded by NSERC discovery grant.

5.1 Introduction

Several techniques have been proposed so far for improving the SSA of rGO such as using a physical spacer, [11,14,212] chemical activation, [112,113] creating crumpled or curved rGO,[109,110] and using the electrolyte as spacer.[23,105,106,108,213] Among these methods, electrolyte mediated electrode fabrication has shown significant promise enabling some of the highest reported C_V since it can deliver a high ρ_B but often impose processing challenges. [23] To overcome this limitation, Pope et al. [105] used evaporative consolidation to create a gel mixture of GO and hydrophilic IL (1-Ethyl-3-methylimidazolium tetrafluoroborate) which was later heat treated to reduce the GO. This method provided a high C_G of 140 F/g but yielded a mediocre C_V of 65 F/cm^3 since the IL does not adsorb directly on the surface of GO resulting in inhomogeneous distribution of electrolyte and lower ρ_B of 0.46 g/cm^3.

We have shown in Chapters 3 and 4 that mixing several non-ionic surfactants such as Triton X-100 and Pluronic P123 can, in addition to imparting surface activity to a non-surface active IL,[123,172] have a beneficial effect on the C_{DL} measured at a glassy carbon working electrode. The C_{DL} of the IL/glassy carbon interface can surprisingly increase upon the addition of surfactant (for example, over 100% improvement is observed at 40 wt.% P123)[172] as a result of the reduction in ionic correlations within the IL by PEO chain of the non-ionic surfactants.[183]

These works motivated us to explore how the P123 surfactant system, which is known to be a good dispersant for rGO, might be leveraged alone or complexed with the IL EMImTFSI as a spacer requiring no additional processing steps after electrode casting onto an aluminum current collector. We show that using either P123 alone or various IL/P123 compositions leads to composite electrodes with a continuously tunable gravimetric capacitance which simply depends on how much spacer material is added to the composite. Composites exhibiting maximal gravimetric and volumetric capacitance are evaluated and demonstrate promising performance as high voltage, symmetric supercapacitors.

5.2 Experimental Method

Preparation of GO

The preparation of graphene oxide was performed as described in Chapter 3.

Preparation of reduced graphene oxide (rGO)

The graphene oxide was chemically reduced using hydrazine reduction method by Stankovich et al.[84] To a round bottom flask, 50 ml of 2 mg/ml GO dispersion in water was added and 200 µl hydrazine hydrate (35 wt. %) was added to the dispersion (based on the ratio hydrazine : GO of 7:10 wt./wt. as described by Li et al.).[98] This ratio was found to effectively remove 99% of the oxygen functional groups.[214] The dispersion was left overnight at 98 °C. The color of the initially yellowish gold GO dispersion turned black. The resulting rGO was then filtered and washed with 500 ml of DI water. The filter cake was collected (care was taken not to let the filter cake dry out which can lead to irreversible aggregation and restacking) and was subsequently used to make electrodes. Using this method, the GO was found to lose roughly 60 % of its original weight. To make this estimate, around 100 mg of GO was reduced using the above-mentioned method and then filtered and air-dried overnight. The resulting greyish black powder was placed in a vacuum oven (no heating) for two days to remove any remaining moisture and then was weighed. This procedure was repeated three times.

Preparation of rGO/P123/IL composite electrode

For preparation of the electrode, we added 5% of a commercially available reduced graphene oxide (Angstrom Materials Inc.) as a conductive additive which was mixed with the lab prepared rGO collected from the hydrazine reduction and added to an aqueous dispersion of P123 at a concentration of 0.2 mg/ml. The amount of P123 was varied to achieve 10 to 80 wt.% of P123 (on a dry basis) to the dispersion. The dispersion was ultrasonicated for 30 min at 60% amplitude using Sonics Vibra-cell. Then, EMImTFSI was added to the dispersion and ultrasonicated for another 30 min. The ratio of IL to P123 was varied between 1, 2 and 3. The final dispersion was sprayed into liquid nitrogen using a spray bottle to flash freeze the IL/surfactant adsorbed layer onto the surface of the rGO.[123] The resulting frozen slurry was collected and freeze dried to produce a composite a powder of mixed rGO/P123/IL. At lower concentration of P123 and IL, a flocculent powder was collected. However, with increasing the concentration of both P123 and IL, this powder further clumped together, giving rise to a paste like material at around 80 wt.% P123, as a result of excess polymer. This powder was pressed onto a carbon coated aluminum current collector (single carbon layer, Landt instruments) using a 1/2-inch pellet pressing die (MTI corp.) and force of 5 tons (metric) at different mass loadings.

Electrochemical characterization of two electrode cell using rGO/P123/IL composite electrodes

For the purpose of electrochemical characterization, symmetric two electrode cells were made by sandwiching a glass fiber separator soaked with 100 μl of EMImTFSI between two rGO/P123/IL composite electrodes in a stainless steel two-electrode split test cell (TMAX Battery Equipment). The cell assembly was performed in an argon-filled glovebox (less than 1 ppm O_2 and H_2O). The two electrode cells were characterized by CV, GCD and EIS using a Biologic SP-300. The single electrode gravimetric capacitance, C_G, was calculated based on GCD and CV using equations 1 and 2, respectively.

$$C_G = \frac{2.i}{m_{active}.(U-U_{drop})/\Delta t}$$ Equation 5-1

$$\boldsymbol{C_G = \frac{2I_{ave}}{m_{active}\nu}}$$ Equation 5-2

where *i* is the current set for the GCD test, m_{active} is the mass of active material on one electrode, *U i*s device operating voltage (3 V), U_{drop} is the voltage drop at the beginning of the discharge cycle and Δt corresponds to the time it takes for the cell to fully discharge. I_{ave} is the averaged current at the 1.5 V point on CV curve and *v* is the scan rate. And the C_V and areal capacitance (C_A) are calculated as:

$$\boldsymbol{C_V = \rho_B C_G}$$ Equation 5-3

$$\boldsymbol{C_A = \rho_A C_G}$$ Equation 5-4

The ρ_B was calculated by dividing the active electrode materials by the product of electrode's thickness and the area of the electrode. The electrode thicknesses were measured using a caliper. To counter the effect of minor surface irregularities, average of 4 readings from the surface was collected. The areal density (ρ_A) was calculated by dividing the mass of active electrode material by the area of electrode.

The volumetric energy density and power density were calculated using the following relations:

$$\boldsymbol{E_v = \frac{1}{8}\rho_B C_G U^2}$$ Equation 5-5

$$\boldsymbol{P_v = \frac{E_v}{\Delta t}}$$ Equation 5-6

where Δt is the discharge time.

Characterization

SEM images were taken on a field-emission scanning electron microscope (Zeiss UltraPlus) with an acceleration voltage of 10 kV. EDS (EDAX Apollo X) was performed on a thick pressed pellet of sample using acceleration voltage of 20 kV under 500x magnifications.

Electrical conductivity of reduced graphene oxide was measured using a four-point probe station (Ossila). The samples were made by grinding rGO in mortar and pestle and pressing them using hydraulic press into a 0.4 mm thick pellet.

FTIR of rGO and GO were performed using NEXUS 670. For GO, a thin film was created by drop casting and air-drying diluted GO dispersion on aluminum weighing boat, the free-standing GO film was then placed between two slits and subsequently placed into the sample holder for testing. The rGO samples were made by mixing rGO power with KBr 1:100 ratio (rGO to KBr) in mortar and pestle and then pressed in hydraulic press into a thin disc - Since rGO is in powder form, making a thin film using this material is unfeasible, therefore, we decided to use KBr pellet, whenever possible pure form of material was used as sample for FTIR such as in GO case. Using 32 number of scans and resolution of 4 in IR transmittance mode, the data were collected in the range of 4000-400 cm^{-1} wavenumber. The Aperture was set at 32 and optical velocity at 0.63.

Fluorescence spectroscopy was performed for characterization of IL adsorption using a Varian Carry Eclipse and Rh B dye with an excitation wavelength of 550 nm. The resulting emission was collected between 560-600 nm. The adsorption study was performed using a method reported in Chapter 3. Shortly, EMImTFSI was labeled using Rh B dye and was added to the aqueous dispersion of P123 (C_{P123} = 0.4 mg/ml) using ultrasonication to make different weight ratio of P123/IL=1, 2, and 3. The emission spectra were collected for the resulting dispersions and set as control. A fixed amount of rGO was added to the P123 dispersions to make the concentration of 0.2 mg/ml and sonicated for 30 minutes, IL/Rh B at different

ratios (IL/P123 = 1, 2 and 3) was added and sonicated for another 30 min. The final dispersion was centrifuged using Eppendorf centrifuge 5424 at 15000 rpm for 10 min and the supernatant was tested under the same excitation as control samples and the emission spectra were collected and compared with that of the control samples for each IL/P123 ratio. For each IL/P123 ratio, the sensitivity of the device was set to max out the signal from control emission wavelength, for better visual contrast, and the subsequent supernatant spectra were collected using the same device sensitivity. For the adsorption isotherm study, the same procedure was applied with 0.1 mg/ml rGO and fixed IL/P123 ratio of 1.

XRD was performed using a MiniFlex II unit (Rigaku Americas, Cu Kα radiation) from 2θ = 6 to 50° using samples width of 0.05° and scan speed of 1°/min. For testing GO, the aqueous GO was drop cast onto a glass slide and air dried. It was then used directly for testing, and for rGO, a thick pellet was made and placed on the sample holder for testing. Care was taken to match the thickness of the pellet with the depth of the cavity of sample holder to avoid shifting the diffraction angles.

DLS was performed using Zetasizer nano 90, Malvern. Samples were prepared by first dispersing the surfactant in water and then adding a fixed amount of EMImTFSI and further dispersion by ultrasonication. The final dispersion was filtered using a syringe filter with 0.2 μm pore size.

5.3 Results and Discussion

Characterization of IL/P123 aqueous dispersions:

Figure 5-1a shows different volumes of EMImTFSI, a hydrophobic IL (labeled with Rh B to provide visual contrast), in water and Figure 5-1b shows the same concentration of IL when 0.4 mg/ml P123 is added to the mixture (all the three vials have 0.4 mg/ml of P123). As depicted in Figure 5-1b, after addition of P123, the IL disperses in water, resulting in the formation of a transparent solution for tested ratios of IL/P123. The transparency indicates that the dispersed phase is significantly smaller in size than the wavelength of visible light (<< 400 nm). These result, however, are taken at the concentrations lower than

the cmc of P123 (C_{P123} = 0.4 mg/ml vs. C_{CMC} = 1.70 mg/ml). In order to analyze the interaction in the presence of micelles, we performed DLS analysis at a higher concentration of P123 (i.e., C_{P123} = 4 mg/ml) and IL (This is done to increase the total kcps to ~100 which is often needed for a reliable result). For IL/P123 ratio of 1 and 2, a transparent dispersion was resulted. However, we noticed when the ratio of IL to P123 reaches 3, the dispersion changes from transparent to cloudy. Figure 5-1c shows DLS analysis of the dispersions when different ratio of IL/P123 existed in the solution. According to this result, for IL/P123 of 1 and 2, a uniform dispersion with droplet sizes ~10 nm is formed, which is close to the value reported for aqueous micelles of P123, [215] implying the formation of mixed micelle with IL. However, with the IL/P123 = 3, the droplet sizes follow a bimodal distribution, where the average sizes of the smaller droplets is ~20 nm with the appearance of a larger droplets showing particle sizes of ~200 nm (equal to the maximum pore size of the filter paper). From the above results, it can be inferred that addition of excess amount of IL results in swelling of the micelles up to a certain level above which unstable agglomerates with larger diameters appear. Such behavior has been observed in the literature for Pluronic and imidazolium-based ILs. [216] However, this is not the case for C_{P123} = 0.4 mg/ml. It should be noted that EMImTFSI is slightly soluble in water, therefore, at lower concentrations of the surfactant shown in Figure 5-1b, a sizeable amount of the added IL can be solubilized in water without the aid of the surfactant, therefore, the surfactant will only solubilize a portion of the added IL, while the rest will be dissolved in water. As it was already mentioned in the method section, the 0.4 mg/ml P123 (i.e., 80 wt. % P123 based on dry mass of rGO) was the highest concentration of surfactant used in electrode making process. Therefore, we can safely say that before adding rGO, all of our dispersions form stable solution in water

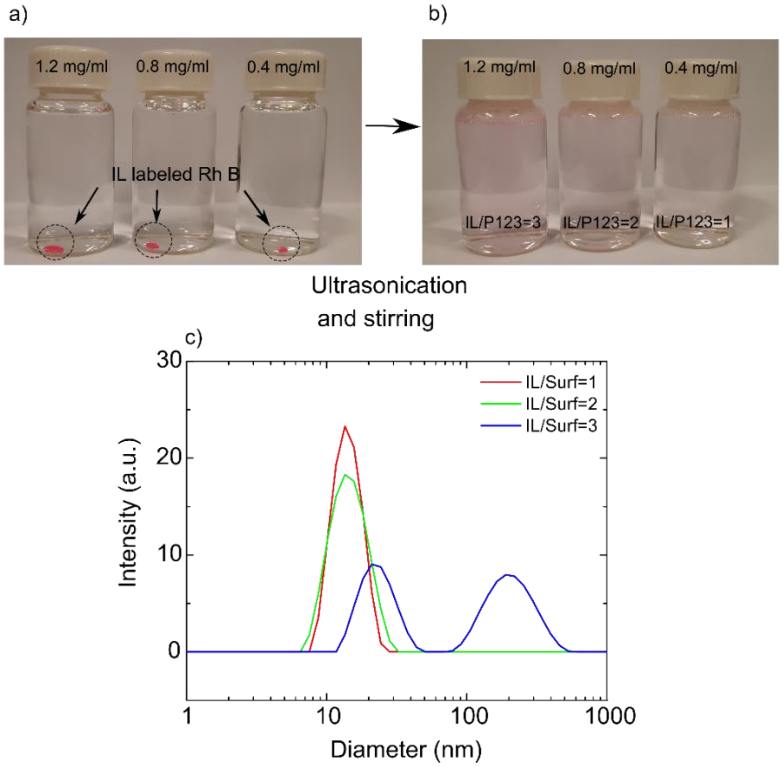

Figure 5-1: Characterization of microemulsion, a) Rh B labeled EMImTFSI in water at various concentration of IL, b) Rh B labeled EMImTFSI dispersed in water after addition of 0.4 mg/ml of P123, c) DLS of microemulsions of EMImTFSI/P123 in water at different weight ratio of IL/P123 at 4 mg/ml of P123

Characterization of IL adsorption on rGO:

Figure 5-2 shows the adsorption isotherm of IL/P123 (mass ratio of 1) complex on rGO (0.1 mg/ml). As it can be seen, with increasing the concentration of IL (C_e), the adsorption increases following the Freundlich adsorption isotherm ($q_e = KC^{1/n}$) with R^2 value of 0.98, K = 37.5 and n = 1.36. Since Freundlich adsorption isotherm is entirely empirical, not much information can be derived from this isotherm, nevertheless, it is often observed for adsorption on heterogeneous surfaces. [217] From the adsorption isotherm, the adsorbed amount increases with increasing the concentration of adsorbate.

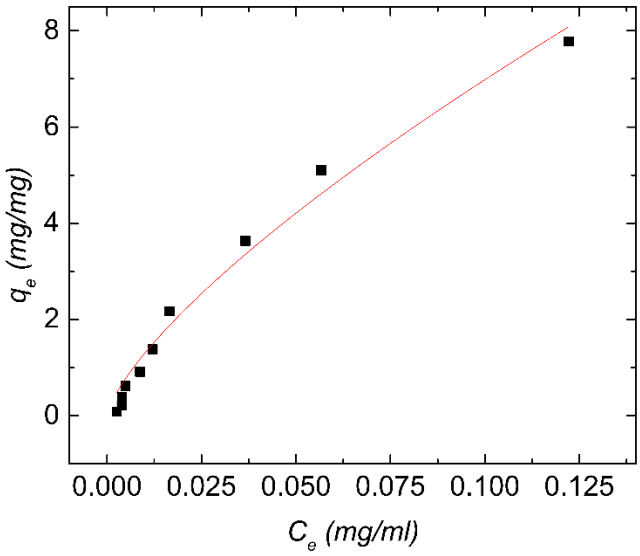

Figure 5-2: Adsorption on P123/IL complex on rGO (0.1 mg/ml) using Rh B dye as label for IL (IL/P123=1), Freundlich adsorption isotherm

Next, we tried to study the adsorption of IL/P123 complex at higher concentration of rGO (0.2 mg/ml) since it is more feasible in terms of our experimental set up. We performed this test at 60 wt.% P123 which generates the C_{P123} = 0.4 mg/ml and we changed the IL/P123 ratio to 1, 2, and 3. The adsorption of IL onto rGO surface was verified using fluorescence spectroscopy as shown in Figure 5-3. When the Rh-B labelled IL is added to the rGO/P123 dispersion, the dark colored dispersion remains stable (Figure 5-3a) but can be separated from the supernatant by centrifugation (Figure 5-3c). The fluorescence spectra of control IL/P123=1 (no rGO) and supernatant of the same samples after adsorption onto rGO (unabsorbed IL/Rh B/P123 complex) is depicted in Figure 5-3b. The significant drop in the intensities suggests that most of the IL is bound to the rGO with only a small amount remaining in the dispersions. From the depleted IL, an adsorbed amount can be compared to total amount in solution as shown in Figure 5-3d. These amounts are larger than the adsorbed amounts that we previously reported for similar IL/non-ionic surfactant (Tween 20 and Triton X-100) systems adsorbed to GO prior to reduction (i.e., Q_{max} ~ 1-3 mg IL/mg under depending on concentration).[123] According to studies performed on the adsorption of Pluronic (P123 and F127) on GO

surfaces, these two surfactants interact with hydrophobic section of GO using their PPO chain. [218,219] Since, rGO is expected to have a larger proportion of more hydrophobic graphene domains compared to GO, it is able to more efficiently adsorb the surfactant, and therefore, the mixed adsorbate (IL/P123 complex).

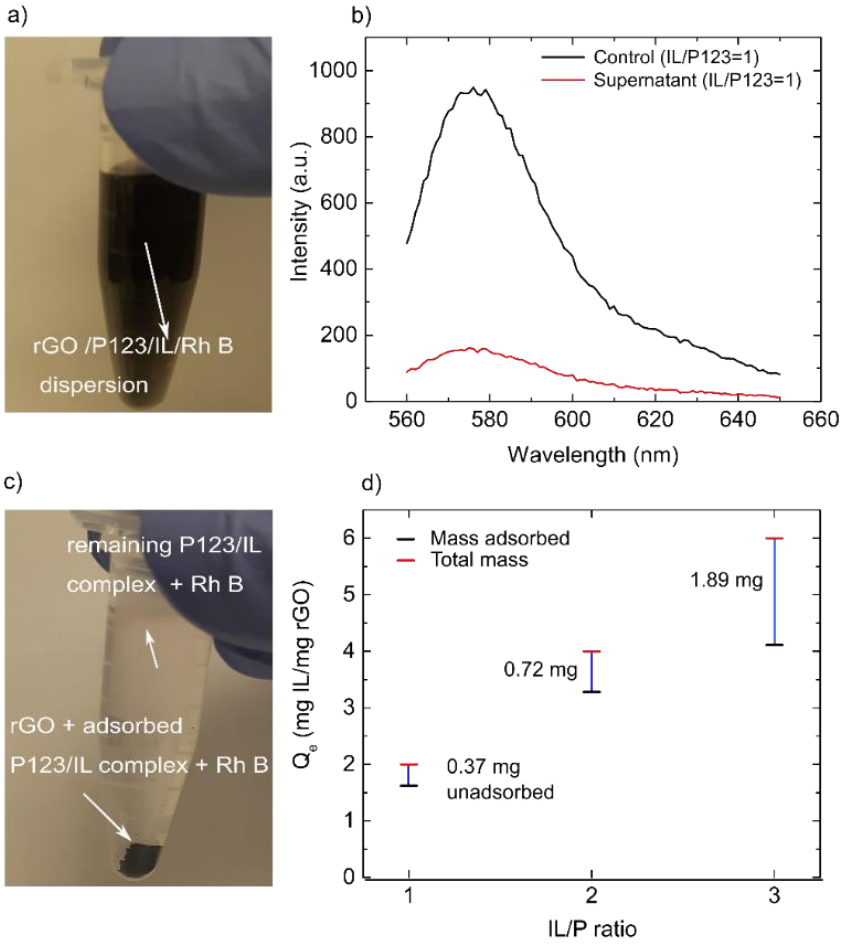

Figure 5-3: Characterization of adsorption P123/IL complex on rGO: a) Photograph of dispersion of rGO/P123/IL; b) Comparison of the emission spectra from supernatant dispersion and control dispersion (i.e., without rGO) for IL/P123 = 1, c) Photograph of rGO pellet with adsorbed P123/IL complex; d) Adsorbed amount in comparison with total IL mass added for each IL/P123 ratio on rGO. The difference is the mass of unabsorbed.

As it was discussed earlier, the concentration of surfactant in all our dispersions is below the cmc of P123, based on this, we expect the surfactant molecules to be dissolved as discrete monomers in the bulk solution which are in equilibrium with an adsorbed phase. As we add IL, interactions between IL molecules and surfactant leads to delivery of IL to the surface. These interactions have been observed between imidazolium protons and PEO chain of Pluronic triblock copolymers. However, PPO chains remained intact as the ether oxygen in PPO is shielded by methyl groups.[220,221] In addition, P123 was reported to break the cation-anion interactions in imidazolium ILs by forming stable cation/P123 and anion/P123 interactions.[221] Therefore, one likely explanation is that IL molecules are being delivered to the rGO surface by complexation with the PEO chains of P123 while PPO groups bond to the rGO surface using hydrophobic interactions. [218,219] A schematic of possible hydrogen bonding between the PEO chain of P123 and EMIm and TFSI is shown in Figure 5-4.

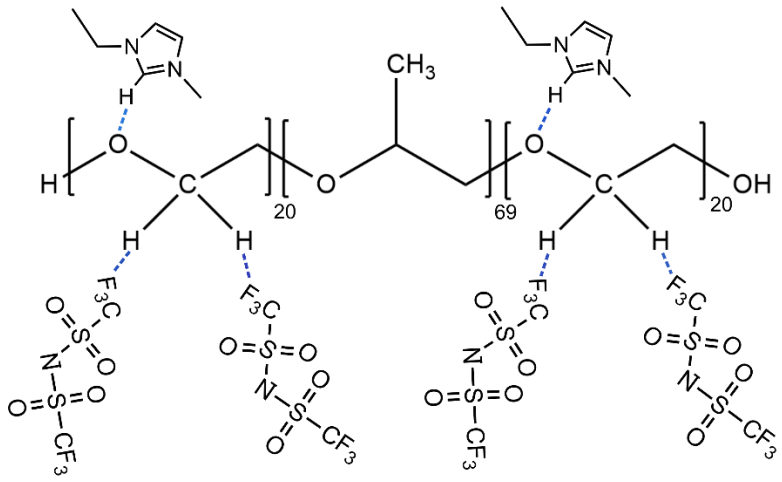

Figure 5-4: Possible interaction of EMImTFSI with P123 surfactant, the dashed blue lines are hydrogen bonding between hydrogen atom of PEO and F in TFSI and oxygen atom in PEO and C2-H in EMIm

From Figure 5-3d, the percentage of unabsorbed molecules are 18%, 18%, and 31% for IL/P123 ratio of 1, 2 and 3, respectively. Therefore, when we have up to two times IL to P123 in the dispersions, we get a higher adsorption, implying that each surfactant can deliver two IL molecules to the surface. Interestingly, when studying these colloidal dispersions at concentration above the cmc, we saw similar trend that P123 is able to complex with IL forming mixed micelles for IL/P123 mass ratio of 2 or less (Figure 5-1c).

Characterization of GO and rGO

The as prepared GO exhibits a C/O ratio of 1.43 ± 0.02 (by atomic ratio) which is increased to 10.3 ± 0.2 after hydrazine reduction in line with similar values reported in the literature.[84] The conductivity of the rGO was found to be around 400 S/m and also similar to previous reports. [84] In order to make a comparison between the functional groups present in both GO and rGO, their spectra were compared using FTIR. Figure 5-5a shows spectra of GO (black) and rGO (red). In this spectrum, the O-H stretching of free hydroxyl groups absorb in the 3620 cm^{-1} (3700-3584 cm^{-1}). The O-H stretching vibration of water molecule can be found at a lower frequency of 3420 cm^{-1} (3550-3200 cm^{-1}). The C-O stretching vibrations are found at 1260-1000 cm^{-1}. The peak at 1050 cm^{-1} can be assigned to epoxy group (C-O-C), while the peak at 1220 cm^{-1} can be allocated to hydroxyl groups (C-OH). The C=C stretching is observed at 1629 cm^{-1} and finally, the carbonyl and carboxylic group (C=O) appears at around 1735 cm^{-1} (1740-1720 cm^{-1}). [164]

The rGO spectrum shows two distinguished bands near1220 cm^{-1} and 1570 cm^{-1} which can be assigned to C-OH groups [214] and C=C stretching absorption band,[222] respectively. By comparison of these two spectra, considerable amounts of functional groups such as carbonyl, carboxyl and epoxy have been eliminated using the hydrazine reduction method and the amount of sp^2 hybridized carbon has been enhanced causing the material to transition from electrically insulating to electronically conducting.

Figure 5-5b shows the XRD profiles for both GO and rGO. For GO, a sharp peak at 10.5° originating from the 001 plane, corresponds to an average interlayer spacing of ~0.84 nm due to presence of oxygen containing functional groups. In contrast, in the rGO spectrum, the peak at 10.5° is replaced with a broad peak at around 24 ° (002 plane). This shift is due to the reduction in interlayer spacing to 0.37 nm as a result of losing the functional groups and restacking of the rGO sheets to a spacing closer to that of graphite (0.34 nm).

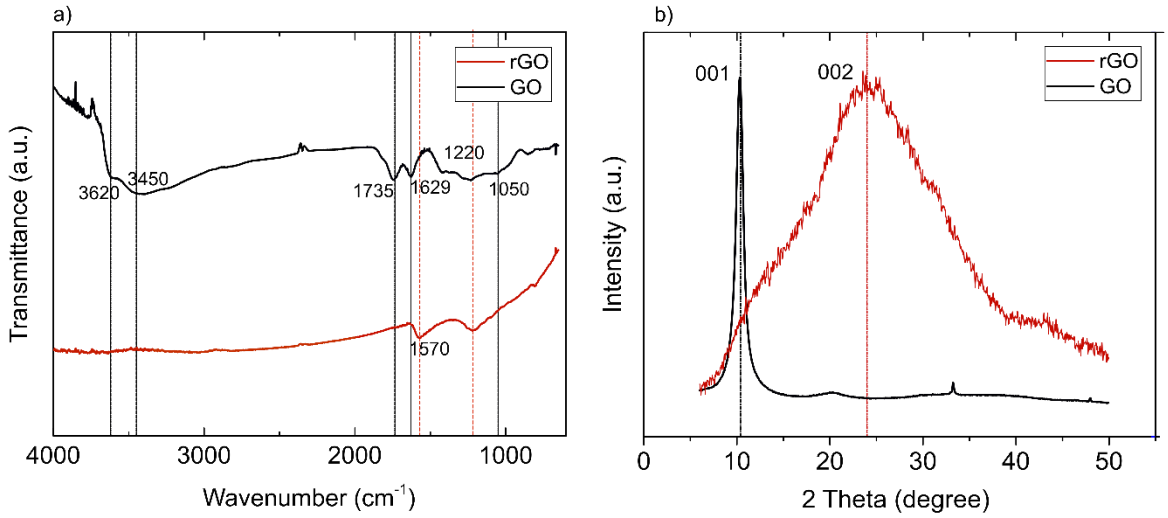

Figure 5-5:Characterization of rGO (black) and GO (red), a) XRD spectra, b) FTIR spectra (red)

Morphological comparison of flash freeze dried rGO and air-dried rGO

Flash freeze drying has proven to provide higher surface area compared to air drying method. During air drying process, as the water evaporates, it induces capillary forces on the sheets, which consolidates the rGO, causing them lose their surface area, while in flash freeze drying process, water sublimes as the sheets are frozen in place, preserving much of its surface area while it is being dried. Figure 5-6a compares the volume of the two materials with the same mass (~6 mg). The freeze-dried sample has a larger volume as a result of enhanced surface area. Figure 5-6b and c show the SEM images of rGO for both freeze dried and air dried rGO, the freeze dried rGO consists of individual rGO sheet that are curved and wrinkled, however,

evaporatively dried samples show clumps of rGO while the individual sheets are unidentifiable. Freeze drying of rGO therefore, provide a significantly reduced ρ_B, which is expected to lead to a higher surface area [223] compared to that of air dried rGO. [10,11]

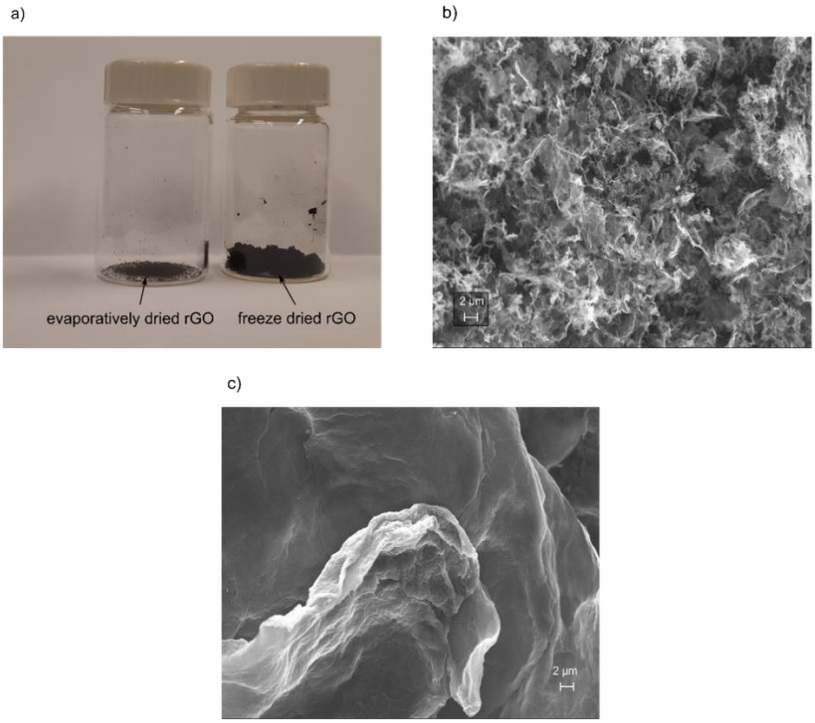

Figure 5-6: Comparison of morphology and surface area of air dried and flash freeze dried rGO, a) Comparison of the volume of 6 mg of the materials for air dried rGO (leftmost vial), and flash freeze dried rGO (rightmost vial), b) SEM image of flash freeze dried rGO, c) SEM image of air dried rGO

Electrochemical performance of rGO/P123/IL composite electrodes

The gravimetric capacitance of a series of electrodes prepared by spray-freeze drying various rGO/IL/surfactant mixtures is shown in Figure 5-7. Figure 5-7a, compares the capacitance of air dried rGO, spray-freeze dried rGO, spray-freeze dried rGO/P123 and spray-freeze dried rGO/P123/IL composites. Allowing the rGO to aggregate and consolidate under capillary forces in the air-dried case leads to electrodes that exhibit only 62.8 F/g of capacitance. Minimizing this aggregation by spray-freeze drying

and switching from capillary induced densification to mechanical densification leads to higher surface area electrodes exhibiting a capacitance of 95.4 F/g which is ~51 % enhancement.

Incorporating P123 into the dispersion improved the capacitance further to 168 F/g (an additional 76% improvement), while, using IL/P123 surfactant complex boosted the capacitance an additional 45% to 243.7 F/g. These results demonstrate the severe sensitivity of graphene or rGO ion-accessible surface area on processing conditions with each material being the same rGO but just assembled in a different way. Adding the P123 or IL/P123 complex as a spacer provides a significant boost in capacitance while retaining a pseudo-rectangular CVs up to 3 V.

In Figure 5-7b, we study the effect of P123 wt.% on the achievable capacitance by galvanostatic charge-discharge testing. However, since P123 is not ionically conducting, the test cell was assembled under flooded IL conditions and mutual diffusion of P123 and IL are expected to have taken place due to the concentration gradient [224] which is expected to draw IL into the initially P123-filled pores of the rGO/P123 composite (this will be discussed more in the upcoming sections). It is interesting to note the maximum capacitance for 10 wt.% P123 electrode series occurs as IL/P123 = 1, while for the 20 wt. % P123 series, the maximum gravimetric capacitance of 158 F/g was reached at IL/P123=2 (or 20 % P (2)), and adding extra IL resulted in a drop in capacitance. Similar phenomena can be observed for 40 wt. % P123 series. However, for 60 wt.% P123 series, the maximum capacitance occurs at the IL/P123=3 (or 60 % P (3)) which is also the largest capacitance among all the tested series (C_G = 243.7 F/g). One likely explanation to this behavior is the possible effect of free, dissolved or emulsified IL on the self-assembly of IL/P123 and kinetics of adsorption.[225,226] Therefore, certain ratios of IL/P123, at various concentrations of surfactant, result in more uniform coverage of the surface, as it was shown that this uniform coverage is critical to achieving large capacitance.[106] For 80 wt.% P123, addition of IL made the rheological properties

of the powder unsuitable for pressing into a semi-solid electrode disc. Therefore, we have not reported any values for this electrode as it could not be easily cast onto a current collector for capacitance measurements.

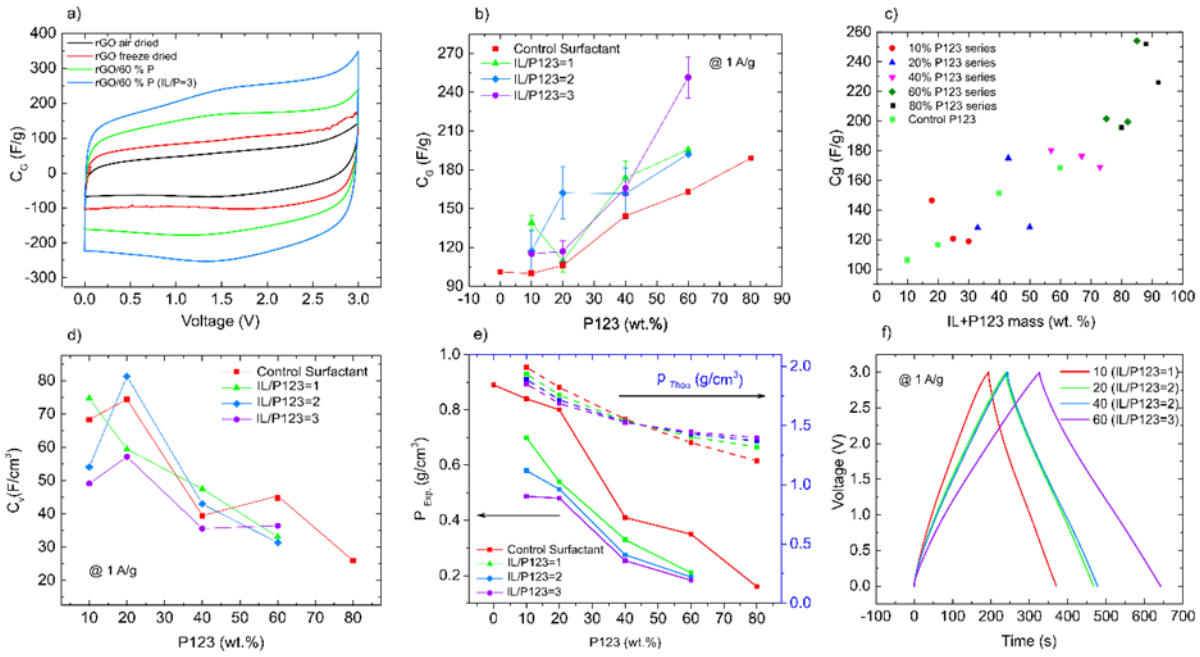

Figure 5-7: Electrochemical performance of rGO/P123/IL composite electrodes at different concentrations of surfactant and IL, electrode loading 0.79 mg/cm^2, a) CV of rGO control (freeze dried and air dried), rGO/P123(at 60 wt.%P123) and rGO/P112/IL (at 60 wt.% P123 (IL/P=3), scan rate = 5 mV/s, b) C_G of electrodes vs. surfactant wt.% at 1 A/g, c) C_G of electrodes vs. total added spacer mass %, d) C_V of electrodes vs. surfactant wt.% at 1 A/g, c) Density comparison of the electrodes, $\boldsymbol{\rho_{theo}}$ denotes the calculated theoretical density (using $\boldsymbol{\rho_B}$ of 2.2 g/cm^3 for graphene) vs. measured $\boldsymbol{\rho_B}$, d) GCD comparison of best performing electrodes at 1 A/g.

However, regardless of the peculiar behavior of C_G with respect to IL/P123 ratio, considering the total mass added to the composites, the capacitance is continuously increasing (Figure 5-7c) in a nearly linear fashion with the total mass spacer material used, suggesting synergic effect of both P123 and IL as spacer. Nevertheless, increasing the amount of spacer has an adverse effect on the C_V of our electrodes as less of the electrode volume is active material with a larger proportion being spacer (Figure 5-7d). Figure 5-7d compares the volumetric capacitance of the whole series of composite electrodes. The maximum C_V is 80

F/cm^3 and occurs at 20% P (2) with C_G of 158 F/g. The second-best performance in terms of C_V can be assigned to 10 % P (1) electrodes with volumetric capacitance of 75 F/cm^3. However, for 60% P (3) electrodes with the highest C_G, the C_V drops to 45 F/cm^3. This drop is due to decrease in electrode density as a result of air entrapment during electrode processing which creates voids in the film. Furthermore, the wrinkled structure of freeze dried rGO (as depicted in Figure 5-6) also reduces the density of the electrodes where the sheets are not as aligned as those deposited by something like vacuum filtration. [23] Figure 5-7e compared the experimental vs. calculated theoretical density of the composite electrodes. For 60% P (3) electrode, the calculated density is ~1.4 g/cm^3 which can boost the CV further to 350 F/cm^3. The presence of trapped air will be illustrated in the upcoming section.

For the best performing electrode of each series, their GCD curves were compared in Figure 5-7f at 1 A/g. The GCD curves are nearly triangular in shape with only a slight voltage drop at the beginning of the discharge cycle (~0.05 V). This can be ascribed to the purely double layer charging of these composites electrodes as a result of effective reduction of GO which was observed in Figure 5-5b. Our previous attempt using heat treatment of the electrode at low temperature of 300 °C resulted in partial removal of the oxygen containing functional groups which can further contribute to the pseudocapacitance and degradation of the device cycle-life. [106]

As it was discussed earlier, for our rGO/P123 electrodes (control surfactant) and some of our composite rGO/IL/P123 electrodes, during the first few CV cycles (work-in cycles), due to mutual diffusion of IL and P123, IL was drawn into the electrodes pore. This time-dependent process was observed as the capacitance of the cell (area of the CV plot) increased from first cycle to the last cycle (10th), indicating that more rGO surface area became ion-accessible with time (Figure 5-8a). While this worked to improve the capacitance, instead, including the IL with the P123 as part of the adsorbed layer complex had a stronger effect on boosting capacitive performance (Figure 5-7b) while the electrolyte work-in cycles were found unnecessary

(Figure 5-8b) indicating that there was already enough IL in the composite to sustain ionic contact to all rGO surface area. Nevertheless, this work-in cycle was observed for 20% P (2) electrode, implying that the electrode surface still is not fully saturated with IL molecules (Figure 5-8c).

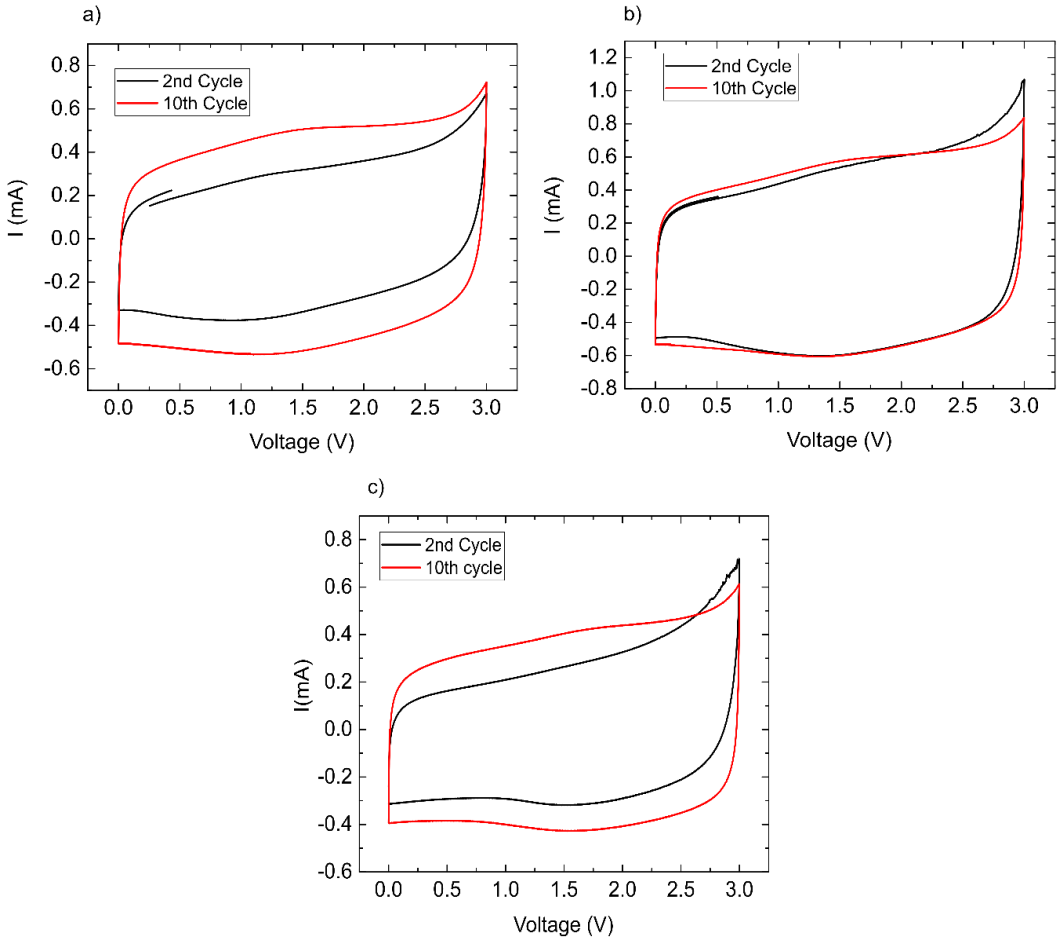

Figure 5-8: Comparison of the 1st to 10th cycle of CV at 5 mV/s, a) 60 % P Control (no IL), b) 60% P (3), c) 20% P (2)

Comparison of 60% P (3) and 20% P (2) electrode performances:

Since 20% P (2) and 60% P (3) electrodes showed the highest volumetric and gravimetric capacitance, respectively, we have compared their performance in this section. Figure 5-9a and b show the CV for 20% P (2) and 60% P (3) electrodes, respectively. The CVs for both electrodes are rectangular in shape and remain so up to a very large scan rate indicating ideal double layer charging. The capacitance vs current densities are compared for both electrodes in Figure 5-9c. As it can be seen from the plot, both electrodes show good rate performance, maintaining up to ~70% of their original capacitance up to current densities as high as 10 A/g. This is an indication of both good ionic and electronic conductivity due to the presence of IL/P123 between the rGO. In Figure 5-9d, voltage drops (IR drop) vs. current density show linear relationship (R^2 ~ 0.99 for both cells) for both electrodes, the slope of this line represents the equivalent series resistance (ESR), or internal resistance of the cell, [227] which reflects the combined resistances due to ion and electron transport. [228] The ESR values of 0.032 Ω and 0.029 Ω were measured for 20% P (2) and 60% P (3), respectively. Figure 5-9e shows the phase angle vs. frequency for both electrodes. As it can be seen from the plot, the phase angle for both electrodes is close to -90 (~ - 80°) at lower frequencies which again signifies ideal double layer capacitance behavior. The frequency at a phase angle of -45° marks the characteristic frequency f_0 where both capacitive and resistive impedances are equal.[229] This frequency for both of our electrodes is at 0.2 Hz corresponding to a time constant (τ_0) of 5 s. Figure 5-9f probes the ion transport properties of both electrodes using EIS. Overall, both electrodes show nearly ideal capacitive behavior judging from the vertical line at the low frequency region. The 45° line from 243 Hz to 1.04 Hz, which is seen for both electrodes, is a result of Warburg-like impedance caused by diffusion resistance as the electrolyte penetrates into the electrode's interior parts.[228] Regardless of the larger volume of IL in 60% P (3), both electrodes show the same Warburg impedance. However, as it was mentioned earlier, the 20% P (2) electrodes require initial work-in cycles using a low scan rate of 5 mV/s, while, the 60% P (3) did not

require this extra step (Figure 5-8b and c). The semicircle in the high frequency region which is sometimes referred to as the charge transfer resistance but for blocking electrodes are more related to the resistance associated with ionic and electronic diffusion processes in the porous electrode, are quite similar and low (~4 Ω).[228] These resistances were compared with control samples of 20% P and 60% P (surfactant only) and the rGO only electrode in Figure 5-10.

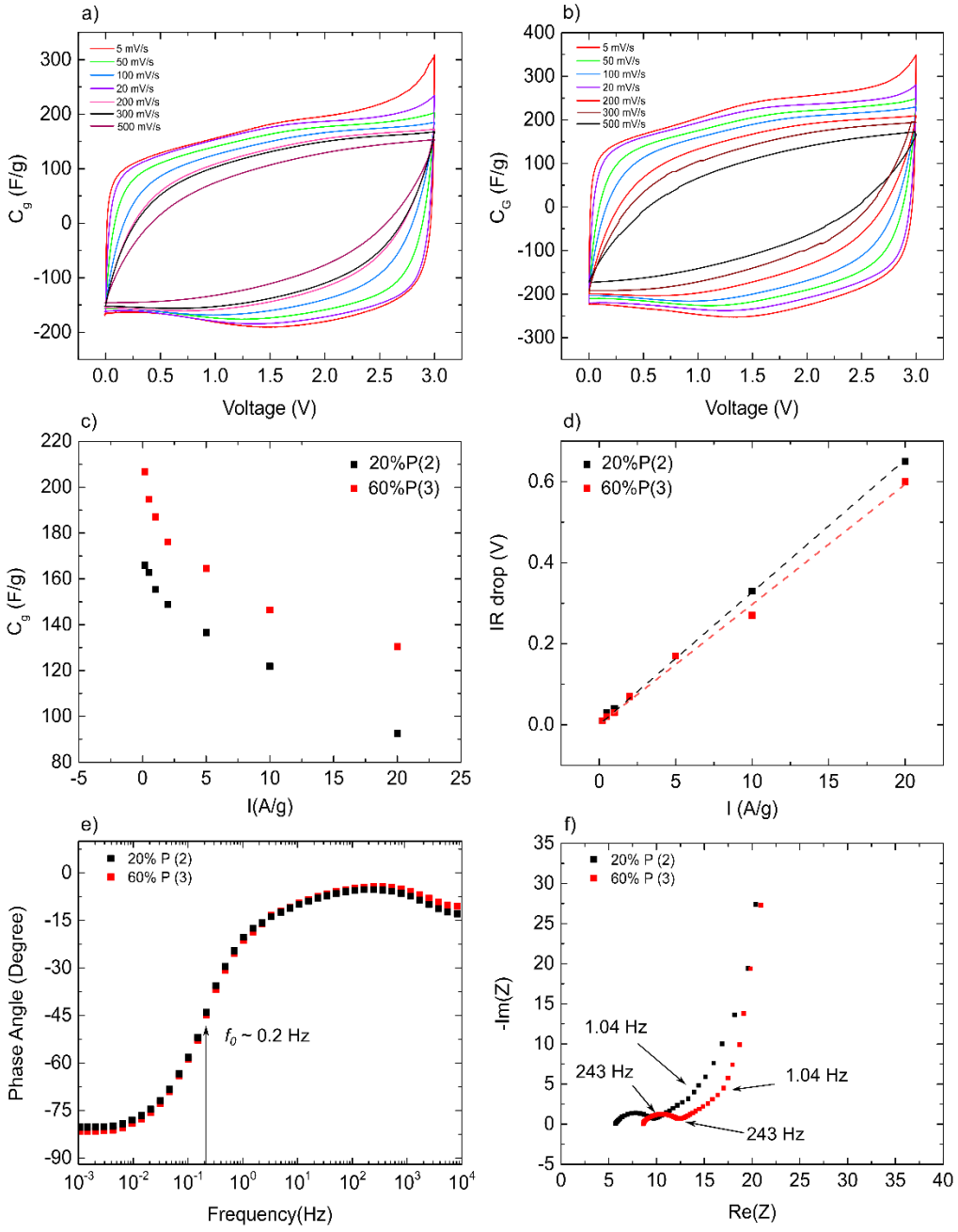

Figure 5-9: Comparison between performance of 60% P (3) vs. 20% P (2), a) CV of 20% P (2), b) CV of 60% P (3), c) Rate performance for 20%P(2) vs. 60% P (3), d) IR drop vs. current density comparison for 20% P (2) and 60% P (3), e) Phase angle for 20% P (2) and 60% P (3), f) EIS comparisons between 20% P (2) and 60% P (3)

As depicted in Figure 5-10a, rGO electrode has the largest voltage drop and ESR as a result. Adding 20 % of P123 has reduced the voltage drop to 0.29 V, but increasing the surfactant further has an adverse effect on the total cell resistance as it can be seen from the increased voltage drop (0.39 Ω). The control sample with rGO as electrode, show a fairly large charge transfer (~ 9.7 Ω) and Warburg resistance, while with addition of only 20 wt.% P123, this resistance reduces to 4.4 Ω. The reduction in resistance with only 20 wt.% P123 can be related to the enhanced ionic transport facilitated by surfactant spacers, which states the significant role of electrolyte in reducing the overall resistance of the cell. The Warburg resistance has also significantly reduced implying better ionic diffusion. With further increase in the amount of surfactant, resistance increase (~6.8 Ω) as a result of having excess non-conducting surfactants, also ionic transport will be interrupted by the surfactant molecules, in addition to hindered ionic diffusion as can be seen from enlarged Warburg resistance. Comparing this value with that of 60% P (3) electrodes, the effect of ordered self-assembly of IL/P123 on the interface prior to electrode assembly can be clearly identified and this effect has already been observed in capacitance enhancement of this electrode (Figure 5-7b).

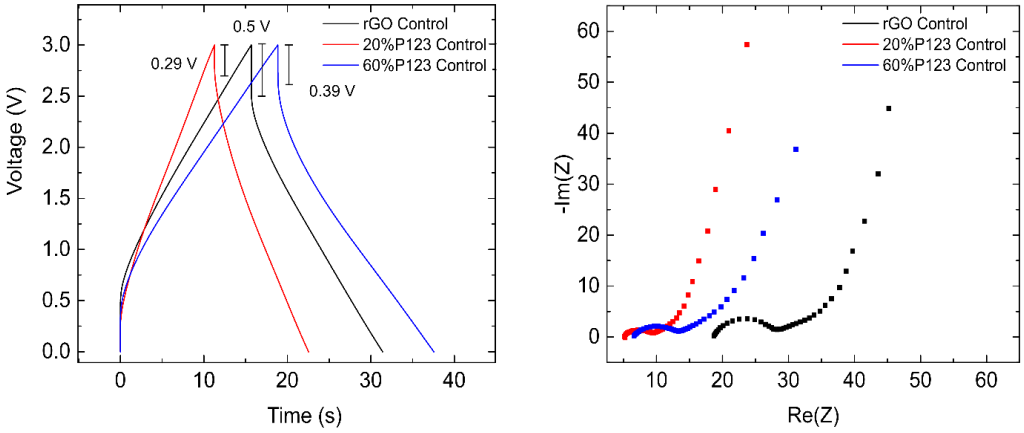

Figure 5-10: Comparison of the GCD and EIS for rGO, 20% P control and 60% P control electrodes, a) GCD comparisons at 10 A/g, b) EIS plot comparisons

Loading study for 20% P (2) electrode:

Since 20% P (2) has the highest volumetric energy density, we have studied its performance at different areal mass loadings of the electrode. Higher loadings are desired as they increase the practical device energy density by increasing the ratio of active material to inactive material (current collectors, membrane separator, etc.). By doubling the electrode loading to 1.58 mg/cm^2, the gravimetric capacitance stays the same for lower scan rates of 5 mV/s and 20 mV/s (20 mV/s corresponds to 1 A/g), but drops at higher scan rates losing ~ 60% of its original values at high scan rate of 500 mV/s. While at 3.96 mg/cm^2 loading of active materials, the capacitance drops to 107 F/g at low scan rate and further reduces to 10 F/g at 500 mV/s, losing around 90% of its original capacitance (Figure 5-11a). Figure 5-11b, compares the GCD curve for different loadings. While for both 0.79 and 1.58 mg/cm^2 of electrode loading the GCD stays rectangular with low voltage drop of 0.05 and 0.11 V, respectively, the 3.96 mg/cm^2 loading electrode shows a much higher voltage drop of 0.29 V which explains the poor rate performance of this electrode. The drop in capacitance at higher loading are usually the result of hindered ionic or electronic transport across the electrode cross section. The areal capacitance (C_A) of the electrodes, shown in Figure 5-11c, increases linearly with mass loading up to mass loading of 1.58 mg/cm^2. The linear increase in C_A indicates that the ionic diffusion is not the limiting factor for capacitive performance in our electrodes up to mass loading of 1.58 mg/cm^2 .[230] The drop in C_A at higher mass loading of 3.96 is as a result of hindered ionic and electronic transport properties. Therefore, the voltage drop at high mass loading is originated from both electronic and ionic transport. The insufficient electronic conductivity of the rGO in addition to the existence of large gaps within the electrode can interrupt the electronic percolation network resulting in poor electronic conductivity. The ionic conductivities at higher mass loading also drops as the IL cannot fully imbibe the entire thickness of the electrodes and the existence of air gap can break the ionic transport network resulting in poor rate performance and capacitance.

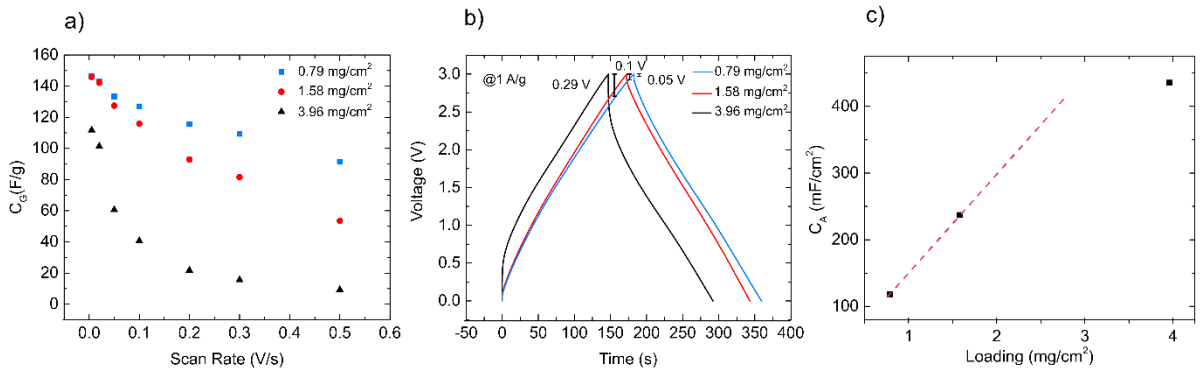

Figure 5-11: Performance of 20% P (2) with increased loading, a) rate performance of electrodes at different loading, b) GCD comparison of different loading at 1 A/g, c) Areal capacitance (C_A) for the max C_G (at 5 mV/s)

Morphological Characterization of 20% P (2) electrodes:

Figure 5-12 a and b show, the relatively smooth surface morphology of the 20% P (2) electrodes with some sparse irregularities related to rGO sheets emanating from the flat surface. This layered structure is better observed in cross sectional views in Figure 5-12 c and d. The carbon coating on the Al foil has ~1 µm thickness, separating the electrode material from the current collector. A slight gap can be seen between the carbon coating and the electrode materials as a result of poor adhesion. Therefore, improving the interface adhesion can further improve the interfacial resistance and rate performance of the device. Since our electrode materials have creases that can create air gaps, the carbon-carbon van der Waals forces between the electrode and the carbon coating layer can be interfered resulting in poor adhesion. In addition, areas with large air gap can be noticed throughout the electrode cross section (Figure 5-12c and d). These gaps are possibly air that is trapped while pressing the electrode/electrolyte composite using the hydraulic press. Using the expression for porosity, $P = 1 - {\rho_B}/{\rho_{theo.}}$, and the value of ρ_B and $\rho_{theo.}$ from Figure 5-7e, the porosity of 20% P (2) is estimated to be ~ 66%. This porosity is attributed to both electrode processing (using the hydraulic press) and wrinkled structures induced during the freeze-drying process.

Thereby by improving our processing, the electrode's ρ_B can be significantly improved. Nevertheless, the wrinkled structure of the electrode is unavoidable and its unlikely to achieve $\rho_{theo.}$ of 1.6 g/cm^3.

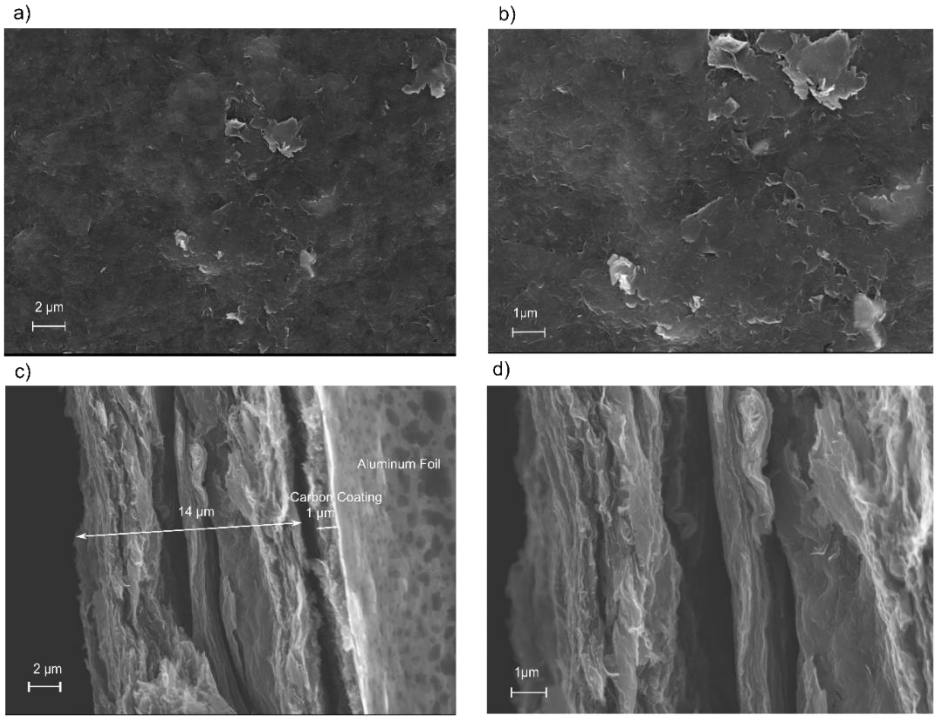

Figure 5-12: Morphological characterization of surface and cross sectional view of 20% P(2), a and b) Surface morphology, c and d) Cross sectional view of electrodes

The EDS mapping of the surface of 20% P (2) electrodes (Figure 5-13) shows uniform elemental distribution of O, N, S and F which indicates even distribution of IL throughout the electrode.

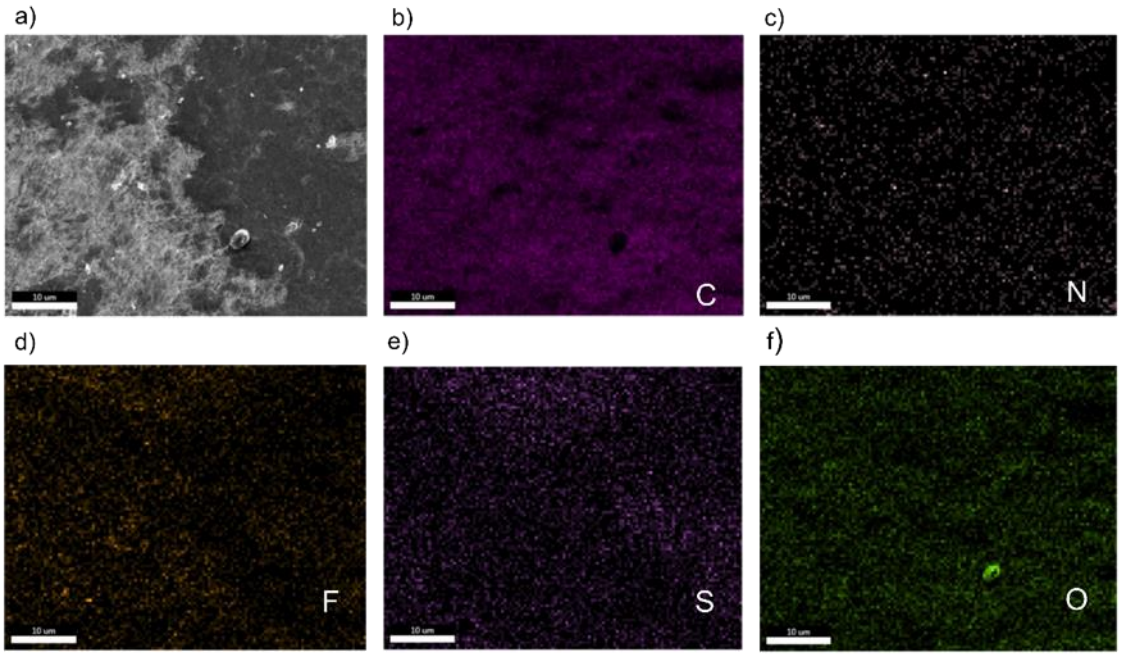

Figure 5-13: EDS mapping of 20% P (2) electrode surface, a) SEM image of the surface, b) composition of C element, b) composition of N element, d) composition of F element, e) composition of S element, f) composition of O element

Cycle life study and comparison of 20% P (2) electrodes to state-of-the-art:

The long term cyclability of our device with 20% P (2) electrode was tested using GCD at 10 A/g for 10,000 cycles. As depicted by Figure 5-14a, the capacitance of the 20% P (2) electrodes increase upon first 1700 cycles up to about 46 % of its original capacitance, as a result of work-in cycle associated with this electrode (Figure 5-8), and then reduce again at 5000 and 10,000 cycles but retaining around 94% and 80% of its maximum capacitance, respectively.

Table 5-1 compares other state-of-the-art EDLCs with our 20% P (2) electrode performance. Figure 5-14b shows a Ragon plot comparing the volumetric energy and power densities of our work to literature estimates. 20% P (2) electrodes show energy density and power density of 27 Wh/L and 0.44 kW/L, respectively when considering only the electrode volume. At a high-power density of 8 kW/L, the energy density drops to 16 Wh/L.

When comparing our work to the literature, it should be noted that, we have developed a procedure, which can be applied to any 2D material such as MXenes and carbides to create binder free electrodes, while maintaining high surface area between electrode and electrolyte using a scalable method which can be adopted at a manufacturing level. Since we have used hydrazine reduced graphene as an active material for our electrode, we first compare our work with Stroller et. al[10] which also used hydrazine reduced graphene as an active materials and PTFE as binder for electrodes combined with organic electrolyte to achieve volumetric energy density (E_V) of 10.7 Wh/L (Table 5-1). Using our procedure, we increased E_V to more than double the value reported for these materials indicating the importance of electrolyte spacer in improvement of the electrode's performance. Nevertheless, due to the nature of this reduction method, we still lose considerable surface area of rGO by hydrazine reduction due to instant agglomeration during reduction which cannot be avoided. Several works were reported using activation of graphene which resulted in improved surface area and energy densities (Figure 5-14b, marked by pink circle).[113,231–233] Nevertheless, these works all used binder which adds to the dead weight of electrode. Plus, both works using activated graphene (asMEGO and compressed a-MEGO) [113,231] used IL mixed with organic solvents at 1:1 wt. ratio which are flammable and toxic (Table 5-1). PGP electrodes also show high energy density as a result of compression but the rate performance is compromised. [233] Other two distinguished works can be named as EM-CCG and acGr/SWNT by Yang et al. [8] and Pham et al., [212] both of which used vacuum filtration in their procedure which is lengthy and not scalable (Figure 5-14, marked by blue circles). Another notable work is GCNS-CS [234] electrodes (marked by purple asterisk) which were made using templating, carbonization and high temperature annealing of biomass, and similar to other activated graphene, this work is scalable and provide good performance, nevertheless, it is energy intensive. Plus, it also requires binder. Considering the state of the art work in the literature, our work is still valuable, since it provides a binder free, scalable, economically viable method for fabrication of energy dense electrodes from 2D materials.

In addition, with further improvement of the electrode assembly method, we can possibly increase the electrode's ρ_B which would result in an increase in volumetric energy and power densities.

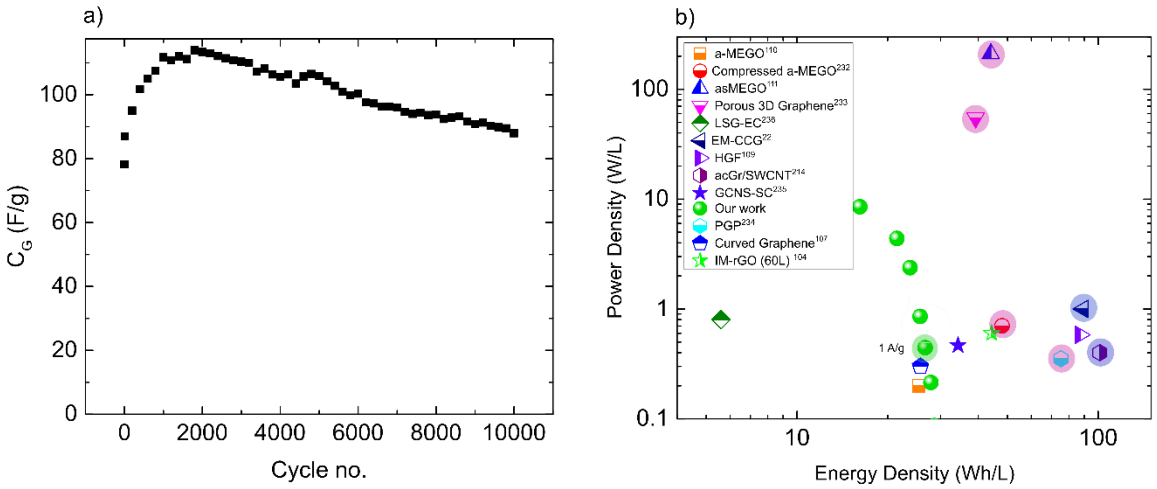

Figure 5-14: Cycle stability and Ragone plot for 20% P (2) electrode, a) cycle stability of 20% P (2) electrode, b) Ragone plot containing data of distinguished work in literature on EDLC compared to our work

Table 5-1: comparisons of the state of the art work on EDLC[1]

Reference	Mass Loading (mg/cm^2)	I(A/g)	C_G (F/g)	C_V (F/cm^3)	E_G (Wh/kg)	E_V (Wh/L)	Electrolyte (VW)	Binder additive	Density (g/cm^3)
Curved Graphene[109]	6.6	1	154	46.2	58.6	27.5	$EMImBF_4$ (4V)	5 wt% SuperP 10 wt% PTFE binder	0.3
a-MEGO[112]	2.5	1.4	165	59.8	70.6	25.4	$BMImBF_4$/ AC (3.5 V)	5 wt% PTFE binder	0.36
Compressed a-MEGO[231]	4.3	1.2	147	110	63	48	$BMImBF_4$/ AC (3.5 V)	5 wt% PTFE binder	0.75
as-MEGO[113]	1.3 10.4	2.1 1.1	173 129	102 58	74 55	44 25	EMImTFSI/ AC (3.5V)	5 wt% PTFE binder	0.59 0.45
Porous 3D Graphene[232]	4	1	231	92	98	39	$EMImBF_4$ (3.5 V)	10 wt% PTFE binder	0.4
Laser ascribed Graphene[235]	0.036	5	276	13.2	117.4	5.6	$EMImBF_4$ (3.5 V)	NA	0.046
Chemically reduced graphene[10]	3.73	1.33	99	49	21.5	10.7	$Et4NBF_4$/AN (2.5 V)	5 wt% PTFE binder	0.5
Carbide Derived Carbon[7]	15	0.3	160	85	50	26.5	EMImTFSI (3 V)	NA	0.53
Single Walled CNT array[236]	5	1	160	80	94	47	$Et4NBF_4$/PC (4.0 V)	NA	0.5
EM-CCG[23]	1 10	1 1	167 126	209 158	71 52	89 65	$EMImBF_4$/ AN (3.5 V)	NA	1.25 1.25

[1] The data are collected for the performance of single electrode at room temperature at 1 A/g, except the laser ascribed graphene (at 5 A/g)

HGF[111]	1 10	1 1	289 246	205 174	123 105	87 74	$EMImBF_4$ (3.5 V)	NA	0.71 0.71
acGr/SWNT[212]	0.6	1	172	275	95.6	101.3	$EMImBF_4$ (4V)	NA	1.06
GCNS-SC [234]	5	1	152	80.6	64.6	34.2	EMImTFSI (3V)	5 wt% PVDF binder	0.53
Our Work	1	1	160	86.4	50	26.6	EMImTFSI (3V)	NA	0.54
IM-rGO (60% IL)[106]	0.7-1.5	1	189	142	59	44.3	EMImTFSI (3V)	NA	0.75
rGO/IL gel (60% IL)[105]	0.5-1	0.2	140	64	43.73	20.125	$EMImBF_4$/3 V	NA	0.46
PGP [233]		1	152	140	84	77	$BMImBF_4$/4 V	3 wt% PTFE binder	0.9

5.4 Conclusions

In this work, we have used the concept of self-assembly of non-ionic surfactants (P123) with non-surface-active ionic liquid (IL) electrolyte, to deliver IL molecules to the surface of active electrode materials. We prepared composite electrodes of rGO/P123/IL by flash freeze drying the dispersions containing varying surfactant concentration and mass ratios of IL to P123. Overall, the C_G increased continuously with an increase in the added spacer mass up to 80 wt.% P123, however, the rheological properties of the composites made it impossible to cast the electrodes above 80 wt. %. The highest gravimetric capacitance (C_G) of 243.7 F/g was measured for 60 wt.% P123 with IL/P123 =3 (60% P (3)) which shows 150 % increase in C_G compared to control rGO electrode. Measurement of the densities of the electrode show a continuous drop of the electrode's bulk densities (ρ_{bulk}) with addition of spacer. Comparing the calculated theoretical densities ($\rho_{theo.}$) of the composites with their measured values show

on average ~70% porosity in the electrodes. Observation of the electrode's cross section uncovers the existence of large air-gaps which explain the large deviation from the $\rho_{theo.}$. The volumetric capacitance of the electrodes (C_V) as a result reduces significantly. For 60% P (3), the C_V reduced to 45 F/cm^3. The highest C_V (75 F/cm^3) was measured for 20 wt.% P123 with IL/P123 =2 (20% P (2)). The overall rate performance and internal resistance of the two electrodes were analogous, while the 60% P (3) did not require an extra work-in cycle due to the presence of enough ion conducting molecules within the electrode. The volumetric energy density of 20% P (2) electrode were 27 Wh/L and 0.44 kW/L, respectively compared to 10 Wh/L and 0.11 kW/L for 60% P (3). The 20% P (2) electrode shows 94% and 80 % capacitance retention up to 5000 and 10,000 cycles at current density of 10 A/g.

Chapter 6
Conclusions and Future Works

In this thesis, I presented three projects in support of improving the energy density of electric double layer capacitors (EDLC) based on reduced graphene oxide (rGO) as active electrode materials. The works presented here are mainly focused on developing strategies to overcome the capacitance reduction of rGO due to restacking. During these projects, I explored the possibility of using mixed IL/non-ionic surfactant as spacer for rGO electrode. In line with the abovementioned goal, I have contributed to: i) Better understanding of the self assembly and adsorption of mixed EMImTFSI/ surfactants on GO surface, ii) Investigation of the double layer capacitance that is formed between mixed EMImTFSI/surfactant and glassy carbon electrode (which emulates rGO), ii) Establishing procedure to coat rGO with mixed EMImTFSI/surfactant electrolyte to improve the capacitance. Below, summarises the main findings for each project:

In Chapter 3, we studied self-assembly of TX-100 and Tween 20 with EMImTFSI in aqueous solution, and their adsorption and self-assembly on GO surfaces. Both surfactants follow stepwise adsorption isotherm which is Langmuirian in low concentration of surfactant/IL. The concentration of the adsorbent (GO) was found to significantly influence the adsorption: lower concentration of 0.1 mg/ml GO gives rise to ~ 3 mg IL/mg GO adsorbed layer. The first plateau on the adsorption isotherm indicates the formation of a dense monolayer of adsorbate (IL/surfactant) on the GO surface. Further increase in the adsorbate concentration leads to appearance of large lumps of spherical shapes, which marks the formation of the second plateau in the adsorption isotherm. In addition, the adsorption isotherm of P123/IL was compared to TX-100/IL and Tween 20/IL showing higher adsorption. Both TX-100 and P123 can complex with IL at much lower surfactant/IL ratio compared to Tween 20 (i.e., P123/IL = 1, and TX-100/IL = 3, vs. Tween 20/IL = 4). Therefore, TX-100 and P123 were chosen for the study of our next chapter.

Chapter 4 is dedicated to studying the double layer that is formed between IL and non-ionic surfactant (TX-100 and P123). P123 has a stronger tendency to solubilize IL at lower surfactant concentrations than TX-100, plus, this surfactant contains longer PEO chains which is shown to lower the ionic correlations in ILs. For both surfactants, we noted continuous increase in the double layer capacitance (C_{DL}) up to 40 wt.% addition of surfactant. Further increase in surfactant resulted in loss of capacitance. Measurement of the viscosities and ionic conductivities of the mixed electrolytes demonstrates inconsistency between the two surfactants. While P123 had sixfold higher viscosity, its conductivity drops at the same scale as TX-100 from 8.5 mS/cm to 1 mS/cm. PFG-NMR diffusivity measurement unveils the role of P123 in better reducing the ionic correlations in EMImTFSI. Studying the voltage windows of the mixed electrolyte show reduction in electrochemical voltage window of IL with addition of surfactant, which needs to be taken into consideration while using these electrolyte series.

In Chapter 5, based on our understanding of the self-assembly of non-ionic surfactants and EMImTFSI, we established a procedure to use this mixed electrolyte as a spacer which both inhibit the restacking of rGO and boost the capacitance. Following our findings in Chapter 3, dilute dispersions of rGO/P123/IL (rGO concentration ~ 0.2 mg/ml) were created with IL/P123 ratio of 1, 2 and 3. These dispersions were sprayed upon liquid nitrogen to solidify the composites and then freeze dried. This helped prevent the reassembly of the adsorbate which often happens during air drying (i.e., evaporative consolidation). After drying, a flocculent powder was collected and pressed onto current collector to create the final electrode. The capacitance shows continuous improvement with increasing the total added spacer mass. Up to 150% increase was observed for 60 wt.% P123 with IL/P123 = 3 electrode, increasing the capacitance from 100 F/g (for rGO only) to 250 F/g. The charge transfer resistance of ~ 4 Ω further attests the improvement of ionic and electronic conductivities from that of rGO alone (9.7 Ω). Nevertheless, the density of the electrode reduced to 0.18 g/cm^3 with addition of mixed electrolytes resulting in severe reduction in C_V (45 F/cm^3).

Using lower concentration of P123 and IL, at 20 wt.% P123 with IL/P123 = 2, we maximized our C_V to 75 F/cm^3, However, the C_G was lower at 158 F/g.

Future works:

Although this work shows improvement in the performance of the EDLC using P123/IL mixed electrolyte as spacer, the dependence of capacitance to self-assembly of mixed electrolyte at the interface still need to be studied in more details. Therefore, adsorption isotherm and surface analysis study of such self-assemblies can reveal the role of particular self-assembled structure on the capacitive performance of the final electrode.

Chapter 5 showed the performance of rGO/IL/P123 composite electrodes which demonstrates 150 % enhancement in C_G for 60% P (3) electrodes compared to C_G of 100 F/g for rGO electrode (without filler). Nevertheless, the density of the composites reduces by a factor of 8 from the theoretical density of 1.4 g/cm^3 to 0.18 g/cm^3 which subsequently reduces the C_V from 345 F/cm^3 to only 45 F/cm^3. Observation of the electrode's cross section revealed the existence of large air gaps, trapped during the electrode pressing which contributed to 66% reduction in electrode's ρ_B. This reduction in ρ_B, which can be observed for all our samples, can be avoided using alternative coating methods such as calendaring. We believe the presence of mixed electrolyte in the composites contribute to trapping more air gap as the difference between theoretical and measured bulk densities increases as we add more mixed electrolyte.

In addition, a cycle-life study on 20% P (2) electrode show 80% reduction in capacitance in 10,000 cycles, observation of the electrodes after cycling revealed possible degradation of the electrolyte as a result of surpassing the electrolyte voltage stability window. As reducing the operating voltage of the device results in large reduction in the energy density, we can improve the device operating voltage by balancing the electrode's mass using asymmetric design which improves both energy density and cycle-life of the electrodes.

And lastly, the SEM image of the cross-sectional view of the 20 % P (2) electrodes revealed poor adhesion between electrode and current collector which contribute the semicircle observed on the EIS plot. I believe this poor adhesion is as a result of curved and wrinkled structure of rGO which create distance between rGO sheets and current collector which is larger than the distance for the primary energy minimum where the van der Waals attractions dominate as described in DLVO theory. To improve the adhesion at the electrode/current collector interface, finding reduction methods that produce less wrinkles on the rGO can lead to potential improvement in the interface adhesion.

References

(1) Goodenough, J. B.; Abruna, H. D.; Buchanan, M. V. *Basic Research Needs for Electrical Energy Storage. Report of the Basic Energy Sciences Workshop on Electrical Energy Storage, April 2-4, 2007*; DOESC (USDOE Office of Science (SC)), 2007. https://doi.org/10.2172/935429.

(2) Simon, P.; Gogotsi, Y. Materials for Electrochemical Capacitors. *Nat. Mater.* **2008**, *7* (11), 845–854. https://doi.org/10.1038/nmat2297.

(3) Miller, J. R.; Simon, P. Electrochemical Capacitors for Energy Management. *Science* **2008**, *321* (5889), 651–652. https://doi.org/10.1126/science.1158736.

(4) Miller, J. R.; Burke, A. Electrochemical Capacitors: Challenges and Opportunities for Real-World Applications. *Electrochem. Soc. Interface* **2008**, *17* (1), 53. https://doi.org/10.1149/2.F08081IF.

(5) Christen, T.; Carlen, M. W. Theory of Ragone Plots. *J. Power Sources* **2000**, *91* (2), 210–216. https://doi.org/10.1016/S0378-7753(00)00474-2.

(6) Mathis, T. S.; Kurra, N.; Wang, X.; Pinto, D.; Simon, P.; Gogotsi, Y. Energy Storage Data Reporting in Perspective—Guidelines for Interpreting the Performance of Electrochemical Energy Storage Systems. *Adv. Energy Mater.* **2019**, *9* (39), 1902007. https://doi.org/10.1002/aenm.201902007.

(7) Largeot, C.; Portet, C.; Chmiola, J.; Taberna, P.-L.; Gogotsi, Y.; Simon, P. Relation between the Ion Size and Pore Size for an Electric Double-Layer Capacitor. *J. Am. Chem. Soc.* **2008**, *130* (9), 2730–2731. https://doi.org/10.1021/ja7106178.

(8) Pope, M. A.; Aksay, I. A. Four-Fold Increase in the Intrinsic Capacitance of Graphene through Functionalization and Lattice Disorder. *J. Phys. Chem. C* **2015**, *119* (35), 20369–20378. https://doi.org/10.1021/acs.jpcc.5b07521.

(9) Xia, J.; Chen, F.; Li, J.; Tao, N. Measurement of the Quantum Capacitance of Graphene. *Nat. Nanotechnol.* **2009**, *4* (8), 505–509. https://doi.org/10.1038/nnano.2009.177.

(10) Stoller, M. D.; Park, S.; Zhu, Y.; An, J.; Ruoff, R. S. Graphene-Based Ultracapacitors. *Nano Lett.* **2008**, *8* (10), 3498–3502. https://doi.org/10.1021/nl802558y.

(11) Si, Y.; Samulski, E. T. Exfoliated Graphene Separated by Platinum Nanoparticles. *Chem. Mater.* **2008**, *20* (21), 6792–6797. https://doi.org/10.1021/cm801356a.

(12) Qiu, L.; Yang, X.; Gou, X.; Yang, W.; Ma, Z.-F.; Wallace, G. G.; Li, D. Dispersing Carbon Nanotubes with Graphene Oxide in Water and Synergistic Effects between Graphene Derivatives. *Chem. – Eur. J.* **2010**, *16* (35), 10653–10658. https://doi.org/10.1002/chem.201001771.

(13) Zhang, K.; Mao, L.; Zhang, L. L.; Chan, H. S. O.; Zhao, X. S.; Wu, J. Surfactant-Intercalated, Chemically Reduced Graphene Oxide for High Performance Supercapacitor Electrodes. *J. Mater. Chem.* **2011**, *21* (20), 7302–7307. https://doi.org/10.1039/C1JM00007A.

(14) Yan, J.; Wei, T.; Shao, B.; Ma, F.; Fan, Z.; Zhang, M.; Zheng, C.; Shang, Y.; Qian, W.; Wei, F. Electrochemical Properties of Graphene Nanosheet/Carbon Black Composites as Electrodes for Supercapacitors. *Carbon* **2010**, *48* (6), 1731–1737. https://doi.org/10.1016/j.carbon.2010.01.014.

(15) Conway, B. E. *Electrochemical Supercapacitors: Scientific Fundamentals and Technological Applications*; Springer US, 1999.

(16) Allen J. Bard; Larry R. Faulkner. *Electrochemical Methods: Fundamentals and Applications, 2nd Edition*, 2nd ed.; 2000.

(17) Graham, D. C. The Electrical Double Layer and the Theory of Electrocapillary. *Chem. Rev.* **1947**, *41* (3), 441–501. https://doi.org/10.1021/cr60130a002.

(18) Gerischer, H. Charge Transfer Processes at Semiconductor-Electrolyte Interfaces in Connection with Problems of Catalysis - ScienceDirect. **1969**, *18* (1), 97–122. https://doi.org/10.1016/0039-6028(69)90269-6.
(19) Randin, J.-P.; Yeager, E. Differential Capacitance Study on the Basal Plane of Stress-Annealed Pyrolytic Graphite. *J. Electroanal. Chem.* **1972**, *36* (2), 257–276. https://doi.org/10.1016/S0022-0728(72)80249-3.
(20) Conway, B. E.; Birss, V.; Wojtowicz, J. The Role and Utilization of Pseudocapacitance for Energy Storage by Supercapacitors. *J. Power Sources* **1997**, *66* (1), 1–14. https://doi.org/10.1016/S0378-7753(96)02474-3.
(21) Doherty, A. P. Redox-Active Ionic Liquids for Energy Harvesting and Storage Applications. *Curr. Opin. Electrochem.* **2018**, *7*, 61–65. https://doi.org/10.1016/j.coelec.2017.10.009.
(22) Xie, H. J.; Gélinas, B.; Rochefort, D. Redox-Active Electrolyte Supercapacitors Using Electroactive Ionic Liquids. *Electrochem. Commun.* **2016**, *66*, 42–45. https://doi.org/10.1016/j.elecom.2016.02.019.
(23) Yang, X.; Cheng, C.; Wang, Y.; Qiu, L.; Li, D. Liquid-Mediated Dense Integration of Graphene Materials for Compact Capacitive Energy Storage. *Science* **2013**, *341* (6145), 534–537. https://doi.org/10.1126/science.1239089.
(24) Fic, K.; Lota, G.; Meller, M.; Frackowiak, E. Novel Insight into Neutral Medium as Electrolyte for High-Voltage Supercapacitors. *Energy Environ. Sci.* **2012**, *5* (2), 5842–5850. https://doi.org/10.1039/C1EE02262H.
(25) Zhong, C.; Deng, Y.; Hu, W.; Qiao, J.; Zhang, L.; Zhang, J. A Review of Electrolyte Materials and Compositions for Electrochemical Supercapacitors. *Chem. Soc. Rev.* **2015**, *44* (21), 7484–7539.
(26) Narita, A.; Shibayama, W.; Sakamoto, K.; Mizumo, T.; Matsumi, N.; Ohno, H. Lithium Ion Conduction in an Organoborate Zwitterion–LiTFSI Mixture. *Chem Commun* **2006**, No. 18, 1926–1928. https://doi.org/10.1039/B517019B.
(27) Matsumi, N.; Sugai, K.; Miyake, M.; Ohno, H. Polymerized Ionic Liquids via Hydroboration Polymerization as Single Ion Conductive Polymer Electrolytes. *Macromolecules* **2006**, *39* (20), 6924–6927. https://doi.org/10.1021/ma060472j.
(28) Lu, F.; Gao, X.; Wu, A.; Sun, N.; Shi, L.; Zheng, L. Lithium-Containing Zwitterionic Poly(Ionic Liquid)s as Polymer Electrolytes for Lithium-Ion Batteries. *J. Phys. Chem. C* **2017**, *121* (33), 17756–17763. https://doi.org/10.1021/acs.jpcc.7b06242.
(29) Mirjafari, A.; N. Pham, L.; R. McCabe, J.; Mobarrez, N.; Alan Salter, E.; Wierzbicki, A.; N. West, K.; E. Sykora, R.; H. Davis, J. Building a Bridge between Aprotic and Protic Ionic Liquids. *RSC Adv.* **2013**, *3* (2), 337–340. https://doi.org/10.1039/C2RA22752E.
(30) MacFarlane, D. R.; Seddon, K. R.; MacFarlane, D. R.; Seddon, K. R. Ionic Liquids—Progress on the Fundamental Issues. *Aust. J. Chem.* **2007**, *60* (1), 3–5. https://doi.org/10.1071/CH06478.
(31) Byrne, N.; Rodoni, B.; Constable, F.; Varghese, S.; Davis, J. H. Enhanced Stabilization of the Tobacco Mosaic Virus Using Protic Ionic Liquids. *Phys. Chem. Chem. Phys.* **2012**, *14* (29), 10119–10121. https://doi.org/10.1039/C2CP41625E.
(32) Rochefort, D.; Pont, A.-L. Pseudocapacitive Behaviour of RuO2 in a Proton Exchange Ionic Liquid. *Electrochem. Commun.* **2006**, *8* (9), 1539–1543. https://doi.org/10.1016/j.elecom.2006.06.032.
(33) Smith, D. E.; Walsh, D. A. The Nature of Proton Shuttling in Protic Ionic Liquid Fuel Cells. *Adv. Energy Mater.* **2019**, *9* (24), 1900744. https://doi.org/10.1002/aenm.201900744.
(34) Luo, H.; Baker, G. A.; Lee, J. S.; Pagni, R. M.; Dai, S. Ultrastable Superbase-Derived Protic Ionic Liquids. *J. Phys. Chem. B* **2009**, *113* (13), 4181–4183. https://doi.org/10.1021/jp901312d.

(35) Shi, M.; Kou, S.; Yan, X. Engineering the Electrochemical Capacitive Properties of Graphene Sheets in Ionic-Liquid Electrolytes by Correct Selection of Anions. *ChemSusChem* **2014**, *7* (11), 3053–3062. https://doi.org/10.1002/cssc.201402275.
(36) Kornyshev, A. A. Double-Layer in Ionic Liquids: Paradigm Change? *J. Phys. Chem. B* **2007**, *111* (20), 5545–5557. https://doi.org/10.1021/jp067857o.
(37) Bazant, M. Z.; Storey, B. D.; Kornyshev, A. A. Double Layer in Ionic Liquids: Overscreening versus Crowding. *Phys. Rev. Lett.* **2011**, *106* (4), 046102. https://doi.org/10.1103/PhysRevLett.106.046102.
(38) Kornyshev, A. A.; Luque, N. B.; Schmickler, W. Differential Capacitance of Ionic Liquid Interface with Graphite: The Story of Two Double Layers. *J. Solid State Electrochem.* **2014**, *18* (5), 1345–1349. https://doi.org/10.1007/s10008-013-2316-8.
(39) González, A.; Goikolea, E.; Barrena, J. A.; Mysyk, R. Review on Supercapacitors: Technologies and Materials. *Renew. Sustain. Energy Rev.* **2016**, *58*, 1189–1206. https://doi.org/10.1016/j.rser.2015.12.249.
(40) Snook, G. A.; Kao, P.; Best, A. S. Conducting-Polymer-Based Supercapacitor Devices and Electrodes. *J. Power Sources* **2011**, *196* (1), 1–12. https://doi.org/10.1016/j.jpowsour.2010.06.084.
(41) Snook, G. A.; Chen, G. Z. The Measurement of Specific Capacitances of Conducting Polymers Using the Quartz Crystal Microbalance. *J. Electroanal. Chem.* **2008**, *612* (1), 140–146. https://doi.org/10.1016/j.jelechem.2007.08.024.
(42) Yu, F.; Pang, L.; Wang, H.-X. Preparation of Mulberry-like RuO2 Electrode Material for Supercapacitors. *Rare Met.* **2021**, *40* (2), 440–447. https://doi.org/10.1007/s12598-020-01561-8.
(43) Liao, Q.; Li, N.; Jin, S.; Yang, G.; Wang, C. All-Solid-State Symmetric Supercapacitor Based on Co3O4 Nanoparticles on Vertically Aligned Graphene. *ACS Nano* **2015**, *9* (5), 5310–5317. https://doi.org/10.1021/acsnano.5b00821.
(44) Noh, J.; Yoon, C.-M.; Kim, Y. K.; Jang, J. High Performance Asymmetric Supercapacitor Twisted from Carbon Fiber/MnO2 and Carbon Fiber/MoO3. *Carbon* **2017**, *116*, 470–478. https://doi.org/10.1016/j.carbon.2017.02.033.
(45) Gujar, T. P.; Kim, W.-Y.; Puspitasari, I.; Jung, K.-D.; Joo, O.-S. Electrochemically Deposited Nanograin Ruthenium Oxide as a Pseudocapacitive Electrode. *Int J Electrochem Sci* **2007**, *2*, 9.
(46) Frackowiak, E.; Delpeux, S.; Jurewicz, K.; Szostak, K.; Cazorla-Amoros, D.; Béguin, F. Enhanced Capacitance of Carbon Nanotubes through Chemical Activation. *Chem. Phys. Lett.* **2002**, *361* (1–2), 35–41. https://doi.org/10.1016/S0009-2614(02)00684-X.
(47) Gao, L.; Peng, A.; Wang, Z. Y.; Zhang, H.; Shi, Z.; Gu, Z.; Cao, G.; Ding, B. Growth of Aligned Carbon Nanotube Arrays on Metallic Substrate and Its Application to Supercapacitors. *Solid State Commun.* **2008**, *146* (9), 380–383. https://doi.org/10.1016/j.ssc.2008.03.034.
(48) Honda, Y.; Haramoto, T.; Takeshige, M.; Shiozaki, H.; Kitamura, T.; Ishikawa, M. Aligned MWCNT Sheet Electrodes Prepared by Transfer Methodology Providing High-Power Capacitor Performance. *Electrochem. Solid-State Lett.* **2007**, *10* (4), A106. https://doi.org/10.1149/1.2437665.
(49) Futaba, D. N.; Hata, K.; Yamada, T.; Hiraoka, T.; Hayamizu, Y.; Kakudate, Y.; Tanaike, O.; Hatori, H.; Yumura, M.; Iijima, S. Shape-Engineerable and Highly Densely Packed Single-Walled Carbon Nanotubes and Their Application as Super-Capacitor Electrodes. *Nat. Mater.* **2006**, *5* (12), 987–994. https://doi.org/10.1038/nmat1782.
(50) Frackowiak, E.; Béguin, F. Carbon Materials for the Electrochemical Storage of Energy in Capacitors. *Carbon* **2001**, *39* (6), 937–950. https://doi.org/10.1016/S0008-6223(00)00183-4.

(51) Niu, C.; Sichel, E. K.; Hoch, R.; Moy, D.; Tennent, H. High Power Electrochemical Capacitors Based on Carbon Nanotube Electrodes. *Appl. Phys. Lett.* **1997**, *70* (11), 1480–1482. https://doi.org/10.1063/1.118568.
(52) Jiang, Q.; Qu, M. Z.; Zhou, G. M.; Zhang, B. L.; Yu, Z. L. A Study of Activated Carbon Nanotubes as Electrochemical Super Capacitors Electrode Materials. *Mater. Lett.* **2002**, *57* (4), 988–991. https://doi.org/10.1016/S0167-577X(02)00911-4.
(53) Hughes, M.; Chen, G. Z.; Shaffer, M. S. P.; Fray, D. J.; Windle, A. H. Electrochemical Capacitance of a Nanoporous Composite of Carbon Nanotubes and Polypyrrole. *Chem. Mater.* **2002**, *14* (4), 1610–1613. https://doi.org/10.1021/cm010744r.
(54) Gratuito, M. K. B.; Panyathanmaporn, T.; Chumnanklang, R.-A.; Sirinuntawittaya, N.; Dutta, A. Production of Activated Carbon from Coconut Shell: Optimization Using Response Surface Methodology. *Bioresour. Technol.* **2008**, *99* (11), 4887–4895. https://doi.org/10.1016/j.biortech.2007.09.042.
(55) Hou, J.; Cao, C.; Idrees, F.; Ma, X. Hierarchical Porous Nitrogen-Doped Carbon Nanosheets Derived from Silk for Ultrahigh-Capacity Battery Anodes and Supercapacitors. *ACS Nano* **2015**, *9* (3), 2556–2564. https://doi.org/10.1021/nn506394r.
(56) Hayashi, J.; Kazehaya, A.; Muroyama, K.; Watkinson, A. P. Preparation of Activated Carbon from Lignin by Chemical Activation. *Carbon* **2000**, *38* (13), 1873–1878. https://doi.org/10.1016/S0008-6223(00)00027-0.
(57) Pandolfo, A. G.; Hollenkamp, A. F. Carbon Properties and Their Role in Supercapacitors. *J. Power Sources* **2006**, *157* (1), 11–27. https://doi.org/10.1016/j.jpowsour.2006.02.065.
(58) Simon, P.; Burke, A. Nanostructured Carbons : Double-Layer Capacitance and More. **2008**. https://doi.org/10.1149/2.f05081if.
(59) Fernández, J. A.; Morishita, T.; Toyoda, M.; Inagaki, M.; Stoeckli, F.; Centeno, T. A. Performance of Mesoporous Carbons Derived from Poly(Vinyl Alcohol) in Electrochemical Capacitors. *J. Power Sources* **2008**, *175* (1), 675–679. https://doi.org/10.1016/j.jpowsour.2007.09.042.
(60) Jurewicz, K.; Vix-Guterl, C.; Frackowiak, E.; Saadallah, S.; Reda, M.; Parmentier, J.; Patarin, J.; Béguin, F. Capacitance Properties of Ordered Porous Carbon Materials Prepared by a Templating Procedure. *J. Phys. Chem. Solids* **2004**, *65* (2), 287–293. https://doi.org/10.1016/j.jpcs.2003.10.024.
(61) Raymundo-Piñero, E.; Kierzek, K.; Machnikowski, J.; Béguin, F. Relationship between the Nanoporous Texture of Activated Carbons and Their Capacitance Properties in Different Electrolytes. *Carbon* **2006**, *44* (12), 2498–2507. https://doi.org/10.1016/j.carbon.2006.05.022.
(62) Jänes, A.; Permann, L.; Arulepp, M.; Lust, E. Electrochemical Characteristics of Nanoporous Carbide-Derived Carbon Materials in Non-Aqueous Electrolyte Solutions. *Electrochem. Commun.* **2004**, *6* (3), 313–318. https://doi.org/10.1016/j.elecom.2004.01.009.
(63) Novoselov, K. S.; Geim, A. K.; Morozov, S. V.; Jiang, D.; Zhang, Y.; Dubonos, S. V.; Grigorieva, I. V.; Firsov, A. A. Electric Field Effect in Atomically Thin Carbon Films. *Science* **2004**, *306* (5696), 666–669. https://doi.org/10.1126/science.1102896.
(64) Kim, K. S.; Zhao, Y.; Jang, H.; Lee, S. Y.; Kim, J. M.; Kim, K. S.; Ahn, J.-H.; Kim, P.; Choi, J.-Y.; Hong, B. H. Large-Scale Pattern Growth of Graphene Films for Stretchable Transparent Electrodes. *Nature* **2009**, *457* (7230), 706–710. https://doi.org/10.1038/nature07719.
(65) Wintterlin, J.; Bocquet, M.-L. Graphene on Metal Surfaces. *Surf. Sci.* **2009**, *603* (10), 1841–1852. https://doi.org/10.1016/j.susc.2008.08.037.
(66) Daniela C. Marcano; Dimitry V. Kosynkin; Jacob M. Berlin; Alexander Sinitskii; Zhengzong Sun; Alexander Slesarev; Lawrence B. Alemany; Wei Lu; James M. Tour. Improved Synthesis of Graphene Oxide - ACS Nano (ACS Publications). *ACS Nano* **2010**, *4* (8), 4806–4814.

(67) Rio-Castillo, A. E. D.; Merino, C.; Díez-Barra, E.; Vázquez, E. Selective Suspension of Single Layer Graphene Mechanochemically Exfoliated from Carbon Nanofibres | SpringerLink. *Nano Res.* **2014**, *7* (7), 963–972.
(68) Yumura, T.; Kimura, K.; Kobayashi, H.; Tanaka, R.; Okumura, N.; Yamabe, T. The Use of Nanometer-Sized Hydrographene Species for Support Material for Fuel Cell Electrode Catalysts: A Theoretical Proposal. *Phys. Chem. Chem. Phys.* **2009**, *11* (37), 8275–8284. https://doi.org/10.1039/B905866D.
(69) Wang, X.; Zhi, L.; Müllen, K. Transparent, Conductive Graphene Electrodes for Dye-Sensitized Solar Cells. *Nano Lett.* **2008**, *8* (1), 323–327. https://doi.org/10.1021/nl072838r.
(70) Gerischer, H. An Interpretation of the Double Layer Capacity of Graphite Electrodes in Relation to the Density of States at the Fermi Level. *J. Phys. Chem.* **1985**, *89* (20), 4249–4251. https://doi.org/10.1021/j100266a020.
(71) Chen, J.-H.; Jang, C.; Adam, S.; Fuhrer, M. S.; Williams, E. D.; Ishigami, M. Charged-Impurity Scattering in Graphene. *Nat. Phys.* **2008**, *4* (5), 377–381. https://doi.org/10.1038/nphys935.
(72) Brodie, Benjamin Collins. Sur Le Poids Atomique Du Graphite. *Ann Chim Phys* **1860**, *59*, e472.
(73) Staudenmaier, L. Verfahren zur Darstellung der Graphitsäure. *Berichte Dtsch. Chem. Ges.* **1898**, *31* (2), 1481–1487. https://doi.org/10.1002/cber.18980310237.
(74) Hummers, W. S.; Offeman, R. E. Preparation of Graphitic Oxide. *J. Am. Chem. Soc.* **1958**, *80* (6), 1339–1339. https://doi.org/10.1021/ja01539a017.
(75) Du, X. S.; Xiao, M.; Meng, Y. Z.; Hay, A. S. Novel Synthesis of Conductive Poly(Arylene Disulfide)/Graphite Nanocomposite. *Synth. Met.* **2004**, *143* (1), 129–132. https://doi.org/10.1016/j.synthmet.2003.10.023.
(76) Matsuo, Y.; Hatase, K.; Sugie, Y. Selective Intercalation of Aromatic Molecules into Alkyltrimethylammonium Ion-Intercalated Graphite Oxide. *Chem. Lett.* **1999**, *28* (10), 1109–1110. https://doi.org/10.1246/cl.1999.1109.
(77) Kotov, N. A.; Dékány, I.; Fendler, J. H. Ultrathin Graphite Oxide–Polyelectrolyte Composites Prepared by Self-Assembly: Transition between Conductive and Non-Conductive States. *Adv. Mater.* **1996**, *8* (8), 637–641. https://doi.org/10.1002/adma.19960080806.
(78) Tian, Y.; Yu, Z.; Cao, L.; Zhang, X. L.; Sun, C.; Wang, D.-W. Graphene Oxide: An Emerging Electromaterial for Energy Storage and Conversion. *J. Energy Chem.* **2021**, *55*, 323–344. https://doi.org/10.1016/j.jechem.2020.07.006.
(79) Szabó, T.; Berkesi, O.; Forgó, P.; Josepovits, K.; Sanakis, Y.; Petridis, D.; Dékány, I. Evolution of Surface Functional Groups in a Series of Progressively Oxidized Graphite Oxides. *Chem. Mater.* **2006**, *18* (11), 2740–2749. https://doi.org/10.1021/cm060258+.
(80) He, H.; Riedl, T.; Lerf, A.; Klinowski, J. Solid-State NMR Studies of the Structure of Graphite Oxide. *J. Phys. Chem.* **1996**, *100* (51), 19954–19958. https://doi.org/10.1021/jp961563t.
(81) Lerf, A.; He, H.; Riedl, T.; Forster, M.; Klinowski, J. 13C and 1H MAS NMR Studies of Graphite Oxide and Its Chemically Modified Derivatives. *Solid State Ion.* **1997**, *101–103*, 857–862. https://doi.org/10.1016/S0167-2738(97)00319-6.
(82) Lerf, A.; He, H.; Forster, M.; Klinowski, J. Structure of Graphite Oxide Revisited. *J. Phys. Chem. B* **1998**, *102* (23), 4477–4482. https://doi.org/10.1021/jp9731821.
(83) He, H.; Klinowski, J.; Forster, M.; Lerf, A. A New Structural Model for Graphite Oxide. *Chem. Phys. Lett.* **1998**, *287* (1), 53–56. https://doi.org/10.1016/S0009-2614(98)00144-4.
(84) Stankovich, S.; Dikin, D. A.; Piner, R. D.; Kohlhaas, K. A.; Kleinhammes, A.; Jia, Y.; Wu, Y.; Nguyen, S. T.; Ruoff, R. S. Synthesis of Graphene-Based Nanosheets via Chemical Reduction of Exfoliated Graphite Oxide. *Carbon* **2007**, *45* (7), 1558–1565. https://doi.org/10.1016/j.carbon.2007.02.034.

(85) Lau, K. S.; Ginting, R. T.; Tan, S. T.; Chin, S. X.; Zakaria, S.; Chia, C. H. Sodium Cholate as Efficient Green Reducing Agent for Graphene Oxide via Flow Reaction for Flexible Supercapacitor Electrodes. *J. Mater. Sci. Mater. Electron.* **2019**, *30* (21), 19182–19188. https://doi.org/10.1007/s10854-019-02275-z.
(86) Guex, L. G.; Sacchi, B.; Peuvot, K. F.; Andersson, R. L.; Pourrahimi, A. M.; Ström, V.; Farris, S.; Olsson, R. T. Experimental Review: Chemical Reduction of Graphene Oxide (GO) to Reduced Graphene Oxide (RGO) by Aqueous Chemistry. *Nanoscale* **2017**, *9* (27), 9562–9571. https://doi.org/10.1039/C7NR02943H.
(87) Schniepp, H. C.; Li, J.-L.; McAllister, M. J.; Sai, H.; Herrera-Alonso, M.; Adamson, D. H.; Prud'homme, R. K.; Car, R.; Saville, D. A.; Aksay, I. A. Functionalized Single Graphene Sheets Derived from Splitting Graphite Oxide. *J. Phys. Chem. B* **2006**, *110* (17), 8535–8539. https://doi.org/10.1021/jp060936f.
(88) Pope, M. A.; Punckt, C.; Aksay, I. A. Intrinsic Capacitance and Redox Activity of Functionalized Graphene Sheets. *J. Phys. Chem. C* **2011**, *115* (41), 20326–20334. https://doi.org/10.1021/jp2068667.
(89) Trusovas, R.; Ratautas, K.; Račiukaitis, G.; Barkauskas, J.; Stankevičienė, I.; Niaura, G.; Mažeikienė, R. Reduction of Graphite Oxide to Graphene with Laser Irradiation. *Carbon* **2013**, *52*, 574–582. https://doi.org/10.1016/j.carbon.2012.10.017.
(90) Zhu, Y.; Murali, S.; Stoller, M. D.; Velamakanni, A.; Piner, R. D.; Ruoff, R. S. Microwave Assisted Exfoliation and Reduction of Graphite Oxide for Ultracapacitors. *Carbon* **2010**, *48* (7), 2118–2122. https://doi.org/10.1016/j.carbon.2010.02.001.
(91) Wan, J.; Huang, L.; Wu, J.; Xiong, L.; Hu, Z.; Yu, H.; Li, T.; Zhou, J. Microwave Combustion for Rapidly Synthesizing Pore-Size-Controllable Porous Graphene. *Adv. Funct. Mater.* **2018**, *28* (22), 1800382. https://doi.org/10.1002/adfm.201800382.
(92) Alotaibi, F.; Tung, T. T.; Nine, M. J.; Kabiri, S.; Moussa, M.; Tran, D. N. H.; Losic, D. Scanning Atmospheric Plasma for Ultrafast Reduction of Graphene Oxide and Fabrication of Highly Conductive Graphene Films and Patterns. *Carbon* **2018**, *127*, 113–121. https://doi.org/10.1016/j.carbon.2017.10.075.
(93) Zhou, Y.; Bao, Q.; Tang, L. A. L.; Zhong, Y.; Loh, K. P. Hydrothermal Dehydration for the "Green" Reduction of Exfoliated Graphene Oxide to Graphene and Demonstration of Tunable Optical Limiting Properties. *Chem. Mater.* **2009**, *21* (13), 2950–2956. https://doi.org/10.1021/cm9006603.
(94) Toh, S. Y.; Loh, K. S.; Kamarudin, S. K.; Daud, W. R. W. Graphene Production via Electrochemical Reduction of Graphene Oxide: Synthesis and Characterisation. *Chem. Eng. J.* **2014**, *251*, 422–434. https://doi.org/10.1016/j.cej.2014.04.004.
(95) Gao, J.; Liu, F.; Liu, Y.; Ma, N.; Wang, Z.; Zhang, X. Environment-Friendly Method To Produce Graphene That Employs Vitamin C and Amino Acid. *Chem. Mater.* **2010**, *22* (7), 2213–2218. https://doi.org/10.1021/cm902635j.
(96) Shruthi, G.; Baishali, G.; Radhakrishna, V.; Verma, P. Reducing Graphene Oxide Using Hydroiodic Acid Fumes and Low Temperature Annealing for Enhanced Electrical Conductivity. *Graphene Technol.* **2020**, *5* (1), 19–25. https://doi.org/10.1007/s41127-020-00030-4.
(97) Chen, Y.; Zhang, X.; Zhang, D.; Yu, P.; Ma, Y. High Performance Supercapacitors Based on Reduced Graphene Oxide in Aqueous and Ionic Liquid Electrolytes. *Carbon* **2011**, *49* (2), 573–580. https://doi.org/10.1016/j.carbon.2010.09.060.
(98) Li, D.; Müller, M. B.; Gilje, S.; Kaner, R. B.; Wallace, G. G. Processable Aqueous Dispersions of Graphene Nanosheets. *Nat. Nanotechnol.* **2008**, *3* (2), 101–105. https://doi.org/10.1038/nnano.2007.451.

(99) Everett, D. H. *Basic Principles of Colloid Science*; 1988. https://doi.org/10.1039/9781847550200.
(100) Mattevi, C.; Eda, G.; Agnoli, S.; Miller, S.; Mkhoyan, K. A.; Celik, O.; Mastrogiovanni, D.; Granozzi, G.; Carfunkel, E.; Chhowalla, M. Evolution of Electrical, Chemical, and Structural Properties of Transparent and Conducting Chemically Derived Graphene Thin Films. *Adv. Funct. Mater.* **2009**, *19* (16), 2577–2583. https://doi.org/10.1002/adfm.200900166.
(101) An, X.; Simmons, T.; Shah, R.; Wolfe, C.; Lewis, K. M.; Washington, M.; Nayak, S. K.; Talapatra, S.; Kar, S. Stable Aqueous Dispersions of Noncovalently Functionalized Graphene from Graphite and Their Multifunctional High-Performance Applications. *Nano Lett.* **2010**, *10* (11), 4295–4301. https://doi.org/10.1021/nl903557p.
(102) Lei, Z.; Christov, N.; Zhao, X. S. Intercalation of Mesoporous Carbon Spheres between Reduced Graphene Oxide Sheets for Preparing High-Rate Supercapacitor Electrodes. *Energy Environ. Sci.* **2011**, *4* (5), 1866–1873. https://doi.org/10.1039/C1EE01094H.
(103) Yu, D.; Dai, L. Self-Assembled Graphene/Carbon Nanotube Hybrid Films for Supercapacitors. *J. Phys. Chem. Lett.* **2010**, *1* (2), 467–470. https://doi.org/10.1021/jz9003137.
(104) Lu, X.; Dou, H.; Gao, B.; Yuan, C.; Yang, S.; Hao, L.; Shen, L.; Zhang, X. A Flexible Graphene/Multiwalled Carbon Nanotube Film as a High Performance Electrode Material for Supercapacitors. *Electrochimica Acta* **2011**, *56* (14), 5115–5121. https://doi.org/10.1016/j.electacta.2011.03.066.
(105) Pope, M. A.; Korkut, S.; Punckt, C.; Aksay, I. A. Supercapacitor Electrodes Produced through Evaporative Consolidation of Graphene Oxide-Water-Ionic Liquid Gels. *J. Electrochem. Soc.* **2013**, *160* (10), A1653–A1660. https://doi.org/10.1149/2.017310jes.
(106) She, Z.; Ghosh, D.; Pope, M. A. Decorating Graphene Oxide with Ionic Liquid Nanodroplets: An Approach Leading to Energy-Dense, High-Voltage Supercapacitors. *ACS Nano* **2017**, *11* (10), 10077–10087. https://doi.org/10.1021/acsnano.7b04467.
(107) Gao, J.; Shao, C.; Shao, S.; Bai, C.; Khalil, U. R.; Zhao, Y.; Jiang, L.; Qu, L. Laser-Assisted Multiscale Fabrication of Configuration-Editable Supercapacitors with High Energy Density. *ACS Nano* **2019**, *13* (7), 7463–7470. https://doi.org/10.1021/acsnano.9b02176.
(108) Fan, Q.; Zhao, R.; Yi, M.; Qi, P.; Chai, C.; Ying, H.; Hao, J. Ti3C2-MXene Composite Films Functionalized with Polypyrrole and Ionic Liquid-Based Microemulsion Particles for Supercapacitor Applications. *Chem. Eng. J.* **2022**, *428*, 131107. https://doi.org/10.1016/j.cej.2021.131107.
(109) Liu, C.; Yu, Z.; Neff, D.; Zhamu, A.; Jang, B. Z. Graphene-Based Supercapacitor with an Ultrahigh Energy Density. *Nano Lett.* **2010**, *10* (12), 4863–4868. https://doi.org/10.1021/nl102661q.
(110) Luo, J.; Jang, H. D.; Huang, J. Effect of Sheet Morphology on the Scalability of Graphene-Based Ultracapacitors. *ACS Nano* **2013**, *7* (2), 1464–1471. https://doi.org/10.1021/nn3052378.
(111) Xu, Y.; Lin, Z.; Zhong, X.; Huang, X.; Weiss, N. O.; Huang, Y.; Duan, X. Holey Graphene Frameworks for Highly Efficient Capacitive Energy Storage. *Nat. Commun.* **2014**, *5* (1), 4554. https://doi.org/10.1038/ncomms5554.
(112) Zhu, Y.; Murali, S.; Stoller, M. D.; Ganesh, K. J.; Cai, W.; Ferreira, P. J.; Pirkle, A.; Wallace, R. M.; Cychosz, K. A.; Thommes, M.; Su, D.; Stach, E. A.; Ruoff, R. S. Carbon-Based Supercapacitors Produced by Activation of Graphene. *Science* **2011**, *332* (6037), 1537–1541. https://doi.org/10.1126/science.1200770.
(113) Kim, T.; Jung, G.; Yoo, S.; Suh, K. S.; Ruoff, R. S. Activated Graphene-Based Carbons as Supercapacitor Electrodes with Macro- and Mesopores. *ACS Nano* **2013**, *7* (8), 6899–6905. https://doi.org/10.1021/nn402077v.

(114) Zhang, K.; Zhang, L. L.; Zhao, X. S.; Wu, J. Graphene/Polyaniline Nanofiber Composites as Supercapacitor Electrodes. *Chem. Mater.* **2010**, *22* (4), 1392–1401. https://doi.org/10.1021/cm902876u.
(115) Wang, H.; Hao, Q.; Yang, X.; Lu, L.; Wang, X. A Nanostructured Graphene/Polyaniline Hybrid Material for Supercapacitors. *Nanoscale* **2010**, *2* (10), 2164–2170. https://doi.org/10.1039/C0NR00224K.
(116) Yan, J.; Wei, T.; Shao, B.; Fan, Z.; Qian, W.; Zhang, M.; Wei, F. Preparation of a Graphene Nanosheet/Polyaniline Composite with High Specific Capacitance. *Carbon* **2010**, *48* (2), 487–493. https://doi.org/10.1016/j.carbon.2009.09.066.
(117) *Electrochemical performance of a graphene–polypyrrole nanocomposite as a supercapacitor electrode - IOPscience*. https://iopscience.iop.org/article/10.1088/0957-4484/22/29/295202 (accessed 2022-03-26).
(118) Chen, S.; Zhu, J.; Wu, X.; Han, Q.; Wang, X. Graphene Oxide−MnO2 Nanocomposites for Supercapacitors. *ACS Nano* **2010**, *4* (5), 2822–2830. https://doi.org/10.1021/nn901311t.
(119) Wu, Z.-S.; Wang, D.-W.; Ren, W.; Zhao, J.; Zhou, G.; Li, F.; Cheng, H.-M. Anchoring Hydrous RuO2 on Graphene Sheets for High-Performance Electrochemical Capacitors. *Adv. Funct. Mater.* **2010**, *20* (20), 3595–3602. https://doi.org/10.1002/adfm.201001054.
(120) Vivekchand, S. R. C.; Rout, C. S.; Subrahmanyam, K. S.; Govindaraj, A.; Rao, C. N. R. Graphene-Based Electrochemical Supercapacitors. *J. Chem. Sci.* **2008**, *120* (1), 9–13. https://doi.org/10.1007/s12039-008-0002-7.
(121) Kim, T. Y.; Lee, H. W.; Stoller, M.; Dreyer, D. R.; Bielawski, C. W.; Ruoff, R. S.; Suh, K. S. High-Performance Supercapacitors Based on Poly(Ionic Liquid)-Modified Graphene Electrodes. *ACS Nano* **2011**, *5* (1), 436–442. https://doi.org/10.1021/nn101968p.
(122) Kim, T. Y.; Lee, H. W.; Stoller, M.; Dreyer, D. R.; Bielawski, C. W.; Ruoff, R. S.; Suh, K. S. High-Performance Supercapacitors Based on Poly(Ionic Liquid)-Modified Graphene Electrodes. *ACS Nano* **2011**, *5* (1), 436–442. https://doi.org/10.1021/nn101968p.
(123) Lashkari, S.; Chekini, M.; Pal, R.; Pope, M. A. Aqueous, Mixed Micelles as a Means of Delivering the Hydrophobic Ionic Liquid EMIM TFSI to Graphene Oxide Surfaces. *Langmuir* **2022**. https://doi.org/10.1021/acs.langmuir.1c02928.
(124) Galiński, M.; Lewandowski, A.; Stępniak, I. Ionic Liquids as Electrolytes. *Electrochimica Acta* **2006**, *51* (26), 5567–5580. https://doi.org/10.1016/j.electacta.2006.03.016.
(125) Kang, X.; Sun, X.; Han, B. Synthesis of Functional Nanomaterials in Ionic Liquids. *Adv. Mater.* **2016**, *28* (6), 1011–1030. https://doi.org/10.1002/adma.201502924.
(126) Berthod, A.; He, L.; Armstrong, D. W. Ionic Liquids as Stationary Phase Solvents for Methylated Cyclodextrins in Gas Chromatography. *Chromatographia* **2001**, *53* (1), 63–68. https://doi.org/10.1007/BF02492429.
(127) Carda–Broch, S.; Berthod, A.; Armstrong, D. W. Solvent Properties of the 1-Butyl-3-Methylimidazolium Hexafluorophosphate Ionic Liquid. *Anal. Bioanal. Chem.* **2003**, *375* (2), 191–199. https://doi.org/10.1007/s00216-002-1684-1.
(128) Dupont, J.; Fonseca, G. S.; Umpierre, A. P.; Fichtner, P. F. P.; Teixeira, S. R. Transition-Metal Nanoparticles in Imidazolium Ionic Liquids: Recycable Catalysts for Biphasic Hydrogenation Reactions. *J. Am. Chem. Soc.* **2002**, *124* (16), 4228–4229. https://doi.org/10.1021/ja025818u.
(129) Chen, M.; Cui, Y.; Qian, W.; Peng, Q.; Wang, J.; Gong, H.; Fang, J.; Dai, S.; Hou, Z. Thermoregulated Ionic Liquid-Stabilizing Ru/CoO Nanocomposites for Catalytic Hydrogenation. *Langmuir* **2020**, *36* (39), 11589–11599. https://doi.org/10.1021/acs.langmuir.0c02153.

(130) Sakaebe, H.; Matsumoto, H. N-Methyl-N-Propylpiperidinium Bis(Trifluoromethanesulfonyl)Imide (PP13–TFSI) – Novel Electrolyte Base for Li Battery. *Electrochem. Commun.* **2003**, *5* (7), 594–598. https://doi.org/10.1016/S1388-2481(03)00137-1.
(131) Carlin, R. T.; Long, H. C. D.; Fuller, J.; Trulove, P. C. Dual Intercalating Molten Electrolyte Batteries. *J. Electrochem. Soc.* **1994**, *141* (7), L73. https://doi.org/10.1149/1.2055041.
(132) Sato, T.; Masuda, G.; Takagi, K. Electrochemical Properties of Novel Ionic Liquids for Electric Double Layer Capacitor Applications. *Electrochimica Acta* **2004**, *49* (21), 3603–3611. https://doi.org/10.1016/j.electacta.2004.03.030.
(133) Chakraborty, M.; Ahmed, T.; Sarkar, M. Understanding the Behavior of Monocationic and Dicationic Room-Temperature Ionic Liquids through Resonance Energy-Transfer Studies. *Langmuir* **2019**, *35* (49), 16172–16184. https://doi.org/10.1021/acs.langmuir.9b02776.
(134) Buzzeo, M. C.; Hardacre, C.; Compton, R. G. Use of Room Temperature Ionic Liquids in Gas Sensor Design. *Anal. Chem.* **2004**, *76* (15), 4583–4588. https://doi.org/10.1021/ac040042w.
(135) Vijayakrishna, K.; Mecerreyes, D.; Gnanou, Y.; Taton, D. Polymeric Vesicles and Micelles Obtained by Self-Assembly of Ionic Liquid-Based Block Copolymers Triggered by Anion or Solvent Exchange. *Macromolecules* **2009**, *42* (14), 5167–5174. https://doi.org/10.1021/ma900549k.
(136) Bhushan, V.; Heitz, M. P.; Baker, G. A.; Pandey, S. Ionic Liquid-Controlled Shape Transformation of Spherical to Nonspherical Polymersomes via Hierarchical Self-Assembly of a Diblock Copolymer. *Langmuir* **2021**, *37* (16), 5081–5088. https://doi.org/10.1021/acs.langmuir.1c00821.
(137) Behera, K.; Dahiya, P.; Pandey, S. Effect of Added Ionic Liquid on Aqueous Triton X-100 Micelles. *J. Colloid Interface Sci.* **2007**, *307* (1), 235–245. https://doi.org/10.1016/j.jcis.2006.11.009.
(138) Pramanik, R.; Sarkar, S.; Ghatak, C.; Rao, V. G.; Mandal, S.; Sarkar, N. Effects of 1-Butyl-3-Methyl Imidazolium Tetrafluoroborate Ionic Liquid on Triton X-100 Aqueous Micelles: Solvent and Rotational Relaxation Studies. *J. Phys. Chem. B* **2011**, *115* (21), 6957–6963. https://doi.org/10.1021/jp111755j.
(139) Zhang, S.; Gao, Y.; Dong, B.; Zheng, L. Interaction between the Added Long-Chain Ionic Liquid 1-Dodecyl-3-Methylimidazolium Tetrafluoroborate and Triton X-100 in Aqueous Solutions. *Colloids Surf. Physicochem. Eng. Asp.* **2010**, *372* (1), 182–189. https://doi.org/10.1016/j.colsurfa.2010.10.011.
(140) Thakkar, K.; Patel, V.; Ray, D.; Pal, H.; Aswal, V. K.; Bahadur, P. Interaction of Imidazolium Based Ionic Liquids with Triton X-100 Micelles: Investigating the Role of the Counter Ion and Chain Length. *RSC Adv.* **2016**, *6* (43), 36314–36326. https://doi.org/10.1039/C6RA03086F.
(141) Behera, K.; Pandey, M. D.; Porel, M.; Pandey, S. Unique Role of Hydrophilic Ionic Liquid in Modifying Properties of Aqueous Triton X-100. *J. Chem. Phys.* **2007**, *127* (18), 184501. https://doi.org/10.1063/1.2785178.
(142) Zhao, M.; Zheng, L.; Bai, X.; Li, N.; Yu, L. Fabrication of Silica Nanoparticles and Hollow Spheres Using Ionic Liquid Microemulsion Droplets as Templates. *Colloids Surf. Physicochem. Eng. Asp.* **2009**, *346* (1), 229–236. https://doi.org/10.1016/j.colsurfa.2009.06.021.
(143) Li, Z.; Zhang, J.; Du, J.; Han, B.; Wang, J. Preparation of Silica Microrods with Nano-Sized Pores in Ionic Liquid Microemulsions. *Colloids Surf. Physicochem. Eng. Asp.* **2006**, *286* (1), 117–120. https://doi.org/10.1016/j.colsurfa.2006.03.011.
(144) Harada, M.; Kimura, Y.; Saijo, K.; Ogawa, T.; Isoda, S. Photochemical Synthesis of Silver Particles in Tween 20/Water/Ionic Liquid Microemulsions. *J. Colloid Interface Sci.* **2009**, *339* (2), 373–381. https://doi.org/10.1016/j.jcis.2009.08.003.

(145) Kaur, M.; Singh, G.; Kaur, A.; Sharma, P. K.; Kang, T. S. Thermally Stable Ionic Liquid-Based Microemulsions for High-Temperature Stabilization of Lysozyme at Nanointerfaces. *Langmuir* **2019**, *35* (11), 4085–4093. https://doi.org/10.1021/acs.langmuir.9b00106.
(146) Ducker, W. A.; Grant, L. M. Effect of Substrate Hydrophobicity on Surfactant Surface−Aggregate Geometry. *J. Phys. Chem.* **1996**, *100* (28), 11507–11511. https://doi.org/10.1021/jp9607024.
(147) Manne, S.; Cleveland, J. P.; Gaub, H. E.; Stucky, G. D.; Hansma, P. K. Direct Visualization of Surfactant Hemimicelles by Force Microscopy of the Electrical Double Layer. *Langmuir* **1994**, *10* (12), 4409–4413. https://doi.org/10.1021/la00024a003.
(148) Jaschke, M.; Butt, H.-J.; Gaub, H. E.; Manne, S. Surfactant Aggregates at a Metal Surface. *Langmuir* **1997**, *13* (6), 1381–1384. https://doi.org/10.1021/la9607767.
(149) Amirmoshiri, M.; Zhang, L.; Puerto, M. C.; Tewari, R. D.; Bahrim, R. Z. B. K.; Farajzadeh, R.; Hirasaki, G. J.; Biswal, S. L. Role of Wettability on the Adsorption of an Anionic Surfactant on Sandstone Cores. *Langmuir* **2020**, *36* (36), 10725–10738. https://doi.org/10.1021/acs.langmuir.0c01521.
(150) Acero, P. N.; Mohr, S.; Bernabei, M.; Fernández, C.; Domínguez, B.; Ewen, J. P. Molecular Simulations of Surfactant Adsorption on Iron Oxide from Hydrocarbon Solvents. *Langmuir* **2021**. https://doi.org/10.1021/acs.langmuir.1c02133.
(151) Ma, K.; Li, P. X.; Thomas, R. K.; Penfold, J. Unusual Maximum in the Adsorption of Aqueous Surfactant Mixtures: Neutron Reflectometry of Mixtures of Zwitterionic and Ionic Surfactants at the Silica–Aqueous Interface. *Langmuir* **2021**, *37* (13), 3939–3949. https://doi.org/10.1021/acs.langmuir.1c00178.
(152) Koppel, D. E. Analysis of Macromolecular Polydispersity in Intensity Correlation Spectroscopy: The Method of Cumulants. *J. Chem. Phys.* **1972**, *57* (11), 4814–4820. https://doi.org/10.1063/1.1678153.
(153) Simone, P. M.; Lodge, T. P. Micellization of PS-PMMA Diblock Copolymers in an Ionic Liquid. *Macromol. Chem. Phys.* **2007**, *208* (4), 339–348. https://doi.org/10.1002/macp.200600392.
(154) Hait, S. K.; Moulik, S. P. Determination of Critical Micelle Concentration (CMC) of Nonionic Surfactants by Donor-Acceptor Interaction with Lodine and Correlation of CMC with Hydrophile-Lipophile Balance and Other Parameters of the Surfactants. *J. Surfactants Deterg.* **2001**, *4* (3), 303–309.
(155) Bernard Valeur. *Molecular Fluorescence: Principles and Applications*; Wiley-VCH Verlag GmbH, 2001.
(156) Huddleston, J. G.; Visser, A. E.; Reichert, W. M.; Willauer, H. D.; Broker, G. A.; Rogers, R. D. Characterization and Comparison of Hydrophilic and Hydrophobic Room Temperature Ionic Liquids Incorporating the Imidazolium Cation. *Green Chem.* **2001**, *3* (4), 156–164. https://doi.org/10.1039/B103275P.
(157) Molina-Bolívar, J. A.; Aguiar, J.; Ruiz, C. C. Growth and Hydration Of Triton X-100 Micelles In Monovalent Alkali Salts: A Light Scattering Study. *J. Phys. Chem. B* **2002**, *106* (4), 870–877. https://doi.org/10.1021/jp0119936.
(158) Sadaghiani, A. Salehi.; Khan, Ali. Self-Assembly in System of Lecithin and Nonionic Amphiphile from NMR Studies. *Langmuir* **1991**, *7* (5), 898–904. https://doi.org/10.1021/la00053a015.
(159) Brown, W.; Rymden, R.; Van Stam, J.; Almgren, M.; Svensk, G. Static and Dynamic Properties of Nonionic Amphiphile Micelles: Triton X-100 in Aqueous Solution. *J. Phys. Chem.* **1989**, *93* (6), 2512–2519. https://doi.org/10.1021/j100343a055.
(160) Phillies, G. D. J.; Yambert, J. E. Solvent and Solute Effects on Hydration and Aggregation Numbers of Triton X-100 Micelles. *Langmuir* **1996**, *12* (14), 3431–3436. https://doi.org/10.1021/la951088a.

(161) Denkova, P. S.; Lokeren, L. V.; Verbruggen, I.; Willem, R. Self-Aggregation and Supramolecular Structure Investigations of Triton X-100 and SDP2S by NOESY and Diffusion Ordered NMR Spectroscopy. *J. Phys. Chem. B* **2008**, *112* (35), 10935–10941. https://doi.org/10.1021/jp802830g.
(162) Basheva, E. S.; Kralchevsky, P. A.; Danov, K. D.; Ananthapadmanabhan, K. P.; Lips, A. The Colloid Structural Forces as a Tool for Particle Characterization and Control of Dispersion Stability. *Phys. Chem. Chem. Phys.* **2007**, *9* (38), 5183–5198. https://doi.org/10.1039/B705758J.
(163) Pal, A.; Deenadayalu, N.; Chaudhary, S. Effect of Hydrophilic Ionic Liquid on the Micellar Properties of Aqueous Tween-20. *Fluid Phase Equilibria* **2015**, *391*, 67–71. https://doi.org/10.1016/j.fluid.2015.02.005.
(164) *Free Download Spectrometric Identification of Organic Compounds 7e by Silverstein*. Chemistry.Com.Pk. https://chemistry.com.pk/books/spectrometric-identification-of-organic-compounds-7e/ (accessed 2019-11-07).
(165) Liu, Y.; Liu, C.; Liu, Y. Investigation on Fluorescence Quenching of Dyes by Graphite Oxide and Graphene. *Appl. Surf. Sci.* **2011**, *257* (13), 5513–5518. https://doi.org/10.1016/j.apsusc.2010.12.136.
(166) Lakowicz, J. R. *Principles of Fluorescence Spectroscopy*, 3rd ed.; Springer US, 2006. https://doi.org/10.1007/978-0-387-46312-4.
(167) Cao, X.; Meng, L.; Li, Z.; Mao, Y.; Lan, H.; Chen, L.; Fan, Y.; Yi, T. Large Red-Shifted Fluorescent Emission via Intermolecular π–π Stacking in 4-Ethynyl-1,8-Naphthalimide-Based Supramolecular Assemblies. *Langmuir* **2014**, *30* (39), 11753–11760. https://doi.org/10.1021/la503299j.
(168) Giles, C. H.; Smith, D.; Huitson, A. A General Treatment and Classification of the Solute Adsorption Isotherm. I. Theoretical. *J. Colloid Interface Sci.* **1974**, *47* (3), 755–765. https://doi.org/10.1016/0021-9797(74)90252-5.
(169) Galbraith, J. W.; Giles, C. H.; Halliday, A. G.; Hassan, A. S. A.; McAllister, D. C.; Macaulay, N.; Macmillan, N. W. Adsorption at inorganic surfaces. III. The mechanism of adsorption of organic solutes, including dyes, by graphite. *J. Appl. Chem.* **1958**, *8* (7), 416–424. https://doi.org/10.1002/jctb.5010080704.
(170) Gómez-Navarro, C.; Weitz, R. T.; Bittner, A. M.; Scolari, M.; Mews, A.; Burghard, M.; Kern, K. Electronic Transport Properties of Individual Chemically Reduced Graphene Oxide Sheets. *Nano Lett.* **2007**, *7* (11), 3499–3503. https://doi.org/10.1021/nl072090c.
(171) Robson, R. J.; Dennis, E. A. The Size, Shape, and Hydration of Nonionic Surfactant Micelles. Triton X-100. *J. Phys. Chem.* **1977**, *81* (11), 1075–1078. https://doi.org/10.1021/j100526a010.
(172) Lashkari, S.; Pal, R.; Pope, M. A. Ionic Liquid/Non-Ionic Surfactant Mixtures as Versatile, Non-Volatile Electrolytes: Double-Layer Capacitance and Conductivity. *J. Electrochem. Soc.* **2022**, *169* (4), 040513. https://doi.org/10.1149/1945-7111/ac62c7.
(173) Bordes, E.; Douce, L.; Quitevis, E. L.; Pádua, A. A. H.; Costa Gomes, M. Ionic Liquids at the Surface of Graphite: Wettability and Structure. *J. Chem. Phys.* **2018**, *148* (19), 193840. https://doi.org/10.1063/1.5010604.
(174) Liu, T.; Wang, K.; Chen, Y.; Zhao, S.; Han, Y. Dominant Role of Wettability in Improving the Specific Capacitance. *Green Energy Environ.* **2019**, *4* (2), 171–179. https://doi.org/10.1016/j.gee.2019.01.010.
(175) Vaquero, S.; Palma, J.; Anderson, M.; Marcilla, R. Improving Performance of Electric Double Layer Capacitors with a Mixture of Ionic Liquid and Acetonitrile as the Electrolyte by Using Mass-Balancing Carbon Electrodes. *J. Electrochem. Soc.* **2013**, *160* (11), A2064. https://doi.org/10.1149/2.063311jes.

(176) Kim, Y.-J.; Matsuzawa, Y.; Ozaki, S.; Park, K. C.; Kim, C.; Endo, M.; Yoshida, H.; Masuda, G.; Sato, T.; Dresselhaus, M. S. High Energy-Density Capacitor Based on Ammonium Salt Type Ionic Liquids and Their Mixing Effect by Propylene Carbonate. *J. Electrochem. Soc.* **2005**, *152* (4), A710. https://doi.org/10.1149/1.1869232.
(177) Bozym, D. J.; Uralcan, B.; Limmer, D. T.; Pope, M. A.; Szamreta, N. J.; Debenedetti, P. G.; Aksay, I. A. Anomalous Capacitance Maximum of the Glassy Carbon–Ionic Liquid Interface through Dilution with Organic Solvents. *J. Phys. Chem. Lett.* **2015**, *6* (13), 2644–2648. https://doi.org/10.1021/acs.jpclett.5b00899.
(178) Moreno, M.; Simonetti, E.; Appetecchi, G. B.; Carewska, M.; Montanino, M.; Kim, G.-T.; Loeffler, N.; Passerini, S. Ionic Liquid Electrolytes for Safer Lithium Batteries. *J. Electrochem. Soc.* **2016**, *164* (1), A6026. https://doi.org/10.1149/2.0051701jes.
(179) Tooming, T.; Thomberg, T.; Siinor, L.; Tõnurist, K.; Jänes, A.; Lust, E. A Type High Capacitance Supercapacitor Based on Mixed Room Temperature Ionic Liquids Containing Specifically Adsorbed Iodide Anions. *J. Electrochem. Soc.* **2013**, *161* (3), A222. https://doi.org/10.1149/2.014403jes.
(180) Lodge, T. P. A Unique Platform for Materials Design. *Science* **2008**, *321* (5885), 50–51. https://doi.org/10.1126/science.1159652.
(181) He, Y.; Boswell, P. G.; Bühlmann, P.; Lodge, T. P. Ion Gels by Self-Assembly of a Triblock Copolymer in an Ionic Liquid. *J. Phys. Chem. B* **2007**, *111* (18), 4645–4652. https://doi.org/10.1021/jp064574n.
(182) She, Z.; Ghosh, D.; Pope, M. A. Decorating Graphene Oxide with Ionic Liquid Nanodroplets: An Approach Leading to Energy-Dense, High-Voltage Supercapacitors. *ACS Nano* **2017**, *11* (10), 10077–10087. https://doi.org/10.1021/acsnano.7b04467.
(183) Osti, N. C.; Van Aken, K. L.; Thompson, M. W.; Tiet, F.; Jiang, D.; Cummings, P. T.; Gogotsi, Y.; Mamontov, E. Solvent Polarity Governs Ion Interactions and Transport in a Solvated Room-Temperature Ionic Liquid. *J. Phys. Chem. Lett.* **2017**, *8* (1), 167–171. https://doi.org/10.1021/acs.jpclett.6b02587.
(184) Meli, L.; Santiago, J. M.; Lodge, T. P. Path-Dependent Morphology and Relaxation Kinetics of Highly Amphiphilic Diblock Copolymer Micelles in Ionic Liquids. *Macromolecules* **2010**, *43* (4), 2018–2027. https://doi.org/10.1021/ma902366c.
(185) Lockett, V.; Horne, M.; Sedev, R.; Rodopoulos, T.; Ralston, J. Differential Capacitance of the Double Layer at the Electrode/Ionic Liquids Interface. *Phys. Chem. Chem. Phys.* **2010**, *12* (39), 12499–12512. https://doi.org/10.1039/C0CP00170H.
(186) Lockett, V.; Sedev, R.; Ralston, J.; Horne, M.; Rodopoulos, T. Differential Capacitance of the Electrical Double Layer in Imidazolium-Based Ionic Liquids: Influence of Potential, Cation Size, and Temperature. 10.
(187) Noda, A.; Hayamizu, K.; Watanabe, M. Pulsed-Gradient Spin−Echo 1H and 19F NMR Ionic Diffusion Coefficient, Viscosity, and Ionic Conductivity of Non-Chloroaluminate Room-Temperature Ionic Liquids. *J. Phys. Chem. B* **2001**, *105* (20), 4603–4610. https://doi.org/10.1021/jp004132q.
(188) Amann, T.; Dold, C.; Kailer, A. Rheological Characterization of Ionic Liquids and Ionic Liquid Crystals with Promising Tribological Performance. *Soft Matter* **2012**, *8* (38), 9840–9846. https://doi.org/10.1039/C2SM26030A.
(189) Wittmar, A.; Ruiz-Abad, D.; Ulbricht, M. Dispersions of Silica Nanoparticles in Ionic Liquids Investigated with Advanced Rheology. *J. Nanoparticle Res.* **2012**, *14* (2), 651. https://doi.org/10.1007/s11051-011-0651-1.

(190) L. Burrell, G.; F. Dunlop, N.; Separovic, F. Non-Newtonian Viscous Shear Thinning in Ionic Liquids. *Soft Matter* **2010**, *6* (9), 2080–2086. https://doi.org/10.1039/B916049N.
(191) McEwen, A. B.; Ngo, H. L.; LeCompte, K.; Goldman, J. L. Electrochemical Properties of Imidazolium Salt Electrolytes for Electrochemical Capacitor Applications. *J. Electrochem. Soc.* **1999**, *146* (5), 1687. https://doi.org/10.1149/1.1391827.
(192) Wu, D. H.; Chen, A. D.; Johnson, C. S. An Improved Diffusion-Ordered Spectroscopy Experiment Incorporating Bipolar-Gradient Pulses. *J. Magn. Reson. A* **1995**, *115* (2), 260–264. https://doi.org/10.1006/jmra.1995.1176.
(193) Stejskal, E. O. Use of Spin Echoes in a Pulsed Magnetic-Field Gradient to Study Anisotropic, Restricted Diffusion and Flow. *J. Chem. Phys.* **1965**, *43* (10), 3597–3603. https://doi.org/10.1063/1.1696526.
(194) Généreux, S.; Gariépy, V.; Rochefort, D. On the Relevance of Reporting Water Content in Highly Concentrated Electrolytes: The LiTFSI-Acetonitrile Case. *J. Electrochem. Soc.* **2020**, *167* (12), 120536. https://doi.org/10.1149/1945-7111/abb34c.
(195) O'Mahony, A. M.; Silvester, D. S.; Aldous, L.; Hardacre, C.; Compton, R. G. Effect of Water on the Electrochemical Window and Potential Limits of Room-Temperature Ionic Liquids. *J. Chem. Eng. Data* **2008**, *53* (12), 2884–2891. https://doi.org/10.1021/je800678e.
(196) Klein, J. M.; Panichi, E.; Gurkan, B. Potential Dependent Capacitance of [EMIM][TFSI], [N1114][TFSI] and [PYR13][TFSI] Ionic Liquids on Glassy Carbon. *Phys. Chem. Chem. Phys.* **2019**, *21* (7), 3712–3720. https://doi.org/10.1039/C8CP04631J.
(197) Drüschler, M.; Huber, B.; Roling, B. On Capacitive Processes at the Interface between 1-Ethyl-3-Methylimidazolium Tris(Pentafluoroethyl)Trifluorophosphate and Au(111). *J. Phys. Chem. C* **2011**, *115* (14), 6802–6808. https://doi.org/10.1021/jp200395j.
(198) Roling, B.; Drüschler, M.; Huber, B. Slow and Fast Capacitive Process Taking Place at the Ionic Liquid/Electrode Interface. *Faraday Discuss.* **2012**, *154*, 303–311. https://doi.org/10.1039/c1fd00088h.
(199) Nanjundiah, C.; McDevitt, S. F.; Koch, V. R. Differential Capacitance Measurements in Solvent-Free Ionic Liquids at Hg and C Interfaces. *J. Electrochem. Soc.* **1997**, *144* (10), 3392. https://doi.org/10.1149/1.1838024.
(200) Uralcan, B.; Aksay, I. A.; Debenedetti, P. G.; Limmer, D. T. Concentration Fluctuations and Capacitive Response in Dense Ionic Solutions. *J. Phys. Chem. Lett.* **2016**, *7* (13), 2333–2338. https://doi.org/10.1021/acs.jpclett.6b00859.
(201) Lee, A. A.; Perez-Martinez, C. S.; Smith, A. M.; Perkin, S. Scaling Analysis of the Screening Length in Concentrated Electrolytes. *Phys. Rev. Lett.* **2017**, *119* (2), 026002. https://doi.org/10.1103/PhysRevLett.119.026002.
(202) Joachimowicz, N.; Conessa, C.; Henriksson, T.; Duchêne, B. Breast Phantoms for Microwave Imaging. *IEEE Antennas Wirel. Propag. Lett.* **2014**, *13*, 1333–1336. https://doi.org/10.1109/LAWP.2014.2336373.
(203) Lee, A. A.; Perez-Martinez, C. S.; Smith, A. M.; Perkin, S. Underscreening in Concentrated Electrolytes. *Faraday Discuss.* **2017**, *199* (0), 239–259. https://doi.org/10.1039/C6FD00250A.
(204) Jitvisate, M.; Seddon, J. R. T. Direct Measurement of the Differential Capacitance of Solvent-Free and Dilute Ionic Liquids. *J. Phys. Chem. Lett.* **2018**, *9* (1), 126–131. https://doi.org/10.1021/acs.jpclett.7b02946.
(205) Hussey, C. L.; Sun, I.-W.; Strubinger, S. K. D.; Barnard, P. A. Some Observations about the Diffusion Coefficients of Anionic Transition Metal Halide Complexes in Room-Temperature Haloaluminate Ionic Liquids. *J. Electrochem. Soc.* **1990**, *137* (8), 2515. https://doi.org/10.1149/1.2086978.

(206) Noel, M. A. M.; Allendoerfer, R. D.; Osteryoung, R. A. Solvation in Ionic Liquids: An EPR Study. *J. Phys. Chem.* **1992**, *96* (5), 2391–2394. https://doi.org/10.1021/j100184a070.
(207) Nanjundiah, C.; Osteryoung, R. A. Electrochemical Studies of Cu(I) and Cu(II) in an Aluminum Chloride-N-(N-Butyl)Pyridinium Chloride Ionic Liquid. *J. Electrochem. Soc.* **1983**, *130* (6), 1312. https://doi.org/10.1149/1.2119944.
(208) Yamaguchi, N.; Sato, M. Dipole Moment of Poly(Ethylene Oxide) in Solution and Its Dependence on Molecular Weight and Temperature. *Polym. J.* **2009**, *41* (8), 588–594. https://doi.org/10.1295/polymj.PJ2008232.
(209) Wang, M.; Xiao, X.; Zhou, X.; Li, X.; Lin, Y. Investigation of PEO-Imidazole Ionic Liquid Oligomer Electrolytes for Dye-Sensitized Solar Cells. *Sol. Energy Mater. Sol. Cells* **2007**, *91* (9), 785–790. https://doi.org/10.1016/j.solmat.2007.01.009.
(210) Ong, M. T.; Verners, O.; Draeger, E. W.; van Duin, A. C. T.; Lordi, V.; Pask, J. E. Lithium Ion Solvation and Diffusion in Bulk Organic Electrolytes from First-Principles and Classical Reactive Molecular Dynamics. *J. Phys. Chem. B* **2015**, *119* (4), 1535–1545. https://doi.org/10.1021/jp508184f.
(211) Kirchner, B.; Malberg, F.; Firaha, D. S.; Hollóczki, O. Ion Pairing in Ionic Liquids. *J. Phys. Condens. Matter* **2015**, *27* (46), 463002. https://doi.org/10.1088/0953-8984/27/46/463002.
(212) Pham, D. T.; Lee, T. H.; Luong, D. H.; Yao, F.; Ghosh, A.; Le, V. T.; Kim, T. H.; Li, B.; Chang, J.; Lee, Y. H. Carbon Nanotube-Bridged Graphene 3D Building Blocks for Ultrafast Compact Supercapacitors. *ACS Nano* **2015**, *9* (2), 2018–2027. https://doi.org/10.1021/nn507079x.
(213) Yang, X.; Qiu, L.; Cheng, C.; Wu, Y.; Ma, Z.-F.; Li, D. Ordered Gelation of Chemically Converted Graphene for Next-Generation Electroconductive Hydrogel Films. *Angew. Chem. Int. Ed Engl.* **2011**, *50* (32), 7325–7328. https://doi.org/10.1002/anie.201100723.
(214) Zhu, P.; Shen, M.; Xiao, S.; Zhang, D. Experimental Study on the Reducibility of Graphene Oxide by Hydrazine Hydrate. *Phys. B Condens. Matter* **2011**, *406* (3), 498–502. https://doi.org/10.1016/j.physb.2010.11.022.
(215) Schillén, K.; Jansson, J.; Löf, D.; Costa, T. Mixed Micelles of a PEO−PPO−PEO Triblock Copolymer (P123) and a Nonionic Surfactant (C12EO6) in Water. A Dynamic and Static Light Scattering Study. *J. Phys. Chem. B* **2008**, *112* (18), 5551–5562. https://doi.org/10.1021/jp074832w.
(216) Zheng, L.; Guo, C.; Wang, J.; Liang, X.; Chen, S.; Ma, J.; Yang, B.; Jiang, Y.; Liu, H. Effect of Ionic Liquids on the Aggregation Behavior of PEO-PPO-PEO Block Copolymers in Aqueous Solution. *J. Phys. Chem. B* **2007**, *111* (6), 1327–1333. https://doi.org/10.1021/jp066727c.
(217) Freundlich, H. Über die Adsorption in Lösungen. *Z. Für Phys. Chem.* **1907**, *57U* (1), 385–470. https://doi.org/10.1515/zpch-1907-5723.
(218) Hong, B. J.; Compton, O. C.; An, Z.; Eryazici, I.; Nguyen, S. T. Successful Stabilization of Graphene Oxide in Electrolyte Solutions: Enhancement of Biofunctionalization and Cellular Uptake. *ACS Nano* **2012**, *6* (1), 63–73. https://doi.org/10.1021/nn202355p.
(219) Yan, Y.; Piao, L.; Kim, S.-H.; Li, W.; Zhou, H. Effect of Pluronic Block Copolymers on Aqueous Dispersions of Graphene Oxide. *RSC Adv.* **2015**, *5* (50), 40199–40204. https://doi.org/10.1039/C5RA03525B.
(220) Miranda, D. F.; Russell, T. P.; Watkins, J. J. Ordering in Mixtures of a Triblock Copolymer with a Room Temperature Ionic Liquid. *Macromolecules* **2010**, *43* (24), 10528–10535. https://doi.org/10.1021/ma1015209.
(221) Jiang, J.-C.; Li, S.-C.; Shih, P.-M.; Hung, T.-C.; Chang, S.-C.; Lin, S. H.; Chang, H.-C. A High-Pressure Infrared Spectroscopic Study on the Interaction of Ionic Liquids with PEO-PPO-PEO

Block Copolymers and 1,4-Dioxane. *J. Phys. Chem. B* **2011**, *115* (5), 883–888. https://doi.org/10.1021/jp109600c.
(222) Chen, W.; Yan, L.; Bangal, P. R. Chemical Reduction of Graphene Oxide to Graphene by Sulfur-Containing Compounds. *J. Phys. Chem. C* **2010**, *114* (47), 19885–19890. https://doi.org/10.1021/jp107131v.
(223) Pope, M. A. *Electrochemical Double-Layer Capacitors Based on Functionalized Graphene*; Princeton University, 2013.
(224) Kanematsu, T.; Sato, T.; Imai, Y.; Ute, K.; Kitayama, T. Mutual- and Self-Diffusion Coefficients of a Semiflexible Polymer in Solution. *Polym. J.* **2005**, *37* (2), 65–73. https://doi.org/10.1295/polymj.37.65.
(225) Zhu, B.-Y.; Gu, T. Surfactant Adsorption at Solid-Liquid Interfaces. *Adv. Colloid Interface Sci.* **1991**, *37* (1), 1–32. https://doi.org/10.1016/0001-8686(91)80037-K.
(226) Colegate, D. M.; Bain, C. D. Adsorption Kinetics in Micellar Solutions of Nonionic Surfactants. *Phys. Rev. Lett.* **2005**, *95* (19), 198302. https://doi.org/10.1103/PhysRevLett.95.198302.
(227) Nagao, M.; Kobayashi, K.; Jin, Y.; Maruyama, I.; Hibino, T. Ionic Conductive and Photocatalytic Properties of Cementitious Materials: Calcium Silicate Hydrate and Calcium Aluminoferrite. *J. Mater. Chem. A* **2020**, *8* (30), 15157–15166. https://doi.org/10.1039/D0TA04866F.
(228) Wang, G.; Zhang, L.; Zhang, J. A Review of Electrode Materials for Electrochemical Supercapacitors. *Chem. Soc. Rev.* **2012**, *41* (2), 797–828. https://doi.org/10.1039/C1CS15060J.
(229) Taberna, P. L.; Simon, P.; Fauvarque, J. F. Electrochemical Characteristics and Impedance Spectroscopy Studies of Carbon-Carbon Supercapacitors. *J. Electrochem. Soc.* **2003**, *150* (3), A292. https://doi.org/10.1149/1.1543948.
(230) Liu, J.-C.; Li, H.; Batmunkh, M.; Xiao, X.; Sun, Y.; Zhao, Q.; Liu, X.; Huang, Z.-H.; Ma, T.-Y. Structural Engineering to Maintain the Superior Capacitance of Molybdenum Oxides at Ultrahigh Mass Loadings. *J. Mater. Chem. A* **2019**, *7* (41), 23941–23948. https://doi.org/10.1039/C9TA04835A.
(231) Murali, S.; Quarles, N.; Zhang, L. L.; Potts, J. R.; Tan, Z.; Lu, Y.; Zhu, Y.; Ruoff, R. S. Volumetric Capacitance of Compressed Activated Microwave-Expanded Graphite Oxide (a-MEGO) Electrodes. *Nano Energy* **2013**, *2* (5), 764–768. https://doi.org/10.1016/j.nanoen.2013.01.007.
(232) Zhang, L.; Zhang, F.; Yang, X.; Long, G.; Wu, Y.; Zhang, T.; Leng, K.; Huang, Y.; Ma, Y.; Yu, A.; Chen, Y. Porous 3D Graphene-Based Bulk Materials with Exceptional High Surface Area and Excellent Conductivity for Supercapacitors. *Sci. Rep.* **2013**, *3* (1), 1408. https://doi.org/10.1038/srep01408.
(233) Li, H.; Tao, Y.; Zheng, X.; Li, Z.; Liu, D.; Xu, Z.; Luo, C.; Luo, J.; Kang, F.; Yang, Q.-H. Compressed Porous Graphene Particles for Use as Supercapacitor Electrodes with Excellent Volumetric Performance. *Nanoscale* **2015**, *7* (44), 18459–18463. https://doi.org/10.1039/C5NR06113J.
(234) Tian, W.; Gao, Q.; Tan, Y.; Li, Z. Unusual Interconnected Graphitized Carbon Nanosheets as the Electrode of High-Rate Ionic Liquid-Based Supercapacitor. *Carbon* **2017**, *119*, 287–295. https://doi.org/10.1016/j.carbon.2017.04.050.
(235) El-Kady, M. F.; Strong, V.; Dubin, S.; Kaner, R. B. Laser Scribing of High-Performance and Flexible Graphene-Based Electrochemical Capacitors. *Science* **2012**, *335* (6074), 1326–1330. https://doi.org/10.1126/science.1216744.
(236) Izadi-Najafabadi, A.; Yasuda, S.; Kobashi, K.; Yamada, T.; Futaba, D. N.; Hatori, H.; Yumura, M.; Iijima, S.; Hata, K. Extracting the Full Potential of Single-Walled Carbon Nanotubes as

Durable Supercapacitor Electrodes Operable at 4 V with High Power and Energy Density. *Adv. Mater*. **2010**, *22* (35), E235–E241. https://doi.org/10.1002/adma.200904349.